RAINFALL ATTENUATION PREDICTION MODEL FOR DYNAMIC RAIN FADE MITIGATION TECHNIQUE CONSIDERING MILLIMETER WAVE COMMUNICATION LINK

By

Mary Nabangala

In fulfillment of the Degree of Doctor of Philosophy in Electronic Engineering.
College of Agriculture, Engineering and Science,
University of KwaZulu-Natal, Durban, South Africa

UNIVERSITY OF KWAZULU-NATAL

December 2018

Supervisor:

Prof. Thomas Joachim Odhiambo Afullo

Co-supervisor:

Dr. Akintunde Ayodeji Alonge

As the candidate's Supervisors we agree to the submission of this dissertation

Prof. Thomas Joachim Odhiambo Afullo

Signed …… Date: …….

Dr. Akintunde Ayodeji Alonge

Signed …… Date: …….

DECLARATION 1 - PLAGIARISM

I, **Mary Nabangala**, student number **215000279**, as pertains the thesis entitled: *A modelling approach to rainfall attenuation prediction for dynamic rain fade mitigation*, hereby declare that:

1. The research reported in this thesis, except where otherwise indicated, is my original research.
2. This dissertation has not been submitted for any degree or examination at any other university.
3. This dissertation does not contain other persons' data, pictures, graphs or other information, unless specifically acknowledged as being sourced from other persons.
4. This dissertation does not contain other persons' writing, unless specifically acknowledged as being sourced from other researchers. Where other written sources have been quoted, then:
    a) their words have been re-written but the general information attributed to them has been referenced;
    b) where their exact words have been used, their writing has been placed inside quotation marks, and referenced.
5. Where I have reproduced a publication of which I am an author, co-author or editor, I have indicated in detail those parts of the publication written by myself alone and have fully referenced such publications.
6. This thesis does not contain text, graphics or tables copied and pasted from the Internet, unless specifically acknowledged, and the source being detailed in the thesis and in the References sections.

Signed …… Date: …….

Mary Nabangala

DECLARATION 2 - PUBLICATIONS

Mary N. Ahuna, Thomas J. Afullo, Akintunde A. Alonge, "Outage Prediction during Intense Rainstorm Events Using Queuing Theory and Markov Chains Over Radio Links", *Progress In Electromagnetic Research M*, Vol. 73, pp. 183-196, 2018.

Mary N. Ahuna, Thomas J. Afullo and Akintunde A. Alonge, "Rain attenuation prediction using artificial neural network for dynamic rain fade mitigation," *SAIEE Africa Research Journal*, Vol. 110(1), pp. 11-18, March 2019.

Mary N. Ahuna, Thomas J. Afullo and Akintunde A. Alonge, "Rainfall rate prediction based on artificial neural networks for rain fade mitigation over earth-satellite link" *Proceedings of IEEE AFRICON Conference*, Cape Town, South Africa, pp. 579-584, 18th – 20th September 2017.

Mary N. Ahuna and Thomas J. Afullo, "Effects of storm attenuation over satellite links in sub-tropical Africa," *The 40th PIERS 2018 Conference*, 1st – 4th August, Toyama, Japan, 2018, p. 153.

Mary N. Ahuna and Thomas J. Afullo, "Rain fade duration statistics over Ku-band radio links in sub-tropical South Africa" *South African Telecommunications Network and Applications Conference* (SATNAC), Cape Town, South Africa, 2nd – 5th September, 2018, pp. 434-438.

Mary N. Ahuna, Thomas J. Afullo and Akintunde A. Alonge, "Specific rain attenuation dependence on rain storm magnitudes and measured drop sizes" *IEEE Radio 2018 Conference*, 15th-18th October, Hilton Resort and Spa, Wolmar, *Mauritius*, 2018.

Signed …… Date: …….

Mary Nabangala

DEDICATION

I dedicate this work to my loving husband, *Michael* and our lovely gifts from God, *Joel* and *Noelle* for their endless and limitless support, love and encouragement

ACKNOWLEDGMENTS

First and foremost, I thank the Almighty God for the gift of life and good health for successful completion of this work.

Special thanks goes to my supervisor, Prof. *Thomas J. O. Afullo* for his guidance, support and constructive suggestions during my research work. I thank my co-supervisor, Dr. *Akintunde A. Alonge* for his support and guidance in this work, not forgetting Dr. *Modissa Mosalaosi* for his positive criticisms during the progressive journey in this work and for his dedicated proof-reading services.

A big thank you goes to all staff members in the School of Engineering and College of Agriculture, Engineering and Sciences, Howard College, for their immense contribution in the success of this research work, not to mention Mr. *Sphamandla S. Nqayi*, the CRART Centre administrator, for his great support and Ms *Ausie Luthuli* and *Nombuso Dlamini* from the College office.

To all my postgraduate colleagues and friends, a big thank you – especially Mr. *Gevira Otieno,* Mr. *Nicholas Oyie*, Mr. *Steven Awino,* and Mr. *Olabamidele Kolawole*.

More thanks to the staff of discipline of Electrical, Electronic and Computer Engineering – Dr. *Leigh Jarvis* (Academic leader), Prof. *J-R Tapamo,* Prof. *J. Okello,* Dr. *T. Walingo, B. Mokoena* and *N. Dumisile,* among others.

More thanks to the technical staff, *N. Hlambisa* (Conrad), Mr. *A. Lester*, Mr. U. *Roopnund*, Mr. *D. Govender, A. Stengel, D. Moodley* among others.

Lastly, lots of appreciations go to my husband, *Michael* and our two lovely children, *Joel* and *Noelle* for their moral support and boundless understanding and encouragement that greatly reduced research-related stress during my study period.

ABSTRACT

To deliver modern day broadband services to both fixed and mobile devices, ultra-high speed wireless networks are required. Innovative services such as the Internet-of-Things (IoT) can be facilitated by the deployment of next generation telecommunication networks such as 5G technologies. The deployment of 5G technologies is envisioned as a catalyst in the alleviation of spectrum congestion experienced by current technologies. With their improved network speed, capacity and reduced communication latency, 5G technologies are expected to enhance telecommunication networks for next generation services. These technologies, in addition to using current Long Term Evolution (LTE) frequency range (600 MHz to 6 GHz), will also utilize millimetre wave bands in the range 24-86 GHz. However, these high frequencies are susceptible to signal loss under rain storms. At such high frequencies, the size of the rain drop is comparable to the wavelength of the operating signal frequency, resulting in energy loss in the form of absorption and scattering by water droplets.

This study investigates the effect of intense rain storms on link performance to accurately determine and apply dynamic rain fade mitigation techniques such as the use of a combination of modulation schemes to maintain link connectivity during a rain event. The backpropagation neural network (BPNN) model is employed in this study to predict the state of the link for decision making in employment of dynamic rain fade mitigation. This prediction model was tested on all rainfall regimes including intense rain storms and initial results are encouraging. Further on, the prediction model has been tested on a rainfall event rainfall data collected over Butare (2.6078° S, 29.7368° E), Rwanda, and the results demonstrate the portability of the proposed prediction model to other regions. The evolution of $R_{0.01}$ (rain rate exceeded for 0.01% of the time in an average year) parameter due to intense rain storms over the region of study is examined and detailed analysis shows that this parameter is double the proposed ITU-R value of 60 mm/h. Moreover, an investigation on the largest rain drop size present in each rain storm is carried out for different storm magnitudes. The study goes further to examine the frequency of occurrence of rain storms using the Markov chain approach. Results of this approach show that rain spikes with maximum rain rates from 150 mm/h and above (intense storms) are experienced in the region of study with probability of occurrence of 11.42%. Additionally, rain spike service times for various rain storm

magnitudes are analyzed using the queueing theory technique. From this approach, a model is developed for estimation of rain cell diameter that can be useful for site diversity as a dynamic rain fade mitigation strategy. Finally, the study further investigates second-order rain fade statistics at different attenuation thresholds.

TABLE OF CONTENTS

LIST OF FIGURES

LIST OF TABLES

LIST OF ABBREVIATIONS

Acronym	Definition
ACM	Adaptive coding and modulation
ANN	Artificial neural network
BPNN	Backprogation neural network
CCDF	Complementary cumulative distribution function
CLM	Closed loop mode
DSD	Drop size distribution
FD	Frequency diversity
MLE	Maximum likelihood Estimation
MoM	Method of moments
OLM	Open loop mode
PSP	Pre-storm period
QTT	Queuing theory technique
RFD	Rain fade duration
SD	Site diversity
SOS	Second order statistics
SP	Storm period
TD	Time diversity
UPLC	Uplink control

LIST OF SYMBOLS

Symbol	Meaning
Π_S	Final state probability matrix for storm regime
Π_{Sh}	Final state probability matrix for shower regime
A_{sp}	Specific attenuation
b_H	Hidden layer bias vector
b_O	Output layer bias input
D_{ev}	Rain event diameter
D_{max}	Maximum drop diameter
D_{sp}	Rain spike diameter
$F_{D,mn}$	Mean fade duration
$F_{D,mx}$	Maximum fade duration
f	ANN Activation function
f_{rq}	Frequency
N_{tot}	Total number of fades
$N_{tot(A)}$	Total number of fades at attenuation threshold, A dB
O_{BP}	BPNN output
O_t	Target output or actual output
$P_{ij,S}$	State transition matrix for storm rainfall regime
$P_{ij,Sh}$	State transition matrix for shower rainfall regime
P_Z	Year period X
R	Rain rate in mm/h
$R_{0.01}$	Rain rate exceeded at 0.01% of time of an average year in mm/h
$R_a(t + 1)$	Actual rain rate at time $(t + 1)$ in mm/h
$R_a(t)$	Actual rain rate at time (t) in mm/h
R_m	Spike maximum rain rate in mm/h
R_{max}	Event maximum rain rate in mm/h

$R_p(t + 1)$	Predicted rain rate at time $(t + 1)$ in mm/h
$R_p(t)$	Predicted rain rate at time (t) in mm/h
S_X	Type X storm
S_{xyz}	Type X storm, part y, year period Z
t_{arr}	Spike interarrival time
t_{ov}	Spike overlap time
t_{st}	Spike service time
w_{HI}	Input weight matrix vector
w_{OH}	Hidden layer matrix vector

CHAPTER 1

General introduction

1.1 Introduction

Wireless communication links operating at frequencies above 10 GHz provide the much needed bandwidths for fast and efficient communication via satellite and terrestrial links. The advent of 5G technologies brings about benefits of faster speeds, higher bandwidths and lower latency down to 1 ms or less. For instance, the first outdoor trial of 5G technology in Africa was carried out by South Africa's network operator, MTN, in collaboration with Huawei as reported in [*Jamie, 2018*]. In this trial, MTN reached download and upload speeds of 530 Mbps and 79 Mbps respectively, with a latency of 7 ms which were measured using an online speed test. During the test, 100 MHz bandwidth was allocated in the 28 GHz spectrum. However, when operating at such high frequencies in the spectrum, the link may not be guaranteed to provide a high efficiency service due to signal outages resulting from signal absorption and scattering by rain drops under rainy conditions. This eventually leads to signal attenuation and, therefore, strategies have to be put in place to ensure that even in the presence of rain storms, the wireless link is at least available for at least 99.99% of the time or more of an average year.

1.2 Problem formulation and motivation

Recent studies and literature over South Africa have revealed that there has been an increase in rainfall over most parts of the country. *McKellar et al.,* [*2014*] carried out a study on climatic trends in rainfall and temperatures over a period of 50 years (1960-2010) for South Africa. Results of their analysis show that there was a significant increase in rainy days over the KZN region. A more recent study on historical rainfall trends was done by *Krugger and Nxumalo* [*2017*] and analysis of their results show that, in general, most parts of the country experienced an increase in the intensity of daily rainfall. Over Durban, rain measurements have shown an increase in both the number of storms and their magnitudes. For instance, an intense rain storm with a maximum rain rate of 253.066 mm/h was recorded on 11th March 2016 from 18:50:30 hours to 22:37:30 hours.

This rain rate is much higher compared to the previous highest rain rate of 88.0419 mm/h that was recorded on 3rd December 2013 from 13:35:00 hours to 14:05:30 hours. This study therefore undertakes to investigate, among others, the effect of the rise in the number and duration of storms on the communication wireless links by searching for answers to the following research questions:

- Does the upward rise in the number of storms alter the long-term $R_{0.01}$ parameter?
- To what extend do these high magnitude rain storms alter the rain drop size distributions?
- With high variability of rain in both space and time, can an artificial neural network be employed for prediction of rain attenuation?
- What is the minimum distance of separation for two earth stations deployment for space diversity as a rain-mitigation measure?
- What is the probability of occurrence of intense rain storms over the region of study and how long do resultant fades last?

1.3 Objectives

a) To determine the new $R_{0.01}$ parameter with the sudden occurrence of rain storms and the effect of rain storm magnitudes on the maximum rain drop size distribution over Durban.
b) To explore the use of the backpropagation neural network in prediction of link condition for dynamic rain fade mitigation
c) To use queueing theory approach to for determining rain spike queueing parameters and distributions
d) To investigate the probability of occurrence of deep fades using Markov chains and fade duration statistics at different fade thresholds

1.4 Dissertation overview

This chapter introduces the work that has been carried in this study and provides the problem formulation and motivation for this study in addition to contributions that have been made. *Chapter 2* provides the literature review on the topical areas that are related to this study. In *Chapter 3*, we investigate the effect of intense rain storms on long-term $R_{0.01}$ parameter and the effect of these storms on rain drop size distributions. In *Chapter 4*, an investigation is carried out to show the application of the backpropagation neural network (BPNN) for rain attenuation prediction. In

Chapter 5, the queuing theory and Markov chain techniques are used to predict link outages during intense rain storm events. Rain fade duration statistics are investigated in *Chapter 6* for application with dynamic rain fade mitigation techniques. Conclusions are presented in Chapter 7.

1.5 Original contributions

- Determination of the new $R_{0.01}$ parameter over Durban
- Examination of effects of storm magnitudes on rain attenuation using measured drop size distributions
- Rain attenuation prediction using the backpropagation neural network for application of dynamic rain fade mitigation
- Determination of rain cell diameters using queueing parameters for space diversity mitigation technique
- Investigation of the most predominant spike magnitudes using Markov chains
- Determination of second order rain fade statistics for site diversity rain fade mitigation

1.6 Publications – Journal and Conferences

1) Mary N. Ahuna, Thomas J. Afullo, Akintunde A. Alonge, "Outage Prediction during Intense Rainstorm Events Using Queuing Theory and Markov Chains Over Radio Links", *Progress In Electromagnetic Research M*, Vol. 73, pp. 183-196, 2018.

2) Mary N. Ahuna, Thomas J. Afullo and Akintunde A. Alonge, "Rain attenuation prediction using artificial neural network for dynamic rain fade mitigation," *SAIEE Africa Research Journal*, Vol. 110(1), pp. 11-18, March 2019.

3) Mary N. Ahuna, Thomas J. Afullo and Akintunde A. Alonge, "Rainfall rate prediction based on artificial neural networks for rain fade mitigation over earth-satellite link" *Proceedings of IEEE AFRICON Conference*, Cape Town, South Africa, pp. 579-584, 18th – 20th September 2017.

4) Mary N. Ahuna and Thomas J. Afullo, "Effects of storm attenuation over satellite links in sub-tropical Africa" *The 40th PIERS 2018 Conference*, 1st – 4th August 2018, Toyama, Japan, p. 153.

5) Mary N. Ahuna and Thomas J. Afullo, "Rain fade duration statistics over Ku-band radio links in sub-tropical South Africa" *South African Telecommunications Network and Applications Conference* (SATNAC), Cape Town, South Africa, 2nd – 5th September 2018, pp. 434-438.

6) Mary N. Ahuna, Thomas J. Afullo and Akintunde A. Alonge, "Specific rain attenuation dependence on rain storm magnitudes and measured drop sizes" *IEEE Radio 2018 Conference,* 15th-18th October, Hilton Resort and Spa, Wolmar, *Mauritius,* 2018.

1.7 Chapter Summary

An introduction to the rest of thesis has been presented in this chapter, with the problem statement and motivation, in addition to contributions made in this study. In the next chapter, a literature review on related topics will be presented.

CHAPTER 2

Literature Review and Related Work

2.1 Introduction

A general introduction was done in the previous chapter providing highlights on the problem formulation and motivation for this work. In this chapter, a literature review is carried out on related works and topics that provide background on the work that has been done in this study.

2.1.1 Wireless Communication and Technologies

Wireless and optical fiber access networks play a key role of providing access to information. Each of these two technologies has its own limitations. For instance, the optical fiber provides a huge amount of bandwidth and effectively high speeds, but this cable cannot reach everywhere. On the other hand, wireless communication networks can potentially reach everywhere, but their communication channel that is highly susceptible to atmospheric and environmental impairments.

Frequencies above 10 GHz provide large bandwidths for fast and efficient communications through satellite and terrestrial links [*Matricciani and Riva, 2005*; *Cheffena and Amaya, 2008; ITU-R P.618, 2017; Foty et al., 2011*]. Rolling out of 5G technologies brings about benefits of fast speeds and lower latency. For successful implementation of these technologies, wireless communication links are desired to experience close to zero outages. Unfortunately, communication links operating at 7 GHz and above may not be guaranteed to provide the intended service due to signal fading caused by rain drops through processes of absorption and scattering [*Matricciani, 1997; ITU-R P.530-17, 2017*]. Link designers, in the quest to provide reliable service, strive to achieve link availabilities of at least 99.99% of an average year or better.

2.1.2 Wave Propagation and Atmospheric Effects

Communication systems that operate at frequencies above 18 GHz and especially those with lower elevation angles may suffer a great deal due to multiple sources of simultaneously occurring atmospheric attenuation. These sources of attenuation include rain, clouds, gas and tropospheric scintillation. ITU-R [*ITU-R P.618-13, 2017*] provides an equation for determining total attenuation due to these multiple sources:

$$A_{tot}(p) = A_G(p) + \sqrt{\left(A_R(p) + A_C(p)\right)^2 + {A_S}^2(p)} \qquad [dB] \tag{2.1}$$

where A_G is the attenuation due to gas (vapor and oxygen), A_R is the attenuation due to rain, A_C is attenuation due to clouds, A_S is attenuation due to atmospheric scintillation and p is the probability of attenuation being exceeded in the range 50% to 0.001%. It is to be noted that A_C and A_G are considered at p = 1 [*ITU-R P.618-13, 2017*].

2.2 Rain Rate Prediction Models

Prediction of the rain intensity, R mm/h, that is exceeded for different percentages of an average year is important in the design of reliable communication links. ITU-R [*ITU-R P.618-13, 2017*] recommends a rain rate, $R_{0.01}$, that is exceeded for 0.01% of an average year for design of communication links that can guarantee link availability of up to 99.99%. There are a number of rain rate prediction models in existence that can be used to obtain this long-term parameter such as *Rice and Holmberg* [1973], *Olsen* [1999], *Dissanayake et al.* (2002), *Ojo et al.* (2008), *Chun and Mandeep* (2013). More details on these models are given in *Ahuna et al.* (*2016*b).

Further, ITU-R recommends $R_{0.01}$ be determined using data sampled at 1-minute integration time. Regions where only higher integration time data are available, estimation of rain rates exceeded can be obtained using rain rate conversion models. A review on integration time conversion models was carried out by *Emiliani et al.* (2009) by grouping these models into three broad categories of physical, analytical and empirical (*See Appendix 1*). Physical models are based on physical processes that are involved in the formation and development of rain. In analytical models, the rain rate CDF is assumed to be represented by a given function and the Moupfouma model is an example of such models. Most common models combine physical with stochastic/analytical approaches in their modelling. Two examples of such models are the EXCELL [*Capsoni et al., 1987*] and the Lavergnat (LG) model [*Lavergnat, 1998*]. In the conversion of cumulative distribution function from an integration time, t_1, toa target integration time, t_2, the LG model achieves this by using a conversion factor, *CF*, given by:

$$CF = \frac{t_1}{t_2} \tag{2.2}$$

$$P_2(R_2) = CF^a P_1(R_1) \tag{2.3}$$

$$R_2 = \frac{R_1}{CF^a} \tag{2.4}$$

Where $P_2(R_2)$ is the probability that a certain rain rate, r_2, is greater than R_2 in the target integration time, t_2, $P_1(R_1)$ is the probability that a certain rain rate r_1 is greater than R_1 in the integration time, t_1, while a is a parameter that is empirically determined.

Empirical models give simple analytical laws that show the relationship between equiprobable rain rate values. These models are the most common because functions for these models are relatively simple to generate whenever cumulative distributions for both integration times are available. Examples of empirical models include the *Flavin,* (*1982*) model and the ITU-R P.837-5 (2007) model. In the absence of precipitation measurements, this parameter can be obtained from rain maps proposed by ITU-R [*ITU-R P.837-7, 2017*] as given in *Appendix 2*. For instance, four long-term rainfall rate prediction models are briefly discussed in this section. These models are the Moupfouma model [*Moupfouma, 1987*], Moupfouma and Martins model [*Moupfouma and Martins, 1995*], the Rice-Holmberg model [Rice and Holmberg, 1973] and Crane rain rate models [*Crane, 1982; Crane, 1996*].

2.2.1 The Moupfouma Model

A three-parameter model that resembles an exponential distribution at higher rainfall rates and lognormal distribution at lower rainfall rates was developed by *Moupfouma* [*Moupfouma, 1987*] for prediction of rainfall rates exceeded at various percentages, *P*, of time in an average year. This model is expressed as:

$$P(R \geq r) = 10^{-4} \left(\frac{R_{0.01}}{r}\right)^b e^{\left(\lambda r^{1-s}\left[\left(\frac{R_{0.01}}{r}\right)-1\right]\right)} \tag{2.5a}$$

with

$$b = 8.22(R_{0.01})^{-0.584} \tag{2.5b}$$

$$\mu = \lambda r^{-s} \tag{2.5c}$$

where P is the probability that rainfall rate R in [mm/h] exceeds a value r, and $R_{0.01}$ is the rain rate exceeded for 0.01% of the time of an average year, whereas parameters λ and s are as given in [*ITU-R, P.837-1, 1994*] according to different climatic zones.

2.2.2 The Moupfouma and Martins Model

In 1995, Moupfouma and Martin [*Moupfouma and Martins, 1995*] improved on the model in (2.5a) by developing a model that could perform better for both temperate and tropical regions. This model is given as:

$$P(R \geq r) = 10^{-4}\left(\frac{R_{0.01}}{r+1}\right)^{b} e^{[\mu(R_{0.01}-1)]} \qquad (2.6a)$$

with:

$$b = \left(\frac{r - R_{0.01}}{R_{0.01}}\right) ln\left(1 + \frac{r}{R_{0.01}}\right) \qquad (2.6b)$$

$$\mu = \left(\frac{9.21}{R_{0.01}}\right) e^{\left[-\lambda\left(\frac{r}{R_{0.01}}\right)^{\gamma}\right]} \qquad (2.6c)$$

where $\lambda = 1.066$ and $\gamma = 0.214$ and $R_{0.01}$, p and r are as defined in (2.5a).

2.2.3 Rice-Holmberg (R-H) Rain Rate Model

In this model, rain rate distributions are developed from Mode 1 rain (thunderstorms) and Mode 2 rain (other rain), with the total distribution, *M*, being the sum of the two modes and given as [*Rice and Holmberg* 1973; *Dissanayake et al.*, 1997; *Dissanayake et al.*, 2003]:

$$M = Mode\ 1 + Mode\ 2 \quad [mm] \qquad (2.7)$$

and

$$P(R) = \frac{M}{87.6}\{0.03\beta e^{-0.03R} + 0.2(1-\beta)[e^{-0.258R} + 1.86e^{-1.63R}]\} \quad [\%] \qquad (2.8)$$

where *P(R)* is the percentage of the year the rain rate *R* mm/h is exceeded, *M* is the average annual accumulation of rainfall in mm, whereas β is the thunderstorm component of *M*. Values of β and *M* can be obtained from world maps given in *Rice and Holmberg* [1973], or can be obtained from the relation [*Rice and Holmberg*, 1973; *Dissanayake et al.*, 2002]:

$$\beta = \frac{M_1}{M} \qquad (2.9)$$

where M_1 is the mean annual accumulation of thunderstorm rain in mm and M is defined in (2.5). Alternatively, β can be determined as:

$$\beta = \beta_0[0.25 + 2e^{-0.35}(1 + 0.125M)/U] \tag{2.10a}$$

$$\beta_0 = 0.03 + 0.97e^{-5exp(-0.004M_m)} \tag{2.10b}$$

where *U is the* average number of thunderstorm days expected during an average year and M_m is the highest monthly precipitation observed in the total period of the experiment. *Dutton and Dougherty* [1974] extended the R-H model to include an attenuation prediction property, and the modified model becomes:

$$P(R) = \begin{cases} 0.0114(T_{11} + T_{12})e^{-\frac{R}{R_1'}}, & R < 5\ mm/h \\ 0.0114T_{21}exp\left(-\sqrt[4]{\frac{R}{R_{21}}}\right) & 5 \le R \le 30 \\ 0.0114T_{11}exp(-R/\bar{R}_{11}) & R > 30 \end{cases} \quad [\%] \tag{2.11}$$

where T_{11}, T_{21}, R_1' and $\bar{R}$ are linear combinations of M, β and D = 24 + 3M and are determined from regression equations.

2.2.4 Crane Rain Rate Models

In 1980, the popularly known as the Crane Global model was developed by Crane (1980) for rain rate prediction. Two years later, Crane (Crane, 1982) proposed his second model known as the two-component Crane model. This was a closed-form distribution model that handles contributions from volume cells and debris separately during link calculations. The empirical rain rate distributions function, $P(r \geq R)$, of the model is given as [*Crane, 1996; Ahuna 2016b*]:

$$P(r \geq R) = P_C(r \geq R) + P_D(r \geq R) - P_{CD}(r \geq R) \tag{2.12a}$$

with

$$P_C(r \geq R) = P_C e^{-R/R_C} \tag{212b}$$

$$P_D(r \geq R) = P_N N\left(\frac{lnR - lnR_D}{S_D}\right) \tag{2.12c}$$

$$= \frac{P_D}{\sqrt{2\pi}S_D}\int_R^{\infty} exp\left[\frac{1}{2}\left(\frac{ln(2/R_D)}{S_D}\right)^2\right] \quad (2.12d)$$

$$P_{CD}(r \geq R) = P_C(r \geq R)P_D(r \geq R) \approx 0 \quad (2.12e)$$

where r and R are rain rates in mm/h, $P_C(r \geq R)$, $P_D(r \geq R)$ and $P_{CD}(r \geq R)$ are the CDFs for volume cells, debris and joint CDF for volume cells and debris respectively, P_C and P_D are probability of cell and debris respectively, N is the normal distribution function, R_C and R_D are average rain rate in cell and median rain rate in debris respectively, and S_D is the standard deviation of natural logarithm of rain rate.

2.2.5 Application of the Artificial Neural Network for Rainfall Prediction

An artificial neural network (ANN) is an interconnection of nodes designed to solve problems that would prove difficult or complex to solve by humans or statistical methods. This computation model works by mimicking the functions of biological neural networks (neurons) [*Rojas, 1996*]. An example of a multilayer neural network is shown in Figure 2.1, showing input patterns, internal representation and output patterns. There are different kinds of neural networks that can be used for different tasks such as forecasting (stock market, weather), character recognition (for fraud detection in banks), cancer detection (in medicine), satellite imagery and natural language processing.

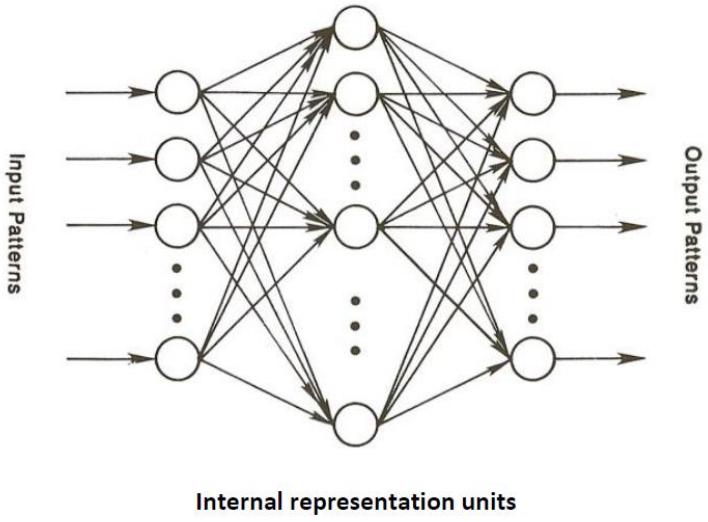

Figure 2.1 Multilayer neural network

The feedforward neural network (FNN) is the simplest type of ANN in which data moves only in one direction, from input to the output with the goal of approximating some function, *f*. An example of the feedforward network is shown in Figure 2.2 and this king of network is utilized in medicine (X-ray) (*Jian and Wu, 2010*). Another kind of ANN is the Convolutional neural network (CNN) that was developed by Yann and his collaborators in 1998 [*LeCun et al., 1998*]. This network was used as a recognizer for handwritten digits under the name LeNet. The CNN is widely used for image and audio processing. For recurrent neural networks, they are commonly used for sequence prediction or time series forecasting [*Kim, 2014; Brownlee, 2017*]. A variant of this network is the long short-term memory (LSTM) that is widely used for sequence prediction problems. Other variants of ANNs exist for different applications, but the most commonly used network for prediction/forecasting is the classical feedforward network known as the *backpropagation neural network*, which is discussed at length in Chapter 4.

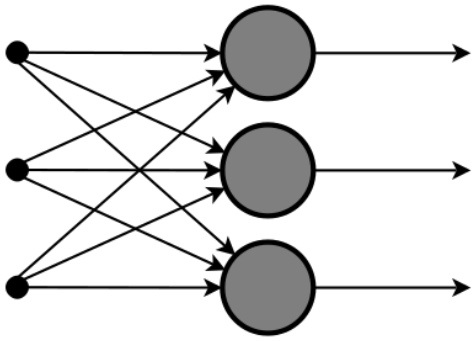

Figure 2.2 Feedforward neural network

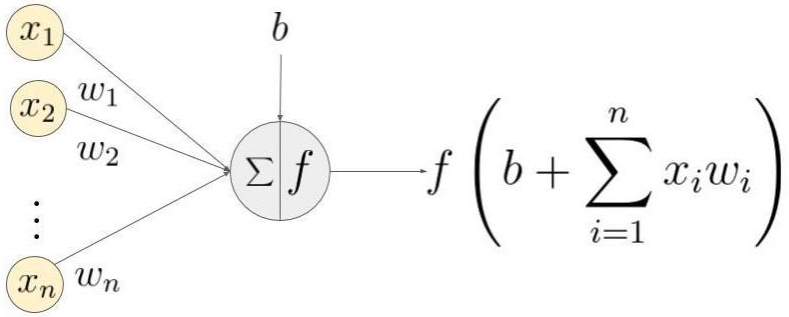

Figure 2.3 Basic ANN showing an activation function, *f*

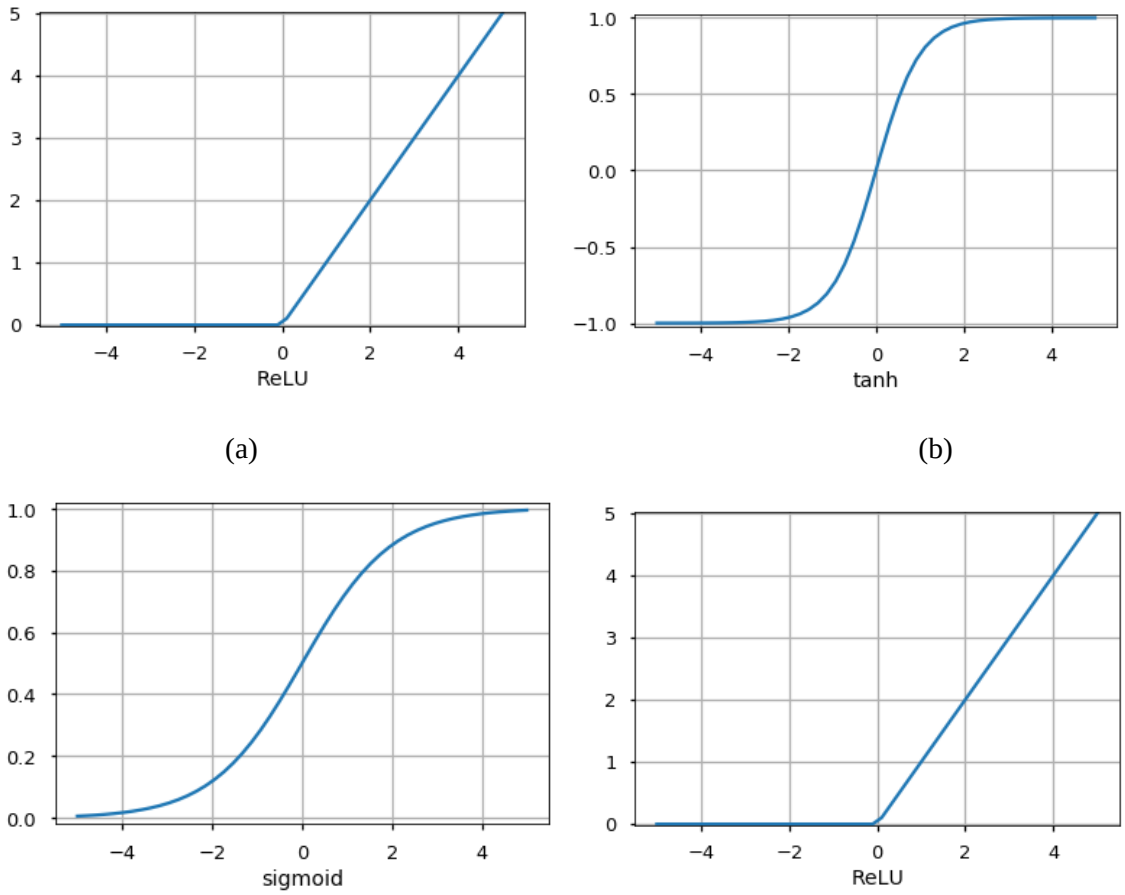

(a) (b)

(c) (d)

Figure 2.4 Variants of ANN activation functions (a) Linear (b) Rectified Linear Unit (c) Sigmoid (d) Tanh

An artificial neural network uses an activation function, *f*, for decision-making and Figure 2.3 shows a sample of an activation function at the output of the network. Some notable activation functions are the *Linear* function, the *Rectified Linear Unit* (ReLu), the *Sigmoid* function, and the *Tanh* function as shown in Figure 2.4 with their functions given as:

$$f_{lin}(x) = kx \tag{2.13}$$

$$f_{ReLu}(x) = \begin{cases} 0 & ; \quad x < 0 \\ x & ; \quad x \geq 0 \end{cases} \tag{2.14}$$

$$f_{sig}(x) = \frac{1}{1 + e^{-x}} \tag{2.15}$$

$$f_{tan}(x) = \frac{2}{1 + e^{-2x}} \tag{2.16}$$

where f_{lin}, f_{ReLu}, f_{sig}, $f_{\tan}$ are linear, *Rectified Linear*, *Sigmoid* and *Tanh* functions, respectively, with x being the input variable.

Atmospheric processes from which rainfall is formed have been known to be complex and may not be accurately modelled using mathematical or statistical models. The artificial neural network (ANN) is known to predict these random variables reasonably well with non-linear relationships. Earlier studies have been carried out on the application of the ANN for rainfall prediction especially in the field of meteorology and water management [*Abhishek et al., 2012; Michaelides et al., 1995; Luk et al., 2001; Hung et al., 2009; Purnomo et al., 2017*]. The use of an artificial network was employed by *French et al.* [*1992*] to predict a two-dimensional rainfall, one hour ahead in time. This work laid a good foundation for form most researchers in this field. Over Cyprus, estimation of missing rainfall data was done using the artificial neural network together with daily rainfall observations in the neighboring sites [*Michaelides et al., 1995*]. In 2004, *Christodoulou et al.* [*2004*], using radar data as inputs and rain gauge data as outputs, trained the self-organizing map (SOM) and the K-Nearest Neighbor (KNN) machine learning classifiers to predict rainfall rates in Italy. These earlier studies have motivated new researchers to venture into application of machine learning algorithms for prediction of rainfall.

2.3 Rain Attenuation Prediction

The prediction of long-term rain attenuation is important in the design of microwave links that can be highly available and reliable. The rain attenuation probability distribution function, $P(a > A)$ is the main objective in all attenuation prediction models. Some of these include the Bryant model [*Bryant et al., 2001*], the Crane two-component model [*Crane, 1982*] and the widely used ITU-R P.618 model [*ITU-R P.618-13, 2017*].

2.3.1 ITU-R Prediction Model

ITU-R [*ITU-R P.618-13, 2017*] provides a model for estimation of rain attenuation exceeded for 0.01% of an average year. This model is given as:

$$A_{0.01}(dB) = \gamma \times r \times L_s \qquad [\mathrm{d}B] \qquad (2.17)$$

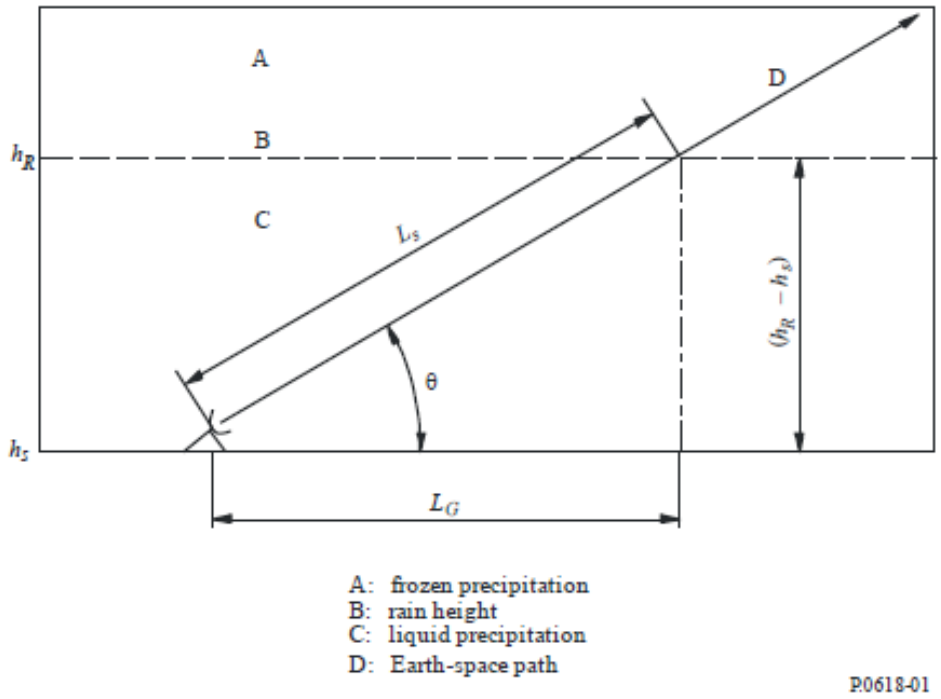

Figure 2.5 Earth-space link parameters [ITU-R P.618-13, 2017]

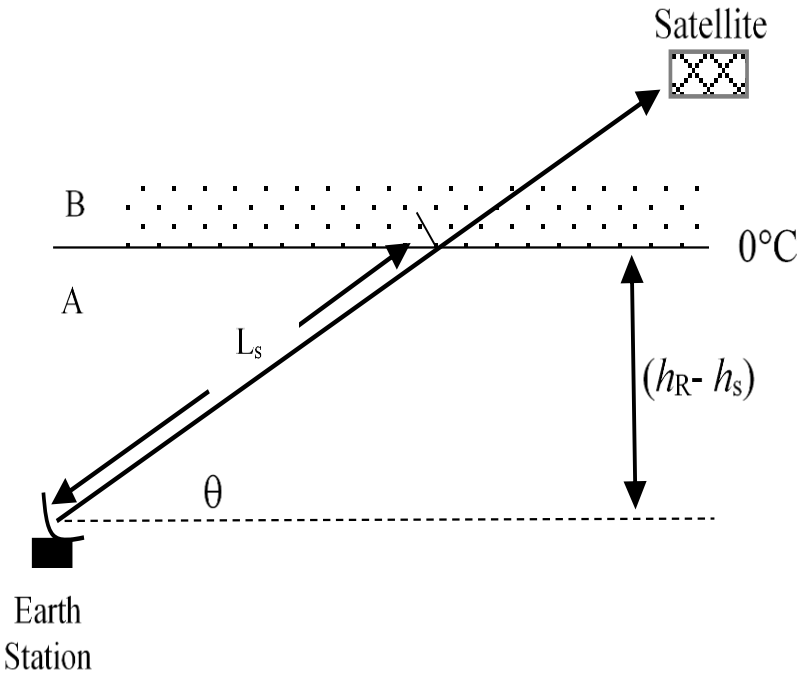

Figure 2.6 Earth-satellite slant path

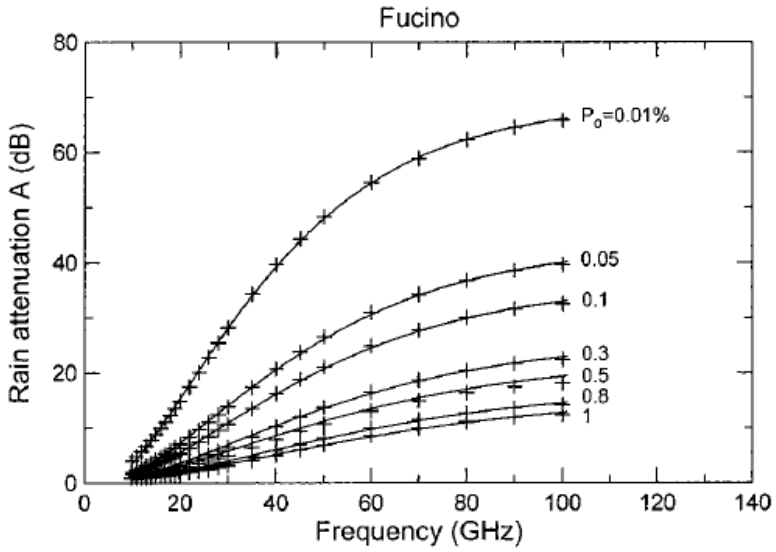

Figure 2.7 Rain attenuation as a function of frequency and outage probability, *P*o %, in an average year at Fucino [*Matricciani and Riva, 1998*]

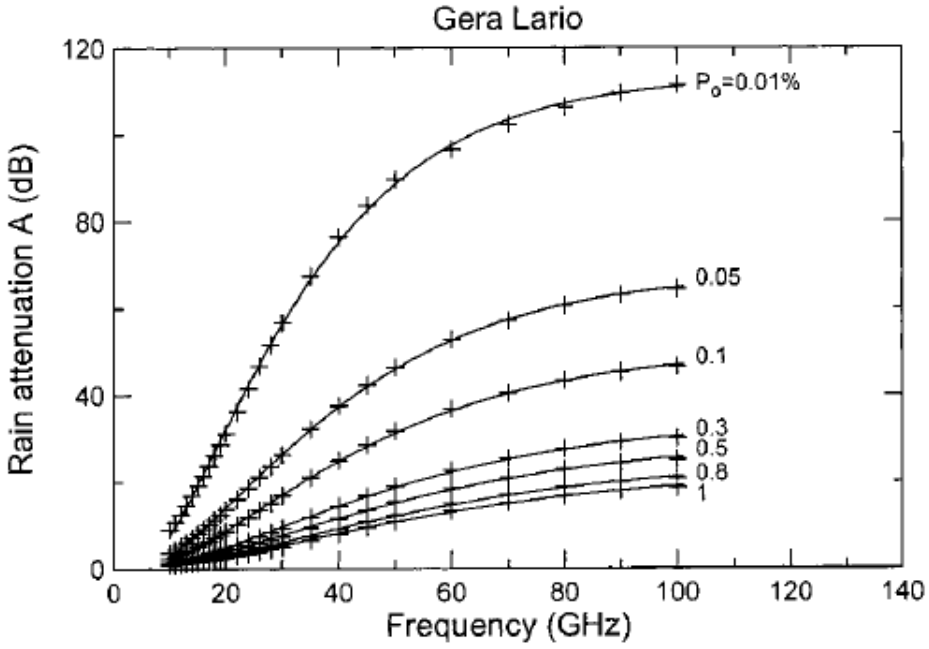

Figure 2.8 Rain attenuation as a function of frequency and outage probability, *P*o %, in an average year at Gera Lario [*Matricciani and Riva, 1998*]

where r is the path length adjustment factor, L_s is the slant path length in km (*see* Figure 2.5) and γ, in dB/km, is the specific rain attenuation as obtained in [*ITU-R P.838-3, 2005*]. An estimate of long-term attenuation statistics for other percentages of an average year in the range 0.001% to 5% are given as [*ITU-R P.618-13, 2017*]:

$$A_p(dB) = A_{0.01}\left(\frac{p}{0.01}\right)^{-0.655+0.033\ln(p)-0.045\ln(A_{0.01})-\beta(1-p)sin\theta} \tag{2.18}$$

where p is the probability of exceedance in %, A_p is attenuation exceeded p % of time in an average year, θ is the angle of elevation of the earth station antenna, k and α are parameters dependent on frequency and β is the parameter dependent on the latitude of the earth station and obtained from *ITU-R P.618-13* [*2017*] as:

$$\beta = \begin{cases} 0 & ; \quad p \geq 1\% \text{ or } |\varphi| \geq 36° \\ -0.005(|\varphi| - 36) & ; \quad p < 1\% \text{ and } |\varphi| < 36° \text{ and } \theta \geq 25° \\ -0.005(|\varphi| - 36) + 1.8 - 4.25\sin\theta & ; \quad \text{Otherwise} \end{cases} \tag{2.19}$$

where φ is the latitude of the earth station in degrees and θ is defined in (2.10).

2.3.2 Rain Attenuation Prediction Using Synthetic Storm Technique (SST)

A rain attenuation prediction model using the SST approach was proposed by *Matricciani* (1996). In this model, the vertical structure of rain is modelled using two layers, A and B, as shown in Figure 2.6, where layer A is made up hydrometeors in form of rain drops at 20°C, whereas layer B is the melting layer at 0°C. With an assumption that the rain in layer A is uniform, using simple physical hypotheses, Matricciani (1996) showed that the rain rate in the melting layer, also termed 'apparent rain rate', is assumed to be uniform and may be estimated as:

$$R_B = 3.134R_A \qquad [\mathrm{d}B] \tag{2.20}$$

where R_B and R_A are rain rates in layer B and layer A, respectively.

Matricciani and Riva (1998), using data collected over Fucino and Gera Lario, estimated the $P(a > A)$ function using the SST. They also derived a function that associated the attenuation, A, with the carrier frequency, f_{rq}, for fixed probabilities in the frequency range of 10 GHz to 100 GHz. These results are shown in Figure 2.7 and Figure 2.8 for Fucino and Gera Lario, respectively. The function of association is given as:

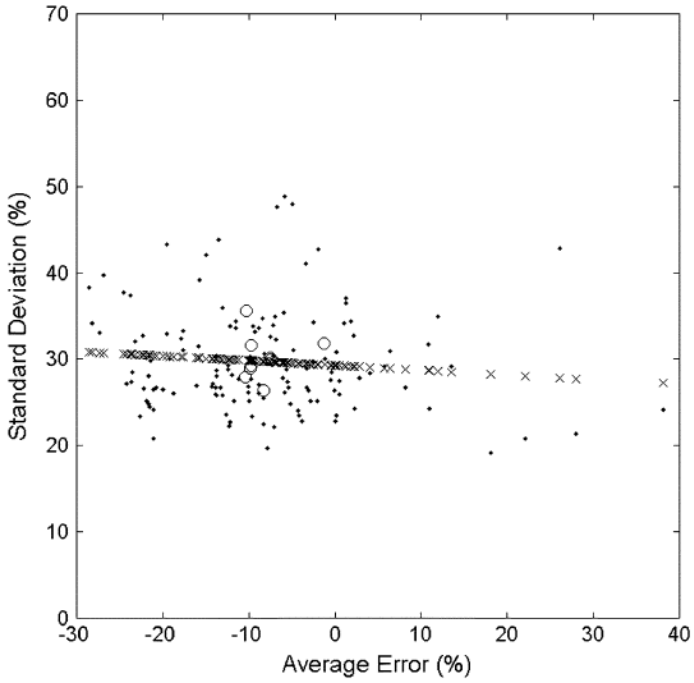

Figure 2.9 Error standard deviation for 15 rain attenuation models [*Matricciani and Riva, 2005*]

$$A(f_{rq}) = C_1 e^{\delta_1 f_{rq}} + C_2 e^{\delta_2 f_{rq}} - (C_1 + C_2) \tag{2.21}$$

where f_{rq} in GHz is the carrier frequency while C_1, C_2, δ_1 and δ_2 are functions of probability as given in *Appendix 3* and *Appendix 4* for Fucino and Gera Lario, respectively. A further search for the most reliable long-term rain attenuation CDF on a slant path was carried out by Matricciani

and Riva (2005). This study was motivated by relatively large errors when existing prediction results were tested on beacon measurements. This study was carried out using data collected over Spino d'Adda and independent predictions of the synthetic storm technique for the same radio link. Figure 2.9 shows a scatter plot of standard deviation of the error, ϵ, for 15 prediction models.

2.4 Rain Fades and Mitigation Techniques

This section gives an overview of second order rain fade statistics and thereafter, a summary of some of the rain fade mitigation techniques that can be employed to mitigate these fades is provided.

2.4.1 Second Order Rain Fade Statistics

The three most important parameters that become inputs to dynamic rain fade mitigation schemes are the rain fade duration, the inter-fade duration and the fade slope, with the former parameter determining the length of time a communication link is subjected to an outage. In 1982, Cox and *Arnold* [*1982*] investigated fade durations on a slant path link operating at 19-GHz and an elevation angle of 18.5°. Results of this investigation showed that the median fade durations range between 2.8 to 7.5 minutes at fade thresholds in the range of 5 dB to 40 dB. Another research on prediction of long-term fade duration statistics was carried out by *Matricciani,* [*1997*] on the slant path by simulating time series using the synthetic storm technique (SST). Results of this study showed that predicted and measured rain fade durations longer than approximately 64-128 sec are quite similar. In addition, researchers on this topic agree that fade durations at 5 dB to 20 dB thresholds tend to follow a lognormal distribution [*Lin, 1973; Paraboni and Riva, 1994; Dao et al., 2012, ITU-R, P.618-13, 2017*]. For instance, a double lognormal model for prediction of rain fade duration statistics was developed by *Cheffena and Amaya* [*2008*] using data collected from links operating at frequencies ranging from 11 GHz to 50 GHz and elevation angles from 14° - 89°. This model is given by:

$$P(d > D|a > A) = \alpha \frac{Q\left(\frac{\ln(D/m_s)}{\sigma_s}\right)}{Q\left(\frac{\ln(1/m_s)}{\sigma_s}\right)} + (1-\alpha)\alpha \frac{Q\left(\frac{\ln(D/m_r)}{\sigma_r}\right)}{Q\left(\frac{\ln(1/m_r)}{\sigma_r}\right)} \tag{2.22}$$

where $P(d > D|a > A)$ is the probability of occurrence of fades with duration d longer than D sec and having attenuation a greater than A dB, with $D \geq 1$ s, Q being the standard cumulative distribution for a normally distributed variable defined in [*ITU-R, P.1623, 2005; Cheffena and Amaya, 2008*]. Equations for determining vales for α, σ_s, d_r, m_s and m_r are given in [*Cheffena and Amaya, 2008*] as:

$$\propto = 0.8881 - 0.3168\beta^3 + 0.1636e^{\left(-\frac{A}{2.61}\right)} \tag{2.23a}$$

$$m_s = 0.3636 - 2.0411 \times 10^{-6} f^3 + 0.11117e^{(-\epsilon)} \tag{2.23b}$$

$$\sigma_s = 1.6462 + 29.8038e^{\left(-\frac{f}{3.5}\right)} - 1.3671 \times 10^{-6} A^3 \tag{2.23c}$$

$$m_r = 686.59 - 173.51\log(f) \tag{2.23d}$$

$$\sigma_r = 0.6210 + 4.3516 \times 10^{-3} f^{1.5} + 3.3637 A^{-2} \quad (2.23e)$$

where A is the attenuation threshold in dB, m_s and d_s are the mean and standard deviation of the first lognormal function, m_r and d_r are the mean and standard deviation of the second lognormal function, $\in$ is the elevation angle in the range 5 to 90°, f is the frequency in the range 10 GHz to 50 GHz, α defines the fraction of fades related with each lognormal function and β is the rain connectivity parameter whose value is estimated in ITU-R P.837-4 [2007] for different locations.

Similarly, *ITU-R, P.1623,* [*2005*] provides guidelines on how to determine fade duration statistics through two independent cumulative functions given by:

$$P(d > D|a > A) = \frac{N(d > D|a > A)}{N_{tot(A)}} \quad (2.24)$$

and

$$F(d > D|a > A) = \frac{T(d > D|a > A)}{T_{tot(A)}} \quad (2.25)$$

where $P(d > D|a > A)$ is as defined in (2.13), $N(d > D|a > A)$ is the number of fades with duration d lasting longer than D s, $N_{tot(A)}$ is the total number of fades observed at the given attenuation threshold, $F(d > D|a > A)$ is the probability of occurrence of fades with durations d longer than D sec, $T(d > D|a > A)$ is the total fading time due to fades of durations longer than D sec given that the threshold attenuation A is exceeded, $T_{tot(A)}$ is the total exceedance time at attenuation threshold A dB, $F(d > D|a > A)$, is the probability of occurrence of fades lasting with durations d longer than D s. It is to be noted that the ITU-R model is only valid for fade durations longer than 1 sec with model input parameter, A in dB, elevation angles from 5° to 60° and frequency *f*, such that $10 \leq f \leq 50$ GHz.

2.4.2 Rain Fade Mitigation Techniques

The two main propagation effects that are of great concern to system designers are attenuation effects and depolarization effects. Rain is the main cause of attenuation on wireless links, and has thus attracted the attention of researchers seeking ways of mitigating these effects. Rain fade mitigation schemes can broadly be divided into two categories: (1) static rain fade mitigation techniques (SRFMTs) and dynamic rain fade mitigation techniques (DRFMTs). The common

SRFMT considers the assignment of a static fade margin equivalent to a rain rate that results into a link availability of 99.99% during an average year [*ITU-R 618-13, 2017; ITU-R P.530-17, 2017*]. One main advantage of this method is its simplicity. On the other hand, the main shortcoming is that the method is uneconomical due to power assignment even during dry spells. Further, employment of this method leads to link outages during intense rain storms with rain rates way above predicted rates.

More economical and reliable methods such as adaptive coding and modulation (ACM), adaptive power control and diversity techniques consider the random behavior of signal attenuation and are put in place when needed and hence improving link efficiency and availability. Most of these methods employ feedback channels that aid in determining the state of the link and hence employ power-on-demand fade mitigation techniques [*Nakazawa et al., 2010*].

A. Power Control Techniques

Power control, as a rain fade mitigation technique, is achieved by varying the EIRP of the signal to improve the carrier-to-noise (C/N) ratio. In adaptive power control systems, the power is adjusted to compensate for fluctuations in the signal attenuation along the path. This method is commonly referred to as *uplink power control* (ULPC) and can be achieved in two modes: open loop mode (OLM) or closed loop mode (CLM). When operating in the open loop mode, the likely fade level on the link is predicted using the downlink signal and the power is adjusted accordingly. In the closed loop mode, the satellite is used to detect the received signal level and sends a control signal back to the earth station for adjustment of the transmitted power in accordance with the state of the link. The CLM is viewed as the most accurate mode, though more expensive than the OLM.

B. Signal Processing Technique

This processing is handled onboard the transponder by translating the uplink signal from the earth station to the baseband through demodulation, demultiplexing and decoding processes. Each incoming packet is processed in the baseband level, and this makes it possible for most of the bit errors to be detected and removed. The transmitting station is eventually alerted for cases where energy levels of their transmitted packets are below defined thresholds.

C. Diversity Techniques

These techniques include time diversity (TD), frequency diversity (FD) and site diversity (SD). In the common TD scheme, the same signal is transmitted twice with an appropriate time delay between the two transmissions. At the receiving end, the two signals are compared and the strongest is chosen. The possibility of one signal being stronger than the other is strengthened by the fact that most rain fades have limited time spans [*Panagopoulos et al. 2004*]. The diversity gain parameter determines the performance of any diversity technique and is defined as the path attention difference between attenuation related to a single path diversity mode of operation for a given % of time and is given as [*Elbert, 2008; Badron et al., 2011; Nurul et al., 2013*]:

$$G(p) = A_0(p) - A_{td}(p) \tag{2.26}$$

where G(p) is the diversity gain of TD scheme, A_0 is the signal with no time delay and A_{td} is the delayed signal.

In frequency diversity scheme, two or more frequency bands are employed. During rain storms (resulting in signal attenuation), there is change-over from heavily affected frequency bands to less affected bands. Space diversity takes advantage of the finite sizes of rain cells. For SD, two or more stations are located sufficiently apart so that the effects of rain or other signal impairments do not affect both stations at the same time. This enables those stations that are less affected to route stronger signal traffic to affected stations for re-distribution [*ITU-R P.618-13, 2017*]. If two earth stations are separated by less than 20 km, ITU-R P.618-13 (2017) provides a simplified method of predicting the net diversity gain, G dB, between the two stations as:

$$G = G_d \times G_{f_{rq}} \times G_\theta \times G_\Psi \tag{2.27}$$

$$G_{f_{rq}} = e^{-0.025 f_{rq}} \tag{2.28}$$

$$G_\theta = 1 + 0.006\theta \tag{2.29}$$

$$G_\psi = 1 + 0.002\Psi \tag{2.30}$$

$$G_\mathrm{d} = a(1 - e^{-bd}) \tag{2.31a}$$

where G_{frq} is the frequency dependent gain, G_θ is the gain dependent on elevation angle, G_ψ is the baseline dependent term, d is the site separation distance in km, A is the path rain attenuation for a single site in dB, f_{rq} is the frequency in GHz, ψ is the angle of azimuth made by the propagation path and the baseline between the two sites with $\psi \leq 90°$ whereas G_d the gain contributed by spatial separation with the values of a and b given as:

$$a = 0.78A - 1.94(1 - e^{-0.11A}) \qquad (2.31b)$$

$$b = 0.59(1 - e^{-0.1A}) \qquad (2.31c)$$

D. Adaptive Coding and Modulation Scheme

Two main benefits of ACM are: (1) maximization of throughput regardless of link condition (2) keeping the link up, though with lower throughput, thereby yielding higher system availability [*Miller, 2009; Tarchi et al., 2012*]. Microwave communication links using adaptive coding and modulation (ACM) schemes continuously monitor the quality of the link. This technique enables network operators to achieve high-capacity data transmission while maintaining the highest link spectral efficiency possible at any given instance irrespective of the link condition, as shown in Figure 2.10. The high spectral efficiency is achieved by defining which services should be transmitted at various link conditions. For instance, whenever the link condition is degraded, high-priority services such as voice data are transmitted while low-priority services such as internet

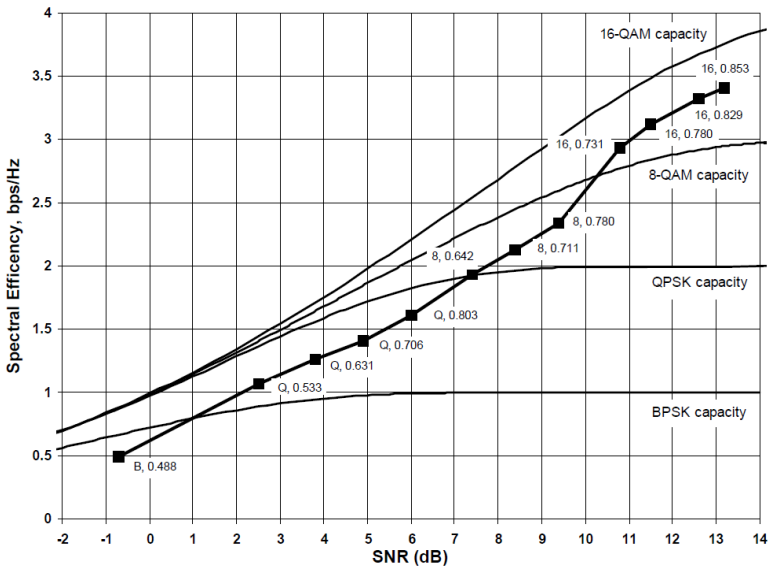

Figure 2.10 Spectral efficiency vs SNR [*Miller, 2009*]

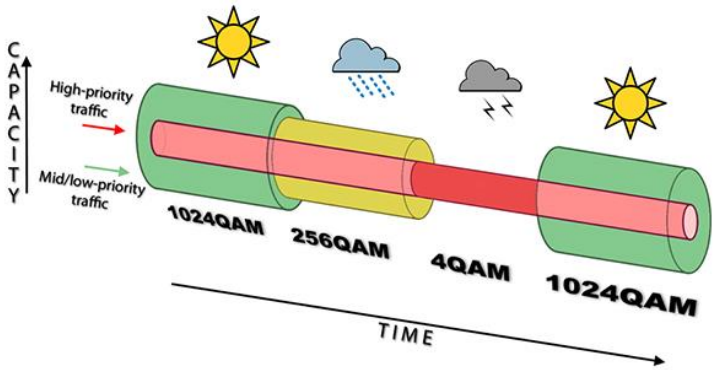

Figure 2.11 Link availability through ACM [*Bezde, 2018*]

browsing are suspended until the link condition improves [*Bezde, 2018*]. In cases of degrading signal quality, there is graceful step-down to lower-order modulation schemes during periods of intense rain storms and this maintains link reliability and availability. When signal impairments disappear, the system gradually reverts back to higher-order modulation schemes for full-capacity operation (high data rates) in clear air conditions [*Cioni, 2004; Ippolito, 2008; Das et al., 2011*].

This is illustrated in Figure 2.11 where the more robust 4QAM modulation is employed during a rain storm event to maintain the link connectivity. The average spectral efficiency, ASE, is given by [*Holm, (n.d.)*]:

$$ASE = \sum_{n=1}^{N} R_n P_n \tag{2.32}$$

where R_n is the information rate and P_n is the probability that modulation code n is used.

2.5 Chapter summary

This chapter has given a literature review on topics related to the rest of the work in this thesis. In the next chapter, effect of intense rain storms on the $R_{0.01}$ parameter and rain drop size distributions will be investigated.

CHAPTER 3

Evolution of $R_{0.01}$ parameter and effects of intense rain storms on attenuation

3.1 Introduction

In Chapter Two, a literature review on related topics are given as a foundation for the rest of the thesis. In this chapter, the long-term value of the $R_{0.01}$ parameter is investigated. This investigation is driven by the sudden rise of rain storms within the region of study. Thereafter, the raindrop size distributions are modelled using the lognormal rain DSD. Further on, an investigation is carried out to confirm the variability of the rain drop DSD with the storm magnitude.

3.2 Long-Term Rain Rate Prediction

Information pertaining to the rain rate exceeded for a fraction of an average year is very important in the design of radio links. Prediction of the rain rate exceeded for 0.01% ($R_{0.01}$ mm/h) of an average year is an important parameter for the design of radio links in order to guarantee 99.99% link availability [*Matricciani and Riva, 2005*]. In the prediction of this parameter, ITU-R recommends measurement data sampled every 1-minute. In cases where higher sampling times are used, there are models available for conversion of such data with higher sampling time, τ, to 1-minute or lower [*Flavin, 1982;Ajayi and Ofoche, 1984; Segal, 1986; Chebil and Rahman, 1999; Emiliani and Luini, 2010; Ahuna et al., 2016*a]. In regions where precipitation measurements are not available, [*ITU-R P.618-13, 2017*] provides rain maps for $R_{0.01}$ to assist in link design.

3.2.1 Methodology

This chapter, and subsequent chapters uses rainfall data collected over Durban (29°52'S, 30°58'E), South Africa, for a period of 17 years using two types of measurement instruments with three sampling times as shown in Table 3.1. As indicated in this table, the 5-min sampled data was sourced from the South African Weather Services (SAWS), whereas the rest of the data was collected at Howard College, University of KwaZulu-Natal, Durban. The outdoor measurement equipment is installed on the rooftop of the Electrical North building. The Joss-Waldvögel (JW) RD-80 impact disdrometer instrument is used for collection of precipitation using sampling times of 60 sec and 30 sec at different times. This instrument encompasses an outdoor unit with rain drops capturing surface area measuring 0.005 m^2, and an indoor unit that consists of a processor

connected to a computer. A full description and set-up of this measurement instrument is given in [*Ahuna et al., 2016*a]. The complete dataset is categorized into different year periods for investigation of the progressive nature of the $R_{0.01}$ parameter. These classifications are shown in Table 3.2.

Table 3.1 Precipitation measurements over Durban

Period	**Sampling time [min]**	**Measurement Instrument**
2001-2011	5	Rain gauge (SAWS)
2008-2010	1	Disdrometer
2013-2017	0.5	Disdrometer

Table 3.2 Categorization of precipitation measurement periods

Period	**Designation**	**Integration time [min]**
2001-2004	P_1	5
2004-2007	P_2	5
2007-2011	P_3	5
2008-2010	P_4	1
2013-2015	P_5	0.5
2014-2016	P_6	0.5
2015-2017	P_7	0.5
2013-2017	P_8	0.5

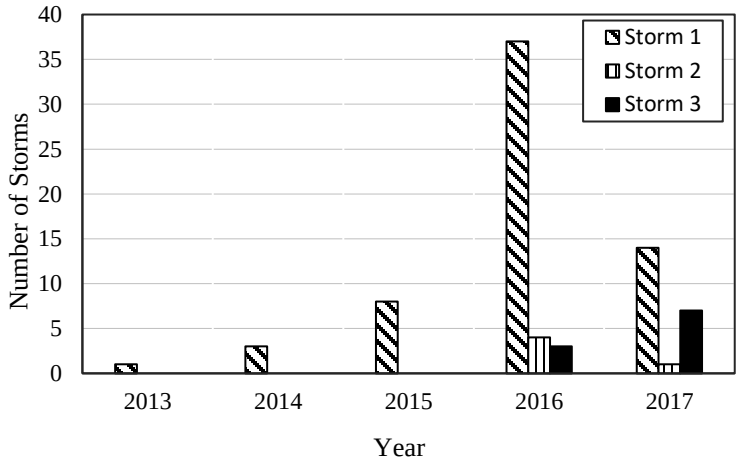

Figure 3.1 Storm occurrence patterns over Durban

Table 3.3 Number of storms recorded

Storm Type	**Number of storm occurrences**					
	2013	2014	2015	2016	2017	Total
S_1	1	3	8	37	14	63
S_2	0	0	0	4	1	5
S_3	0	0	0	3	7	10
Total	1	3	8	44	22	**78**

Table 3.4 Precipitation year periods

Year Period	**Period description**	**Abbrev.**	**Highest rain rate [mm/h]**	**Mean rain event duration [minutes]**
2013-2015	Pre-storm period	PSP	88.0419	112.40
2016-2017	Storm period	SP	253.066	69.84

Figure 3.1 and Table 3.3 show the number of rain storms that were recorded in Durban over a 5-year period. These storms are categorized according to the maximum rain rate, R_{max}, within the rain storm. Table 3.4 shows two time periods: (1) pre-storm period (PSP) that encompasses years

from 2015 and earlier and (2) a storm period (SP) that includes the years 2016 and 2017. This information can be verified in Figure 3.1 and Table 3.3, with emergence of storm 2 (S_2) and storm 3 (S_3) types in the years 2016-2017. Analysis of Table 3.3 shows that 59% of rain storms were experienced in the period 2016-2017 compared to 14% that were experienced in the 2013-2015.

3.2.2 Results and discussion

This subsection presents results that are obtained in this section. Figure 3.2(a) shows rain rates exceeded for different percentages of time of an average year. This analysis is done for year periods P_1, P_2 and P_3 and results show that the later period, P_3, has higher values of rain rates exceeded than P_1 and P_2 for all percentages below 0.02. For periods P_1 and P_2, the values seem to be close for most of the percentages, with P_1 period having slightly higher values than P_2 period. Results show that rain rates exceeded for 0.01% of time of an average year in mm/h are 54, 52 and 60 for P_1, P_2 and P_3, respectively. Rain rates exceeded for other percentages of time are recorded in Table 3.5.

In Figure 3.2(b), we present the complementary CDF for the year period P_4 and results show that the rain rate exceeded for 0.01% of an average year is 61 mm/h. This value is comparable to ITU-R value of 60 mm/h in Region L according to [*ITU-R, P.837-1, 1994*], but higher than proposed

Table 3.5 Rain rate exceeded over year period 2001-2017

%	Rain Rate exceeded [mm/h]							
	P_1	P_2	P_3	P_4	P_5	P_6	P_7	P_8
1	4	4.5	4	6	11	13	16	11
0.5	5	6	6.5	10	17	21	26	18
0.1	16	16	16	24	35	50	67	48
0.05	26	24	25.5	31	46	64.3	88.5	66
0.01	54	52	60	61	76	118	152	132
0.005	66.5	65	78.5	67	82	139	182	157
0.001	107	97.5	165	117.2	89	185	220	216

values of between 40 mm/h and 50 mm/h [*ITU-R P.837-7, 2017*]. Figure 3.3(a) shows

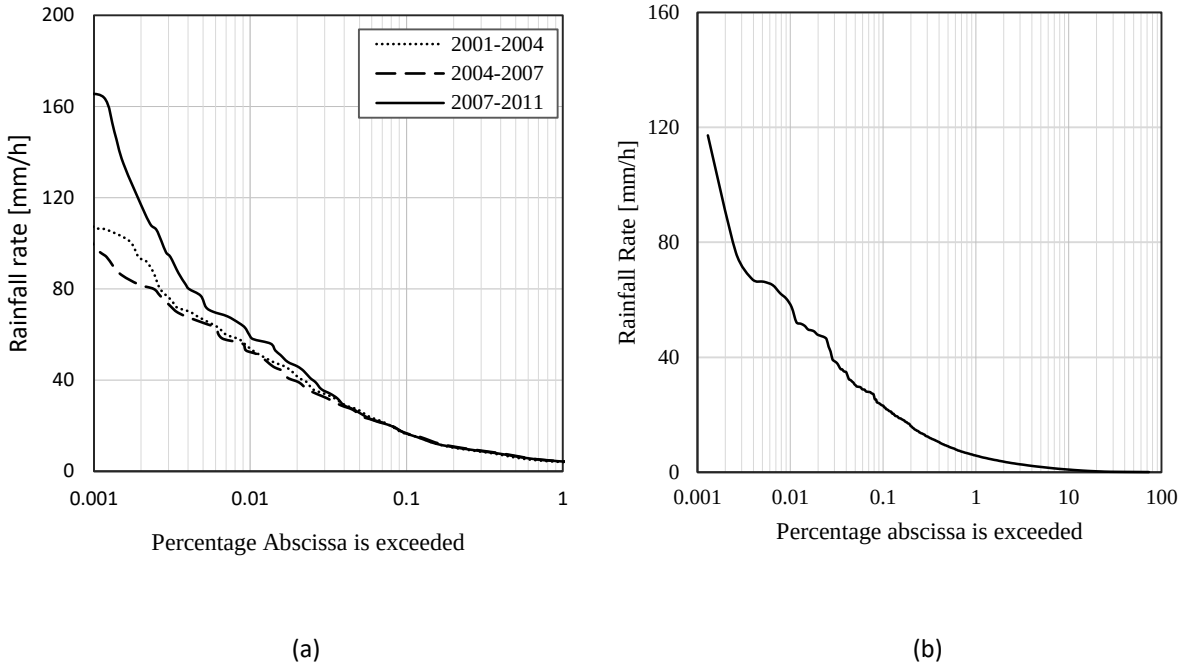

Fig. 3.2 Complementary CDFs for (a) period P_1, P_2 and P_3 (b) period P_4

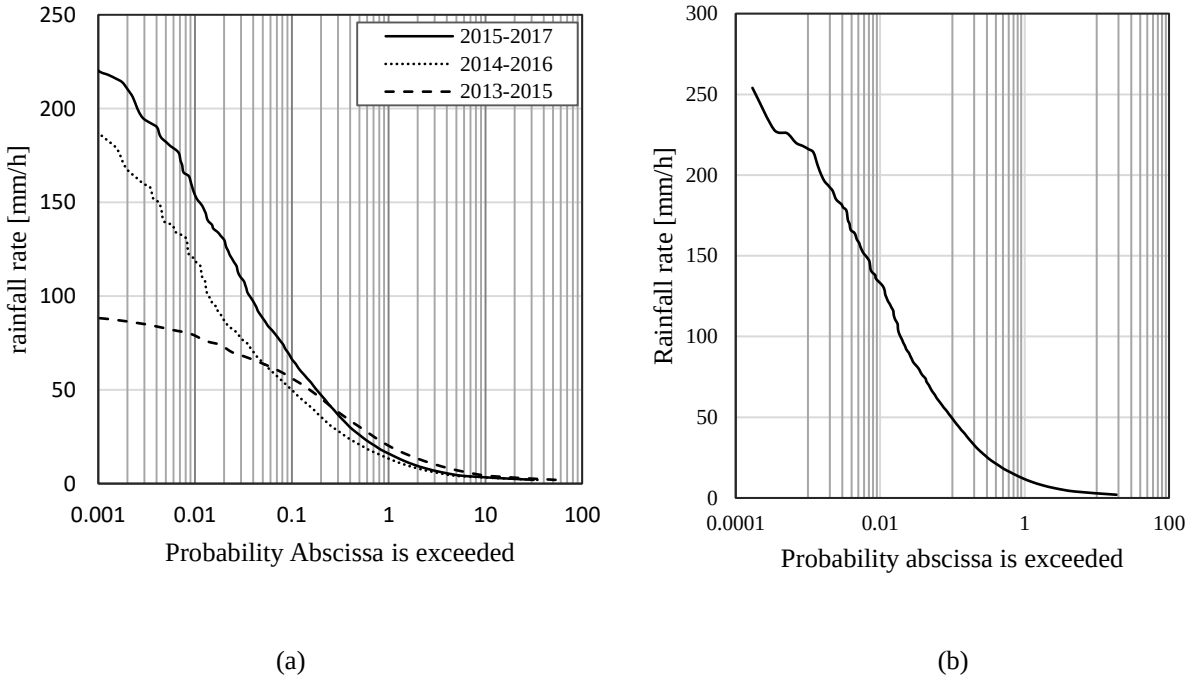

Figure 3.3 Complementary CDFs for (a) periods P_5, P_6, P_7 (b) period P_8

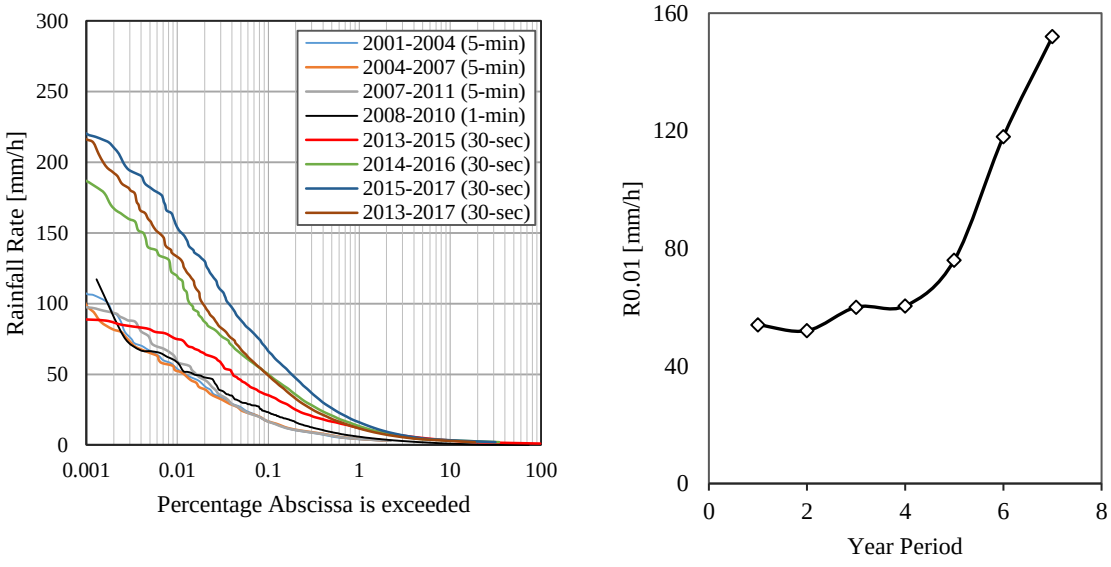

(a) (b)

Fig. 3.4 (a) Complementary CDFs for periods $P_1 - P_8$ (b) $R_{0.01}$ progression

complementary CDFs for year periods P_5, P_6 and P_7 and results show that corresponding rain rates exceeded for 0.01% of an average year are 76 mm/h, 118 mm/h and 152 mm/h for P_5, P_6 and P_7 periods, respectively. From these results, it is noted that there is an upward increase in rain rates exceeded as year periods advance and it is an indication that $R_{0.01}$ parameter is indeed rising.

Figure 3.3(b) shows the complementary CDF for the 5-year period from 2013 to 2017 (P_8) and results show that the rain rate exceeded for 0.01% of an average year is 132 mm/h. This value is way higher than that proposed by ITU-R [ITU-R P.837-7, 2017]. Figure 3.4(a) shows complementary CDFs for all year periods, P_1 - P_8. This figure shows grouping of graphs, with P_5-P_7 year-period graphs occupying the upper part of the graph, whereas the lower part being occupied by graphs of earlier year periods of P_1 - P_4. Finally, Figure 3.4(b) graphically presents the values of long-term parameter $R_{0.01}$ with time and results confirm that this parameter has been on the rise over the region of study.

3.3 Rain DSD Modelling

3.3.1 Background Information

Many authors from tropical regions are in agreement that rain DSDs that were developed using temperate data do not accurately represent tropical and subtropical rain behavior. In their studies,

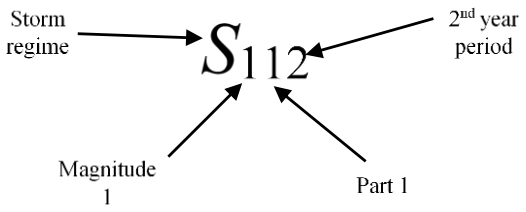

Figure 3.5 Rain storm definition

Table 3.6 Rain storm categories

Rain Storm type	**Label**	**Maximum Rainfall rate [mm/h]**	**Highest rainfall rate [mm/h]**
Storm 1 (2013-2015)	S_{101}	$40 \leq R < 100$	88.0419
Storm 1 (2016-2017)	S_{102}	$40 \leq R < 100$	99.1083
Storm 2 (2016-2017)	S_{202}	$100 \leq R < 150$	137.4889
Storm 3 (2016-2017)	S_{302}	$R > 150$	253.0660

[*Ajayi and Olsen, 1985*; *Afullo, 2011*] confirmed that the three-parameter gamma DSD model developed by [*Ulbrich, 1983*] and [*Atlas and Ulbrich, 1974*] represents rain DSDs in tropical and sub-tropical regions well. Over the current region of study, [*Odedina and Afullo, 2010*] carried out a study to determine the forward scattering amplitudes for spherical rain drops through Mie scattering approach. They used three rain DSDs (exponential, lognormal and Weibull) to model observed rain DSDs and their results showed that the lognormal DSD represented the measured rain DSDs well, followed by the gamma DSD. In 2011, [*Alonge and Afullo, 2011*] carried out an investigation on the behavior of existing rain DSD models for different rainfall regimes of drizzle, widespread, shower and thunderstorm. A year later, [*Alonge and Afullo, 2012*] investigated on the seasonal dynamics of rainfall rate and rain drop sizes in the quest to find the best fit rain DSD. Further on, parameter estimation for the lognormal rain DSD model using method of moments (MoM) and maximum likelihood estimation (MLE) were used by [*Adetan and Afullo, 2012*] and the MoM gave best fit parameters.

In this subsection, the optimized lognormal DSD with maximum likelihood estimation (MLE) of its parameters is used to fit measured rain drops size distributions. This model is represented as [*Afullo, 2011*]:

$$N(D) = f(D)N_T = \frac{N_T}{\sigma D\sqrt{2\pi}} exp\left[-\frac{1}{2}\left(\frac{\ln(D) - \mu_{ln}}{\sigma_{ln}}\right)^2\right] \tag{3.1}$$

where $f(D)$ is the probability density function, $N(D)$ is the drop size distribution, N_T is the drop concentration, whereas μ and σ are the mean and standard deviation, respectively.

3.3.2 Methodology

Data used in this section is obtained as described in *Section 3.2.1* with rain events from storm regimes ($R_{max} \geq 40$ mm/h). Rain storms were thereafter subdivided into five categories according to R_{max}, as shown in Table 3.6. Once again, the analysis is carried out for two-year periods of PSP and SP as shown in Table 3.4. It is to be noted that there are two storm subdivisions from S_1 storm type, one from each year period as shown in Table 3.6 and an illustration of storm definitions in Figure 3.5.

3.3.3 Results and Discussion

The mean parameter, μ, and standard deviation parameter, σ, in (3.1) are obtained from measured data as:

$$\mu = \frac{1}{n}\sum_{n=1}^{n} ln(D_k) \tag{3.2}$$

$$\sigma = \left[\frac{1}{n}\sum_{n=1}^{n} (ln(D_k) - \mu_{ML})^2\right]^{½} \tag{3.3}$$

The self-consistency rule of rainfall DSD was used to optimize the concentration parameter, N_T, parameter and thereafter, the three parameters in the function given in (3.1) were fitted with rainfall rates giving the following relationships

$$N_{T,xy} = a_{T,xy}(R)^{b_{T,xy}} \tag{3.4a}$$

$$\mu_{xy} = b_{\mu,xy} + a_{\mu,xy}\, ln(R) \tag{3.4b}$$

$$\sigma_{xy} = b_{\sigma,xy} + a_{\sigma,xy}\, ln(R) \tag{3.4c}$$

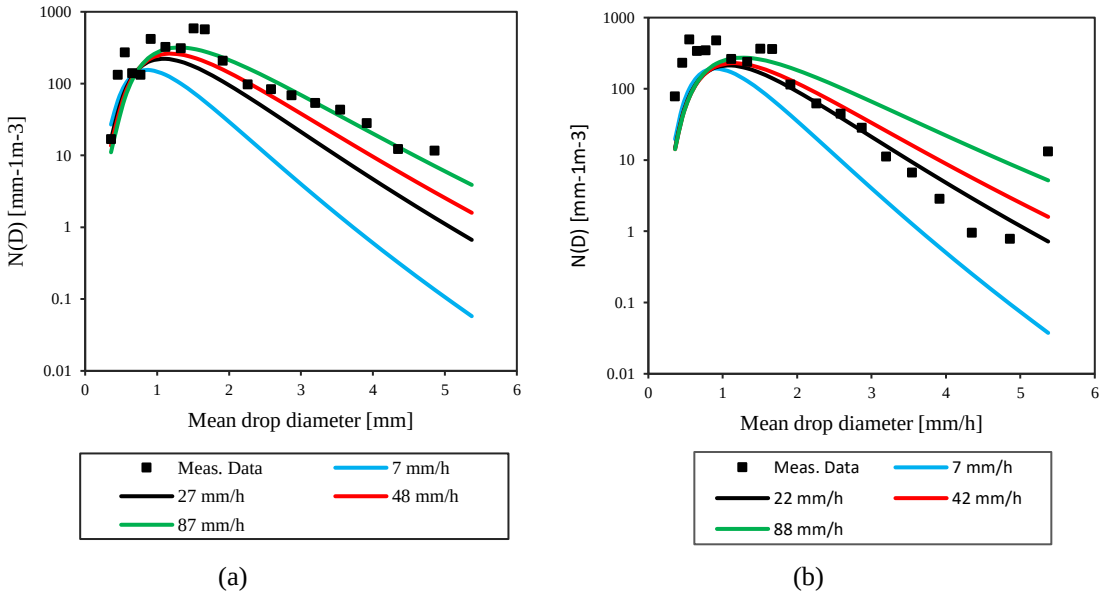

(a) (b)

Figure 3.6 Fitting observed DSDs $85\ mm/h \leq R < 90\ mm/h$ for (a) S_{101} and (b) S_{102} storms with lognormal DSD

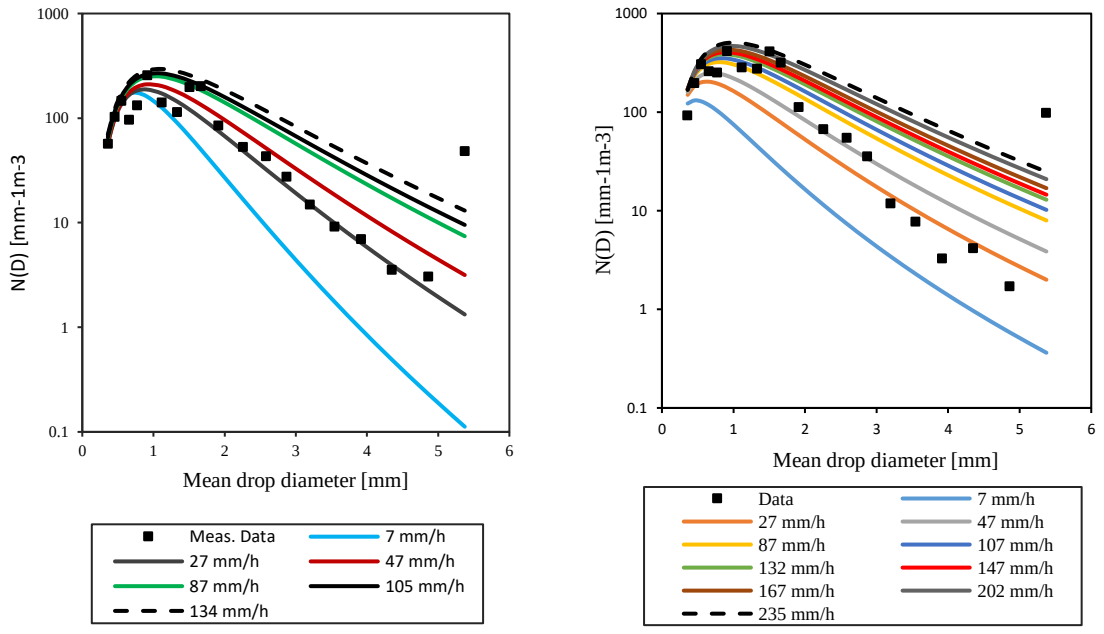

(a) (b)

Figure 3.7 Fitting observed DSDs at (a) $85\ mm/h \leq R < 90\ mm/h$ for S_{202} storm and (b) $150\ mm/h \leq R < 155\ mm/h$ for S_{302} storm with lognormal DSD

with subscript ‘x’ and ‘y’ representing the storm magnitude and the part number, respectively, as shown in Figure 3.5.

Lognormal parameters in (3.1) are shown in Table 3.7 and it is observed that there is a general decrease in the concentration parameter, N_T, from PSP to SP periods. This reduction is also evident in the μ parameter. The σ parameter is observed to increase as the magnitude of the storm increases.

In Figure 3.6, a comparison is made between the measured rain DSDs and the three-parameter lognormal function for S_1 storm type in both year periods. It is observed that there is an underestimation of the rain DSDs for drops with mean diameters less than 2 mm and rainfall rates below 85 mm/h. Also, an underestimation by the model is noted for drops with mean diameters

Table 3.7 Lognormal fitting parameters

Storm type	**Parameters**					
	$N_{T,xy} = a_T R^{b_T}$		$\mu_{xy} = a_{\mu,xy}\ln(R) + b_{\mu,xy}$		$\sigma = a_{\sigma,xy}\ln(R) + b_{\sigma,xy}$	
	$a_{T,xy}$	$b_{T,xy}$	$a_{\mu,xy}$	$b_{\mu,xy}$	$a_{\sigma,xy}$	$b_{\sigma,xy}$
S_{101}	75.947	0.5138	0.1538	-0.2383	0.0068	0.4468
S_{102}	108.87	0.3308	0.1646	-0.2419	0.0336	0.3650
S_{202}	96.516	0.356	0.1779	-0.3842	0.042	0.4388
S_{302}	46.409	0.5697	0.2006	-0.6287	-0.0001	0.7096

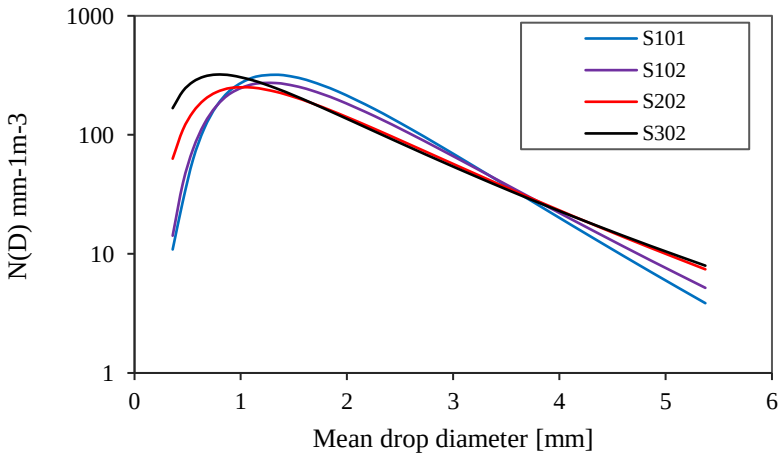

Figure 3.8 Lognormal DSD comparisons at R = 88 mm/h

above 5 mm. Figure 3.7 presents DSD fittings for S_2 and S_3 storms. From this figure, it is observed that there is a DSD overestimation is observed for rain drops with mean diameters in the range $2\ mm < D < 5\ mm$ and rainfall rates above 40 mm/h. It is noted that, though this underestimation occurs for rain drops with mean diameters above 5 mm is reflected in both year periods, the SP period suffers more.

A further investigation was carried out to examine the influence of larger storms on the drop concentration. Results of this investigation are shown in Figure 3.8, where a constant rain rate of 88 mm/h was used to generate measured DSDs within all four storm types. Results show that drops with mean diameters greater than 4 mm have higher concentration in both S_{202} and S_{302} storm types. The determination of specific attenuation through DSDs is achieved by integrating over all drop sizes using the function [*Maitra, 2004; Adetan and Afullo, 2013*]:

$$\mathrm{A}_{sp} = 4.343 \times 10^{-3} \int_0^{\infty} Q_{ext}(D_k) N(D_k).\,\mathrm{d}D_k \qquad [\mathrm{dB/km}] \qquad (3.5)$$

where A_{sp} is the specific attenuation, Q_{ext} is the extinction cross-section, p is the largest drop size and $N(D_k).dD$ is the number density of the rain drop with equivalent diameter D in the interval dD.

The measured rain DSDs at 88 mm/h were used as inputs to the function given in (3.5) for the four rain storm types. The resultant specific attenuation values are compared with those obtained using the lognormal model and the ITU-R (V) model as shown in Table 3.7. These results show that at the same rain rate, measured DSDs increase considerably with increase in the storm magnitude. The same trend is observed for the lognormal model though increments have smaller margins. At the same rain rate of 88 mm/h, the ITU-R model would give a constant attenuation of 3.6689 dB/km computed from the function, $A_{sp} = \alpha R^{\beta}$ [*ITU-R P.838-3, 2005*] using the 12 GHz frequency with vertical polarization.

3.4 Rain attenuation dependence on storm magnitudes and rain DSD

3.4.1 Introduction

Measurement campaigns on drop size distributions across the world have shown that there is an increase in the concentration of larger drop sizes per unit volume at higher rain rates. These large drops are the main cause of signal outages along microwave paths. Previous studies have confirmed that specific attenuation does not solely depend on the rain rate, but on geographic and

climatic conditions due to the high variability of the rain DSD [*Joss et el., 1970; Jaffrain and Berne, 2012; Schonhuber et al., 2015*].

The extent of attenuation on a microwave signal is dependent on sizes of rain drops present on its path. This chapter investigates the effects and contributions of heavy rain storms on the maximum size of the rain drop. Electromagnetic signals (with frequencies above 10 GHz) transmitted over wireless links suffer greatly from the effects of rain. These waves are greatly attenuated through processes of absorption and scattering during heavy rain storms [*Lakshmi et al., 2007; Schonhuber et al., 2013; Ahuna et al., 2016*a]. *Lakshmi et al.* [*Lakshmi et al., 2007*], in their investigations, noted that drop diameters from 0.771 mm to 5.3 mm play a significant role in the determination of specific attenuation. In their investigations over Durban, *Adetan and Afullo* (2013) concluded that rain drops in the range 0.5 mm $\leq D \leq$ 2.5 mm contribute higher specific attenuation at higher frequencies. In this section, analysis of the variability of rain attenuation that results from rain drops present in different magnitudes of rain storms is performed. This investigation is motivated by the sudden occurrence of rain intense rain storms over the region as shown in Figure 3.1 and Table 3.3.

3.4.2 Data Collection and Processing

The data set in this section is drawn from data collection described in *Section 3.2.1* with data from collected from 2013 to 2017. This data is, thereafter, categorized into different storm magnitudes as shown in Table 3.6.

3.4.3 Results and Discussion

Results are discussed in two parts: (1) relationship between the maximum drop size, D_{max}, and the rain rates, and, (2) the relationship between the total number of drops, N_{tot}, and rain rates within a storm.

A. Correlation of D_{max} with rainfall rate

The largest mean drop diameter for each rain rate were correlated with rain rates and resultant correlations are shown in Figure 3.9 and Table 3.8. These results show that the largest drop diameter, D_{max}, increases with increase in the rain rate, R. For instance, it is observed that an average value of D_{max} is 4.859 mm, 5.202 mm, 5.373 mm and 5.373 mm for S_{101}, S_{102}, S_{202} and S_{302} storms respectively at higher rainfall rates. This relationship between D_{max} and rain rate is observed to follow a power-law function given as:

$$D_{max} = k_D R^{\alpha_D} \tag{3.6}$$

where k_D and α_D are regression factors whose values are shown in Table 3.8. It is observed that the maximum mean drop diameter for S_{302} storm was nearly constant from a rain rate of about 18 mm/h and can be estimated by:

$$D_{max,S_{302}} = \begin{cases} 3.3704R^{0.173}, & R < 18\ mm/h \\ 5.373\ , & R > 18\ mm/h \end{cases} \tag{3.7}$$

B. Correlation of N_{tot} rain drops with rainfall rate

Furthermore, an investigation was carried out on the relationship between the total number of rain drops with rainfall rate, *R*, in mm/h for different rain storms. Figure 3.10 shows a power law relationship for all the four storm types with correlation factors above 0.8. This relationship is shown as:

$$N_{tot} = k_N R^{\alpha_N} \tag{3.8}$$

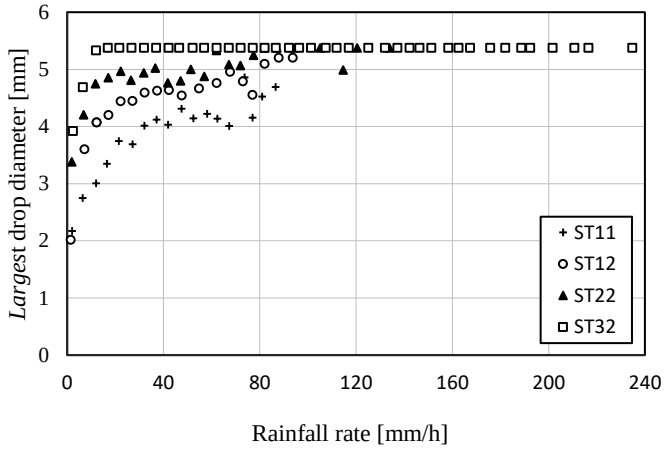

Figure 3.9. Correlation of D_{max} with rainfall rate

Table 3.8 Correlation of D_{max} with rain rates

Storm Type	k_D	α_D	R^2
S_{101}	1.901	0.1989	0.9463
S_{102}	2.3153	0.1832	0.8525
S_{202}	3.518	0.0907	0.8230

where N_{tot} is the total number of drops per rain rate sample, and k_N and α_N are regression factors whose values are given in Table 3.9. Analysis of results in this this table shows that the total number of drops decreases with increase in the magnitude of the storm.

C. Specific Rain Attenuation

For slant paths, [*ITU-R P.618-13, 2017*] recommends a model for calculating the attenuation exceeded for 0.01% of time of an average year. This model is given in (2.9) with specific attenuation as one the inputs. Two common ways of estimating the specific attenuation are: (1) using the rain rate, *R* mm/h in the power-law function or (2) using observed rain DSD. The first approach is given as [*ITU-R P.838-3, 2005*]:

$$\gamma = kR^{\alpha} \qquad [dB/km] \tag{3.9}$$

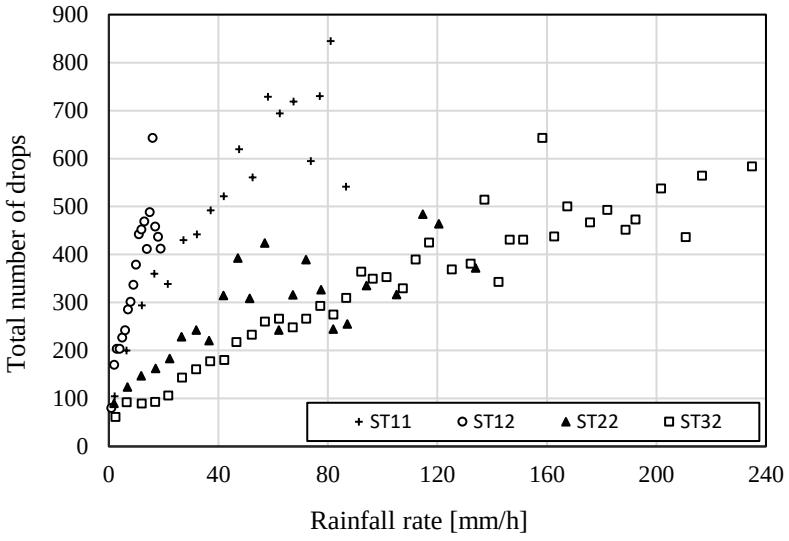

Figure 3.10 Correlation of N_{tot} with rainfall rate

Table 3.9 Correlation of N_{tot} with rain rates

Storm Type	k_N	α_N	R^2
S_{101}	76.945	0.5138	0.9487
S_{102}	65.811	0.4544	0.9436
S_{202}	63.858	0.3787	0.8085
S_{302}	25.314	0.5633	0.9395

where γ is the specific attenuation whereas k and α are regression factors given in [*ITU-R, P.838-3, 2005*]. The expression for estimation of specific attenuation, A_{sp}, using observed rain drop size distribution is given as [*Adetan & Afullo, 2013*]:

$$\mathrm{A}_{sp} = 4.343 \times 10^{-3} \sum_{\mathrm{k}=1}^{\mathrm{n}} \mathrm{Q}_{\mathrm{ext}}(D_k)\mathrm{N}(\mathrm{D}_{\mathrm{k}}).\,\mathrm{dD}_{\mathrm{k}} \qquad [\mathrm{dB/km}] \qquad (3.10)$$

where Q_{ext} is the extinction cross-section, n is the largest size and $N(D_k).dD$ is the number density of rain drops with equivalent diameter D in the interval dD.

Figure 3.11 shows the graph of specific attenuation determined using measured rain DSD model given in (3.10). For instance, it is observed that specific attenuation values of 4.2122, 4.6796, 5.7625 and 5.9799 are obtained for storms S_{101}, S_{102}, S_{202} and S_{302}, respectively. These values are obtained for a mean rain rate in the range $85 \leq R < 90$ mm/h. It is observed that, despite a decrease in the total number of drops for larger rain storms, there is an increase in signal attenuation. This increase in attenuation is explained by earlier appearance of larger rain drop diameters during high magnitude storms as demonstrated in Figure 3.9. In contrast, using the specific attenuation model in (3.9) in the same rain rate range gives a constant value of 3.6689 dB/km as is observed in Section 3.3.3.

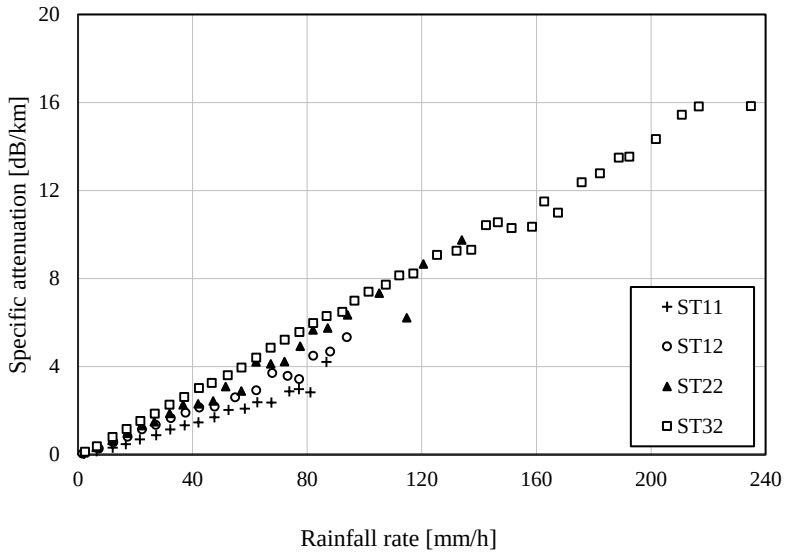

Figure 3.11 Correlation of specific attenuation with rain rate

3.5 Chapter Summary

Results in this chapter show that the parameter $R_{0.01}$ over Durban has escalated to higher values compared to ITU-R proposed value. Further, analysis of the rain drop size distribution show that with the occurrence of larger storms, measured rain DSDs above 5 mm drop diameter fail to match with the statistical lognormal rain DSD model. Lastly, the specific attenuation is obtained from measured rain DSD and results show that at the same rainfall rate, a wireless link is exposed to different outage levels depending on different storm magnitudes. In the next chapter, we explore the prediction of rain attenuation using the backpropagation neural network for dynamic rain fade mitigation.

CHAPTER 4

Prediction of rain attenuation using the Backpropagation Neural Network

4.1 Introduction

The use of higher frequencies above 10 GHz for satellite and terrestrial microwave communication results in signal fading during intense rainfalls [*Matricciani, 1981; Ajayi and Ofoche, 1984; Emiliani et al., 2009*]. These outages are a great concern to service providers especially during live streaming of content such as sport events and prime news that require virtually zero link outages. In the previous chapter, we investigated the effects of intense rain storms on the long-term $R_{0.01}$ long-term parameter and the resulting rain attenuation through measured rainfall DSDs. Dynamic rain fade mitigation requires link state monitoring in real time. This provides information on the state of the link at a future time (t +1). In this chapter, the backpropagation neural network (BPNN) is trained to predict and classify rain attenuation for dynamic rain attenuation mitigation schemes such as adaptive coding and modulation. Consequently, this prediction allows measures to ensure acceptable signal-to-noise (S/N) ratio to maintain the quality of service, and therefore, enhance resource management.

4.2 Background Information

Several rain attenuation prediction models (*see* Table 4.3) have been developed, such as the ITU-R model [*ITU-R P.618-13, 2017*] and Synthetic Storm Technique (SST) model [*Matricciani, 1996; Matricciani and Carlo Riva, 2005*]. Moreover, the ITU-R model statically predicts rain attenuation and hence is not appropriate for dynamic fade mitigation. A review by *Nayak et al.,* (2013) on the utilization of the artificial neural network (ANN) for rainfall prediction reports on the suitability of the ANN for rain fall prediction compared to mathematical and statistical methods. A number of research work on the use the ANN for rainfall prediction has been done in the field of meteorology and water management for monthly rainfall forecasting [*Luk et al., 2001*; *Abhishek et al., 2012; Christodoulou and Michaelides, 2007; Purnomo et al., 2017*]; with a few studies leaning towards prediction intervals of 24 hours or less [*French et al., 1992; Michaelides et al., 1995*; *Christodoulou et al., 2004; Ahuna et al., 2017*]. In this chapter, we focus on the latter approach to rainfall prediction, as it would be more relevant to this work.

4.3 The BPNN Computing Unit

The backpropagation neural network (BPNN) as a computing unit, is divided into two functional units: an integration function unit and the output function. The former function sums up *N* inputs into a single value, whereas the latter unit uses an activation function to produce an output in accordance with the computation function. The common activation function commonly used with backpropagation neural networks is the sigmoid function. This function possesses two key properties of continuity and differentiability of the error function during training. The basic diagram of the ANN as a computing unit and the training structure is shown in Figure 4.1. Integration and activation functions shown in Figure 4.1 are given as [*Rojas, 1996; Ahuna et al., 2017*]

$$g = b + \sum_{n=1}^{N} w_n i_n \qquad n = 1,2, \dots, N \tag{4.1}$$

where, *b* is the bias input, g is the integration function, *N* is the number of inputs, and w_n is the weight associated with the *n*th input, i_n. The actual output of the backpropagation neural network is obtained by applying the activation function to the integration function given by [*Rojas, 1996; Rumelhart et al., 1986*]:

$$f(g) = \frac{1}{1 + e^{-g}} \tag{4.2}$$

where *f*(*g*) is the activation function. During the training process, the network's performance is evaluated by computing an error function given by [*Rumelhart et al., 1986; Rojas, 1996*]:

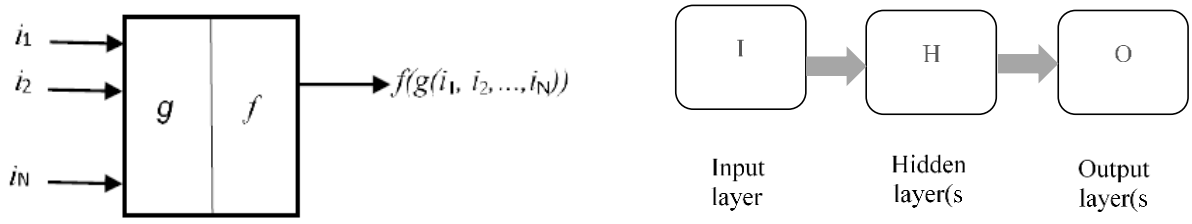

(a) (b)

Figure 4.1 The (a) ANN Computing unit (b) BPNN training structure

$$E = \frac{1}{2}\sum_{p=1}^{P}(O_t - O_{BP})^2 \tag{4.3}$$

where E is the error, O_t is the desired output (target), O_{BP} is the BPNN output, and P is the number of data points. A good predictor model produces outputs that are exact or as close as possible to expected outputs. For the BPNN, errors between outputs and targets during the training process are minimized by an error derivative given by [*Rojas, 1996; Ahuna et al., 2017*]:

$$\frac{\boldsymbol{\partial E_{total}}}{\boldsymbol{\partial O_a}} = -(\boldsymbol{O_t} - \boldsymbol{O_a}) \tag{4.4}$$

The process in (4.4) aims at arriving at an optimized weight vector, w, which results in a minimized error function. This is achieved by updating associated weights on the *i*th input using:

$$\Delta w_i = \eta \frac{\partial E}{\partial O_i} \qquad i = \quad 1,2,\dots,I \tag{4.5}$$

where η is the learning rate, Δw_i is the weight change on the *i*th input, and O_i and the output contributed by the *i*th input.

4.4 Methodology

Training and validation data for the proposed model was collected as described in *Section 3.2.1* with a sampling time of 30 seconds. Training dataset, comprising of 108, 861 samples was obtained from the 4-year (2013-2016) measurement period, and comprise of the four rainfall regimes of drizzle, widespread, shower and storms. It is important to train the neural network using rainfall events from all regimes to prepare the predictor model for all types of rainfall regimes. To validate and test the trained model, we used data collected from January 2017 to May 2018. Rainfall data within this period of 17 months are a representation of all four seasons (summer, autumn, winter and spring) that are experienced in the region of study.

4.4.1 BPNN Training

The training model is a three-layered network whose structure is 3:3:1:1 as shown in Figure 4.1(b). In this structure, there are 3 inputs (I), 3 neurons in the hidden layer (H) and one neural in the output layer (O). The last '1' stands for the network output. During training, TRAINLM and

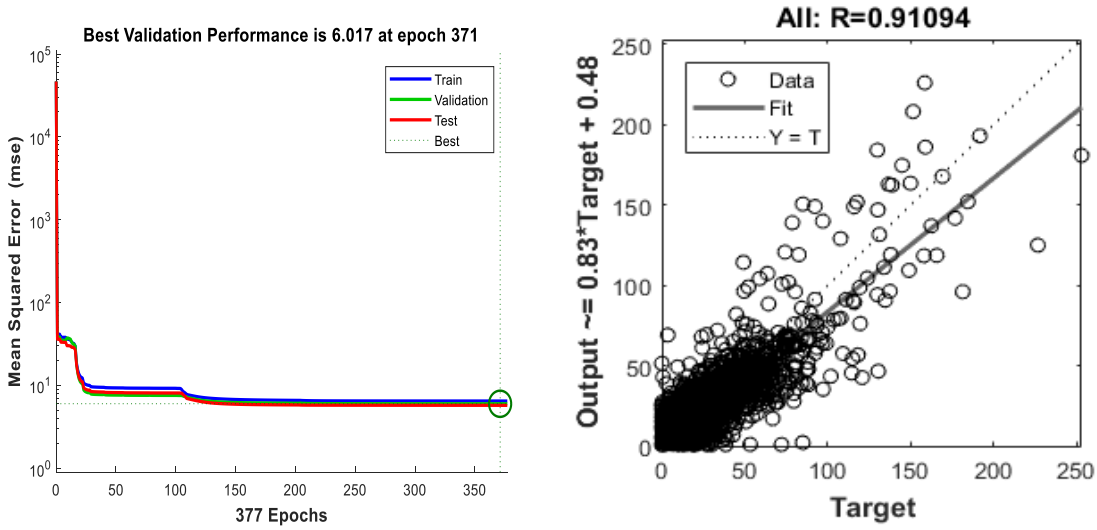

(a) (b)

Figure 4.2 BPNN training plots (a) performance (b) regression

LEARNGDM functions were used as training and adaptation functions, respectively, whereas the MSE and TANSIG were utilized as performance and transfer functions, respectively. The best performance was achieved at epoch 371 of 377 epochs with a mean square error of 6.017. Performance and training regression plots are shown in Figure 4.2(a) and Figure 4.2(b) respectively. The regression coefficient of 0.91094 shown in Figure 4.2(b) shows a good correlation between BPNN outputs and target outputs. After training, optimized weight and bias matrices are determined to be:

$$w_{\mathrm{HI}} = \begin{bmatrix} -0.1974 & -1.1467 & -7.8568 \\ -0.0115 & 0.0086 & -0.0476 \\ 4.0797 & 6.1838 & 6.0543 \end{bmatrix} \quad (4.6a)$$

$$w_{\mathrm{OH}} = [-78.4395 \quad -32.0736 \quad 31.939] \quad (4.6b)$$

$$b_{\mathrm{H}} = \begin{bmatrix} -11.4485 \\ 0.4845 \\ -17.3805 \end{bmatrix} \quad (4.6c)$$

$$b_{\mathrm{O}} = [-32.1027] \quad (4.6d)$$

where $\boldsymbol{w}_{HI}$ is the weight vector for weights from the input to the hidden layer, $\boldsymbol{w}_{OH}$ is the weight vector for weights from the hidden layer to the output layer whereas $\boldsymbol{b}_H$ and b_O are input bias vectors to the hidden layer and the bias input to the output layer, respectively.

4.4.2 The BPNN Prediction Model

Most well-known rain rate prediction models such as [*Moupfouma, 1985; ITU-R P.837-6, 2012*] estimate rain rates exceeded for various percentages of time in an average year. Due to the highly variable nature of rainfall with respect to both space and time, communication links suffer great outages during intense rain storms that may last for relatively short periods hence the need for prediction of rain attenuation in time domain. Thus, the main goal is to train a backpropagation neural network for prediction of a future rainfall rate, $R_p(t + 1)$ mm/h at time $(t + 1)$, using two previous rain rates and a current rain rate, $R_a(t)$ as shown in Figure 4.3. The predicted rain rate is related to the three previous rain rates by the function [*Ahuna et al., 2017*]:

$$\boldsymbol{R_p(t+1) = f\left(R_a(t-2), R_a(t-1), R_a(t)\right)} \qquad (\mathbf{4.7})$$

where $R_a(t – 1)$ and $R_a(t – 2)$ are actual rain rates at time $(t – 1)$ and $(t – 2)$, respectively and all rain rates are measured in mm/h. Rain attenuation prediction models such as those proposed by *Bryant et al.* (2001)*; Capsoni et al.* (2009)*; Crane* (1982)*; ITU-R P.618-13* (2017) estimate rain attenuation exceeded for different percentages of an average year. In 1996, *Matricciani,* (1996) proposed a prediction model for rain attenuation time series. In this model, the vertical structure of rain is modelled as two layers with one layer consisting of hydrometeors in the form of rain drops (Layer A) and the other layer comprising of melting hydrometeors (Layer B). In this study,

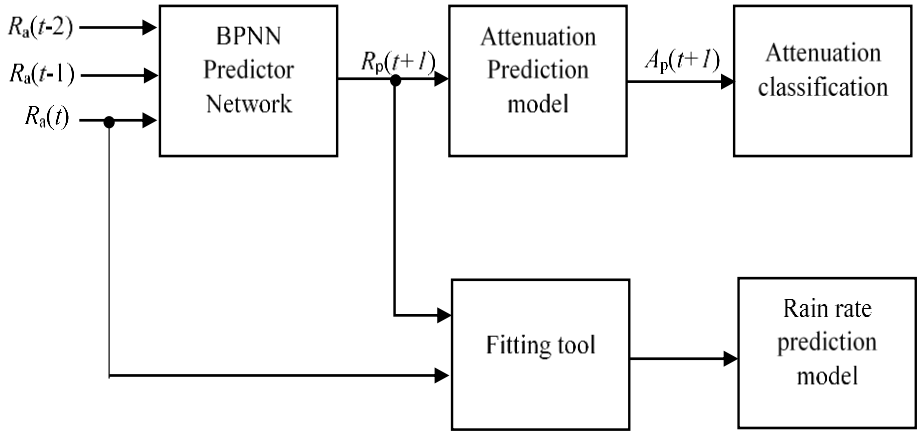

Figure 4.3 Attenuation prediction and classification model

rain attenuation prediction is achieved using the model proposed by *Matricciani* (1996) in conjunction with parameters obtained in *ITU-R P.618-13*, (2017) and *ITU-R P838-3*, (2005). The rain attenuation time series proposed by *Matricciani* (1996) estimates rain attenuation *A* at time (*t*) as:

$$A(t) = k_A R(t)^{\alpha_A} L_A + r^{\alpha_B} k_B R(t)^{\alpha_B} (L_B - L_A) \qquad [dB] \tag{4.8}$$

where L_A and L_B are Layer A and Layer B slant paths, respectively, in km, *R(t)* is the rain rate in Layer A, *r* is the rain rate in Layer B whose value is given in [*Matricciani, 1996*], whereas k_A, α_A, k_B, and α_B are frequency-dependent parameters for Layer A and Layer B given in [*ITU-R P838-3, 2005*].

4.5 Results and Discussion

In this section, discussions are done in two parts: (1) complementary CDFs and (2) the BPNN rain rate prediction model. In the former, long-term attenuation from the prediction model is compared with actual and ITU-R model values.

4.5.1 BPNN Rain Rate Prediction Model

The trained BPNN was tested using precipitation data collected from January 2017 and May 2018. This data is 'unseen' to the trained network because it was not used in training. The BPNN testing results show a fair correlation coefficient of 0.8298 between actual and predicted rainfall data and root mean square error (RMSE) of 2.5128. This correlation is shown in Figure 4.4(a). Further, fitting of predicted and current rain rates was done and resulted in a correlation coefficient of 0.9811. Out of this correlation, a model is developed that relates $R_p(t + 1)$ and $R_a(t)$ as:

$$R_p(t + 1) = mR_a(t) + n \tag{4.9}$$

where *m* and *n* are regression parameters whose values are 0.9036 and *n* = 0.3483, respectively and $R_p(t + 1)$ being a function of the previous three rain rates as shown in (4.7).

4.5.2 Long-Term Rain Attenuation Prediction

The motivation in this subsection is to make a comparison of complementary CDFs resulting from actual and predicted rainfall attenuation values. From (4.7) and (4.8), attenuation on the link at time ($t + 1$) can be obtained as:

$$A_p(t + 1) = \Phi L_A + \Psi(L_B - L_A) \tag{4.10a}$$

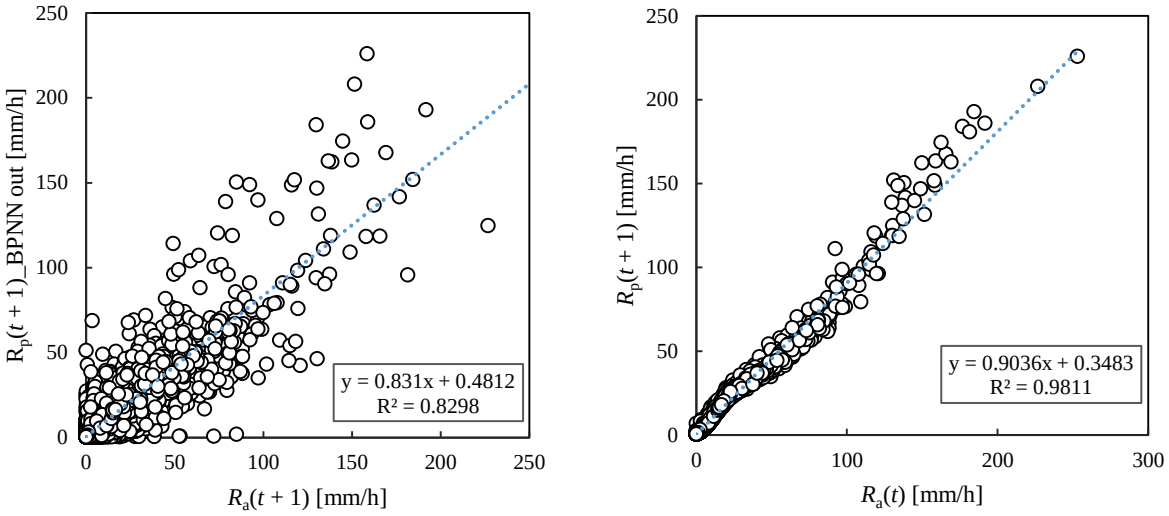

(a) (b)

Figure 4.4 Correlation of BPNN predicted outputs with (a) actual outputs at time (t + 1) (b) current rain rates at time (t)

with:

$$\Phi = k_A R_p(t+1)^{\alpha_A} \tag{4.10b}$$

$$\Psi = r^{\alpha_B} k_B R_p(t+1)^{\alpha_B} \tag{4.10c}$$

Using the testing data described in *Section 4.5.1*, Figure 4.5 shows testing result statistics for the long-term attenuation statistics exceeded for various percentages of an average year.

Comprehensive statistics are shown in Table 4.1 for the comparison of long-term statistics for actual values, BPNN predicted outputs and outputs from the model in (4.9). The ITU-R P.618 model results are also presented for comparison. Results of this long-term prediction show that attenuation values exceeded for 0.01% of an average year are 53 dB (from actual rain rates), 50 dB (from BPNN predicted outputs), 48 dB (proposed model in (4.9) and 53 dB (ITU-R model). These results show the BPNN's ability to predict rain rate time series and consequently, rain attenuation.

4.6 Model Validation

Rainfall events with varying magnitudes from different rainfall regimes were used to confirm the suitability of the proposed prediction model. Five attenuation classes with four attenuation

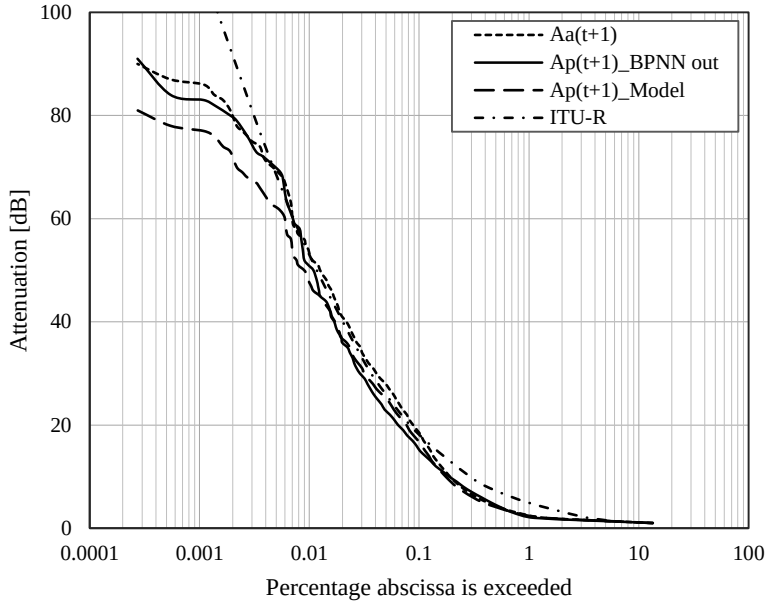

Figure 4.5 Complementary CDFs for long-term rain attenuation (2017-2018)

TABLE 4.1 Rain attenuation distributions

%	Rain attenuation exceeded [dB]			
	A_a(t+1)	A_p(t+1) BPNN out	A_p(t+1) model	A_p(t+1) *ITU-R*
1	2	2	2	5
0.1	18	15	16	18
0.01	53	50	48	53
0.001	86	83	77	106

thresholds of 10 dB, 20 dB, 40 dB and 60 dB were used for this purpose and are shown in Table 4.2. The prediction model illustrated in Figure 4.3 was provided with rain rates from individual rain events and the model produced, as outputs, predicted rain rates for conversion to corresponding attenuation values using the prediction model. Thereafter, these attenuation values are classified using a classification algorithm. As an example, Figure 4.6(a) and Figure 4.7(a) show rain rates of a shower rain event with R_{max} = 22.2265 mm/h being used as inputs to both the BPNN model and the model given in (4.9), respectively. Classifications of resultant attenuation values are shown in Figure 4.6(b) and Figure 4.7(b). These results show that all predicted attenuation

Table 4.2 Rain attenuation classes

Attenuation Class	Class Bounds [dB]
1	$A < 10\ dB$
2	$10 \leq A < 20$
3	$20 \leq A < 40$
4	$40 \leq A < 60$
5	$A \geq 60$

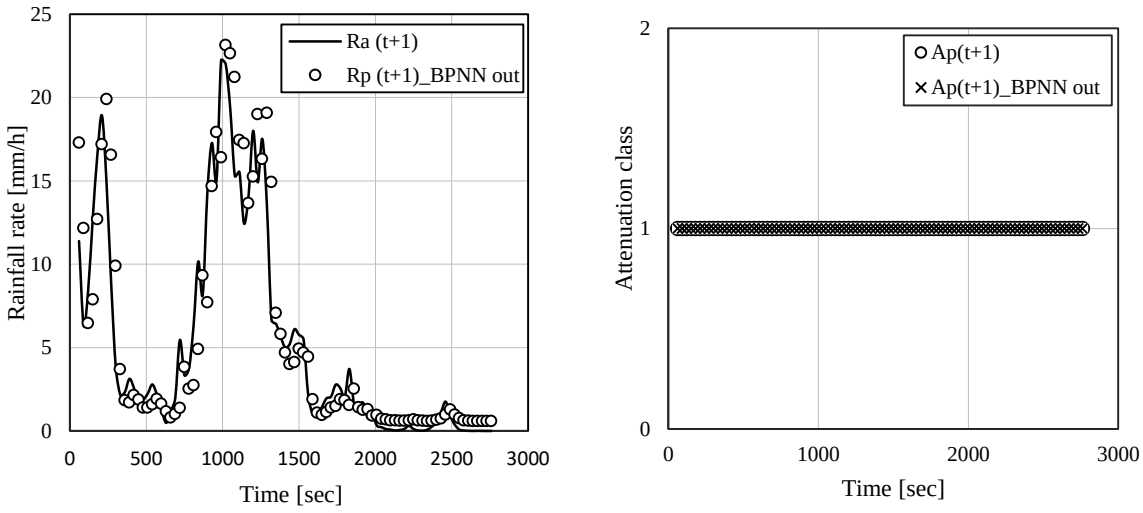

(a) (b)

Figure 4.6 (a) Prediction of (a) rain rate (BPNN out) at R_{max} = 22.2265 mm/h) (b) rain attenuation classification

values are within Class 1 with of attenuation class bound A < 10 dB. In this work, a good class agreement occurs when 'o' and 'x' markers merge as shown in Figure 4.6(b) and Figure 4.7(b).

The prediction model was further tested on a S_{120} rain event of 21st Feb. 2018, with a maximum rain rate of 89.9575 mm/h as shown in Figure 4.8(a). Three rain attenuation classes are expected from this rain event as shown in Figure 4.8(b). A more detailed section of Figure 4.8(b) reveals a few misses in the predicted rain attenuation.

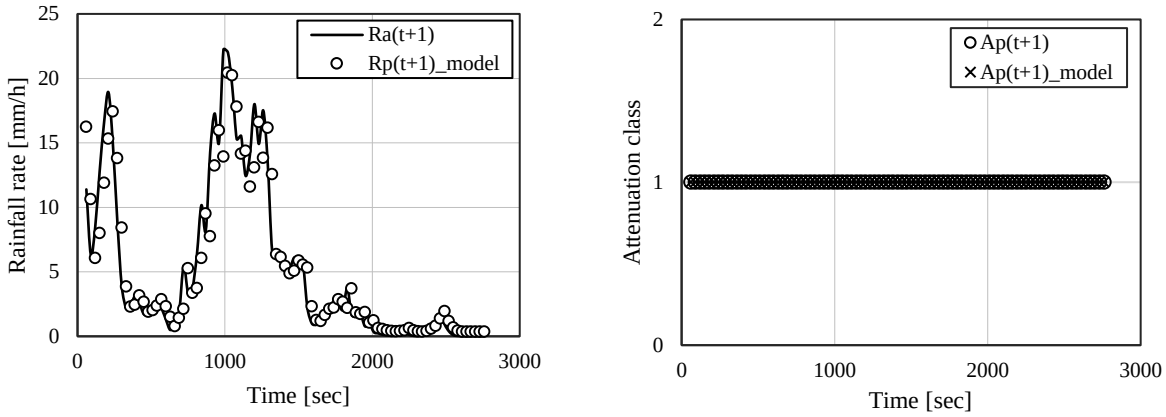

(a) (b)

Figure 4.7 Prediction of (a) Rain rate (model at R_{max} = 22.2265 mm/h (b) rain attenuation classification for Figure 4.7(a)

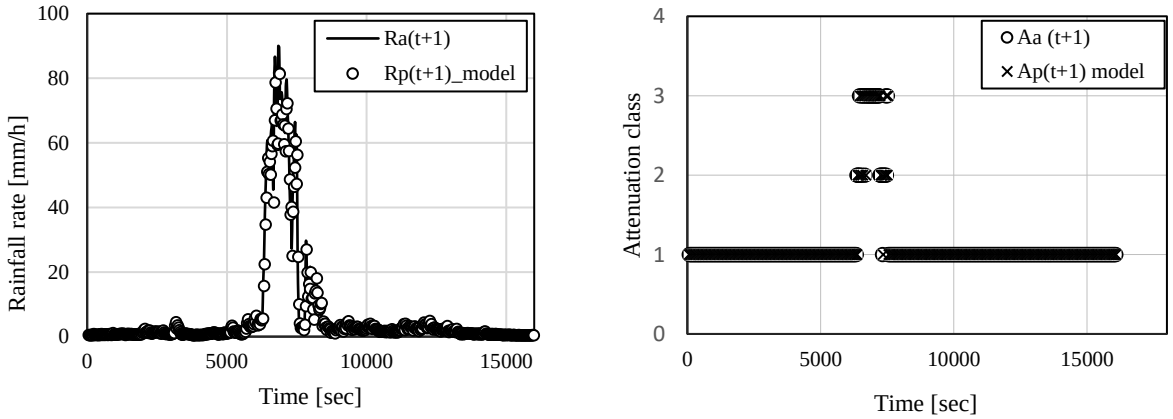

(a) (b)

Figure 4.8 Prediction of (a) Rain rate (model) at R_{max} = 89.9575 mm/h (b) rain attenuation classification for Figure 4.8(a)

The highest rain rate within the testing dataset was 224.9989 mm/h that occurred on 22nd February 2017 at 10:53:00 hours. Testing on this rain event was inspired by the need to show the viability of the prediction process during intense rain storms. Model prediction of these rain rates are shown in Figure 4.10(a) and the resulting attenuation classification is presented in Figure 4.10(b). Observations show that the model can predict fairly well the rain attenuation, and classification results fall within all five classes, as expected. A detailed view of a section of Figure 4.10(b) is presented in Figure 4.11 that spans across a time length of 600 sec (from t = 1000 sec to t = 1600

sec), a period that is expected to experience the deepest fading effect. Results of this test show that there are nine misses during this period. Nevertheless, cases where the 'x' marker is above the 'o' marker can be regarded as safer because during these instances, there is an over-estimation of rain attenuation and this causes a fade mitigation scheme to be put in place. Close analysis shows that rain attenuation underestimation or overestimation in most cases, involve two adjacent levels, implying that the fade mitigation technique employed might be adequate for the two cases and especially when these attenuation values are close to threshold boundaries.

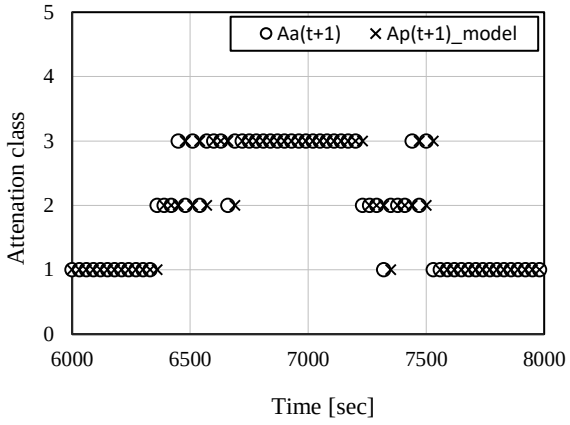

Figure 4.9 Expanded section of Figure 4.8(b)

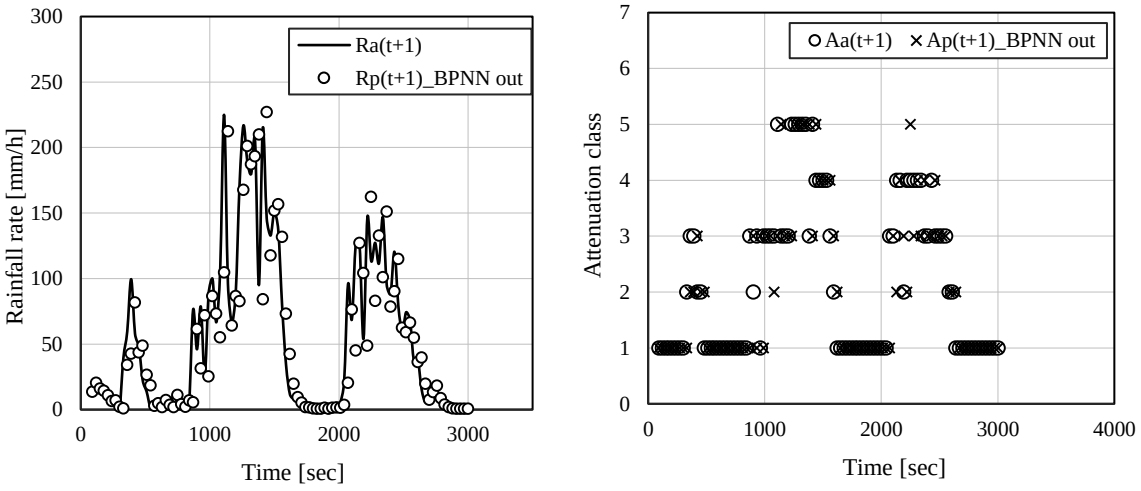

(a) (b)

Figure 4.10 Prediction of (a) Rain rate (model) at R_{max} = 224.9989 mm/h (b) rain attenuation classification for Figure 4.10(a)

The prediction model was further subjected to one-minute sampled data from Butare, Rwanda, tropical region with equatorial climate. The event is a storm type with R_{max} = 66.0395 mm/h that occurred on 17th Feb. 2015 from 10:31:00 hours. Results of this rain rate prediction are shown in Figure 4.12(a) whereas attenuation classification is shown in Figure 4.12(b). The classification plot shows that there were three misses within a period of 600 sec (10 minutes). Excluding overestimation, this number reduces to only one miss, a case of underestimation at time t = 9750 sec. A comparison of various attenuation models are shown in Table 4.3 as proposed by various researchers from different parts of the world.

Table 4.3 Comparison of rain attenuation models

Model	**Inputs**	**Deployment**
Rice-Holmberg	Cumulative distribution of rainfall	Temperate climate
Global model	Location and link parameters	Globally
Karasawa Model	Rain statistics and link parameters	Applicable for Japanese environment
ITU-R P.618-11	Location and link parameters	Used or region-wise rain intensity
Crane model	Rain cell and debris together with other link parameters	Used for different hydrometeors
Matricciani model	Point rain rate and link parameters	Attenuation time series
Dutton-Dougherty	Exceedance time % used with rain rate	Used for gaseous and rain attenuation
Garcia Lopez	Point rain rate and link parameters	Used for tropical climate
Simple Attenuation Model (SAM)	Point rain rate and link parameters	Optimized for simplicity

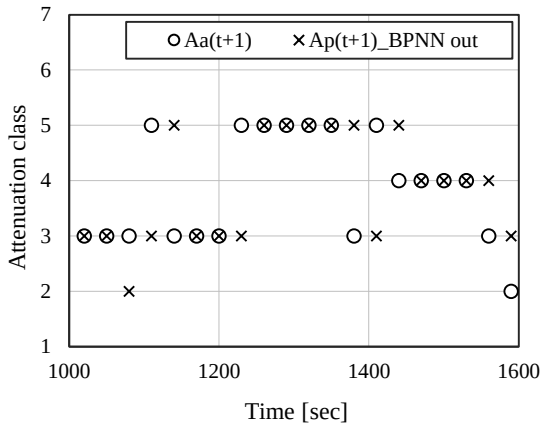

Figure 4.11 Detailed section of Figure 4.10(b)

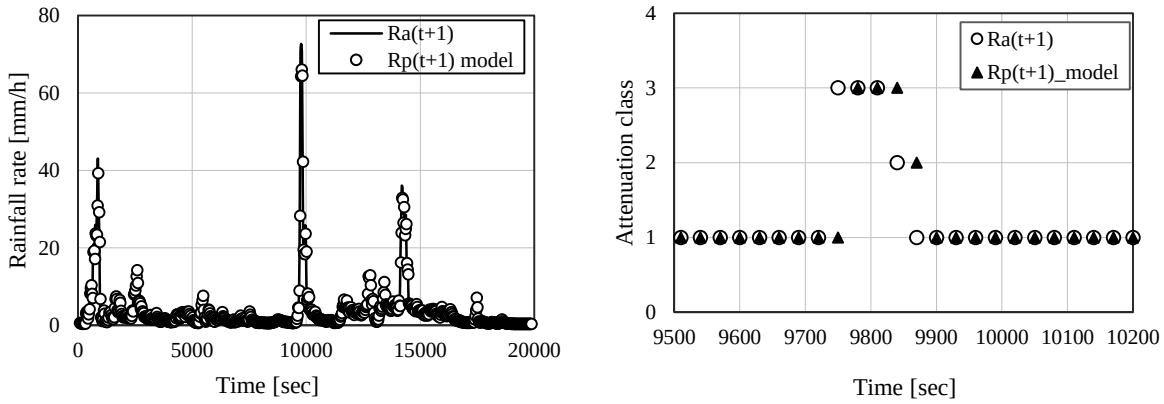

(a) (b)

Figure 4.12 Prediction of (a) Rain rate (model) at R_{max} = 60.0395 mm/h in Butare (b) rain attenuation classification for Figure 4.12(a)

4.7 Chapter Summary

Results obtained in this chapter have indicated that a trained backpropagation neural network can be used to predict rain attenuation fairly well over a communication link. In addition, the portability of the prediction model has been demonstrated through data collected over an equatorial region with a tropical climate. In the next chapter, we will investigate the queueing characteristics of rain spikes and their probabilities of occurrence using the queuing theory technique and Markov Chain.

CHAPTER 5

Outage Prediction using queuing theory and Markov Chain

5.1 Introduction

Rain attenuation is a major threat to satellite communication links operating at higher frequencies above 10 GHz [*ITU-R P.618-13, 2017*]. Rain fade mitigation techniques such as site diversity technique are among techniques that can be utilized on earth-satellite links to improve system reliability and availability. In the previous chapter, rain attenuation was predicted using the backpropagation neural network technique. This chapter uses the queueing theory technique to investigate the length of time a cloud shadow takes to cross an observation point on the ground. This information becomes the basis for site diversity fade mitigation techniques. Due to the increase in the number of storms over the location of study, this chapter explores the probability of occurrence of storms of different magnitudes for efficient planning and mitigation for link outages due to the rain storms.

In this chapter, the queueing theory technique and Markov chains are used to investigate the characteristics and attributes of rain storms, in addition to determining the probability of occurrence of storms of different magnitudes. Results of the investigation are thereafter compared with those that were earlier obtained earlier in Jimma, Ethiopia (7.6667°N, 36.8333°E), which is characterized by the tropical climate.

5.2 Background Information

Previous studies have confirmed that the queuing theory technique can be used to model the behavior of rain as a naturally occurring phenomenon. Three well-known random variables that are used for testing queueing theory technique (QTT) problems are the inter-arrival time, the service time and the overlap time [*Cooper, 1981; Kleinrock, 1975; Alonge and Afullo, 2014; Alonge and Afullo, 2015a*].

The application of the queueing theory concept over Durban was pioneered by *Alonge and Afullo,* (2015a). In their findings, they proposed non-Markovian distribution for rainfall service time, t_{st}, as [*Alonge and Afullo, 2015a*]:

$$f(t_{st}) = \frac{k\mu(k\mu t_{st})^{k-1}e^{-k\mu t_{st}}}{\Gamma(k)} \qquad for \quad t_{st} > 0 \qquad (5.1)$$

where k is the Erlang-k number of stages and μ is the service rate. The inter-arrival time distribution was observed to be an exponential distribution that follows a Markovian process given by:

$$f(t_{arr}) = \lambda e^{-\lambda t_{arr}} \qquad for \quad t_{arr} > 0 \qquad (5.2)$$

where λ is the data arrival rate and t_{arr} the inter-arrival time.

Results from *Alonge and Afullo* (2015b) showed that for tropical and sub-tropical locations, the steady-state queue discipline follows a semi-Markovian first-come first-served (FCFS) Semi-Markovian queue discipline ($M/E_k/s$). The same approach was used in a study in Jimma, Ethiopia by *Diba et al.* (2016) and their results showed that rain spike service time follows the Erlang-*k* probability distribution, contrary to the exponential distribution that has been adopted in past studies. Further on, *Diba et al.* (2016) characterized rainfall rate spikes over Jimma using Markov chain and results indicate that over the region, shower spikes dominate with occurrence probability of 51.26%.

Rain spike attributes of a typical rain event are shown in Figure 5.1 as service time, (t_{st}); inter-arrival time (t_{arr}); overlap time (t_{ov}) and the maximum spike rainfall rate (R_m). Similarly, Figure 5.2 shows a typical rain event with spikes of different magnitudes and width over time. The unpredictability of rain spikes occurrence with varying magnitudes and width makes it difficult to predict the magnitude or width of the next rain spike. A single rain spike within a rain event is analogous to a birth-death process with rain rates progressively building up from near zero to a spike maximum rate, R_m, and thereafter gradually reducing in magnitude with time [*Alonge and Afullo, 2015b*]. This analogy shows that a rain spike is associated with a single cloud having a maximum rain intensity at its center. Hence, it is shown that rain spikes displayed in Figure 5.2 are formed by a queue of clouds passing over a rain measurement instrument in a first come first served (FCFS) discipline.

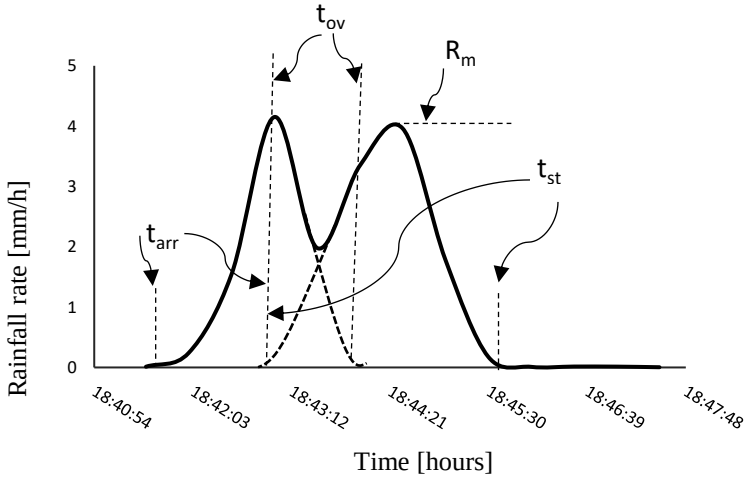

Figure 5.1 Drizzle rainfall event of 16th August 2016 at 18:41:30 hours

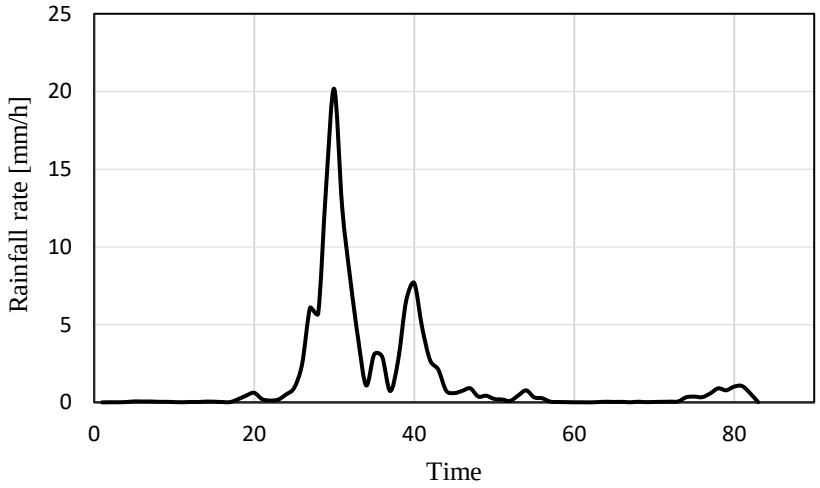

Figure 5.2 Shower rainfall event of 8th January 2017 at 09:04:00 hours

5.3 Rain Storm Modelling Using the Unified Model Language Concept

The Unified Model Language (UML) concept is used in this chapter to show the relationship that exists between elements of a rain event. In this concept, class diagrams are used to show how entities are modelled within a system by showing attributes, associations, operations and constraints that are imposed on a class [*Rambaugh et al., 2005*]. In brief, a *class* represents an

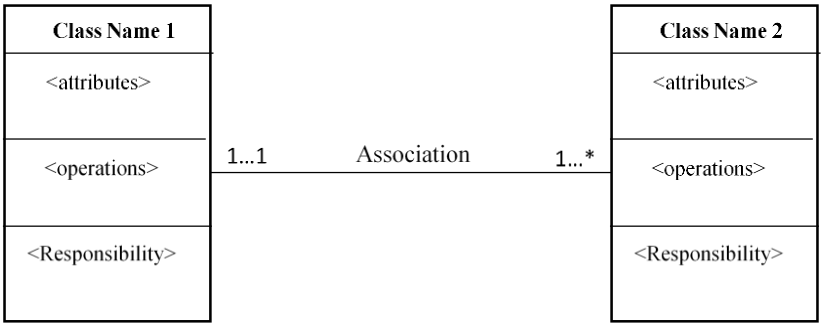

Figure 5.3 A UML typical class diagram

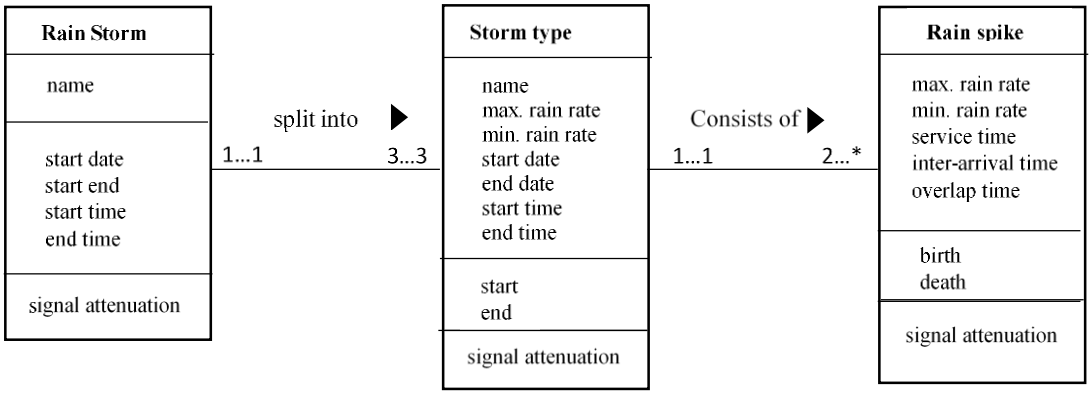

Figure 5.4 Rain storm entity class diagram

abstraction of an entity with common features whereas relationships between classes are represented by *associations.* Figure 5.3 shows a general class diagram model that can be used to model any entity within a system. From this general model, Figure 5.4 is developed to show the use of UML class diagram in modelling a rain storm (entity) with associations existing between the rain storm event and rain spikes within the storm. For For application of the queuing theory concept, the cardinality of the rain spike is given in Figure 5.4 as "2…*". This implies that, for successful extraction of the three queueing parameters, the storms to be considered need to comprise two or more rain spikes. This is an example of a constraint on the storm to be used with QTT. A detailed description of Figure 5.4 is given in *Ahuna et al.* (2018a). In addition, it is shown in the same figure that the three classes are responsible for signal attenuation, though with different magnitudes as low as 1 dB for drizzle spikes and over 10 dB for storm rain spikes.

5.4 Methodology

Precipitation measurements were carried out as described in *Section 3.2.1* and comprised of 30-sec sampled data collected from 2013 to 2017. Data used in this chapter is retrieved from convective rainfall regimes of shower and storm types with rain rates, $R \geq 10$ mm/h. This choice is motivated by the higher contribution towards signal impairment over LOS radio links by these two kinds of rainfall regimes. The data was further categorized into drizzle (D), widespread (*W*), shower (*Sh*), storm 1 (S_1), storm 2 (S_2) and storm 3 (S_3) rain spikes as shown in Table 5.1. Storm subdivisions are is necessitated by the wide gap between the minimum rain rate of 40 mm/h and a maximum of 253.066 mm/h obtained from measurements. Analysis of storm occurrences of storms over Durban is done over a period of 57 consecutive months from April 2013 to December, 2017 and this is motivated by the sudden rise in the number of rain storms and their higher magnitudes over the region of study as shown in Figure 3.1 and Table 3.3 and Table 3.6.

5.5 Results Analysis and Discussions

The three queuing parameters mentioned in *Section 5.3* are analyzed in this section and the results are summarized in Table 5.2. Subsequently, probabilities of storm occurrences of storms of different magnitudes are analyzed using the Markov Chain technique.

Table 5.1 Statistics for shower and storms regimes

Rain Rate Regime	**Range of R_{max} [mm/h]**	**Samples used**	**%**
Drizzle (*D*)	$R < 5$	125	17.6
Widespread (*W*)	$5 \leq R < 10$	130	18.3
Shower (*Sh*)	$10 \leq R < 40$	283	39.8
Storm 1 (S_1)	$40 \leq R \leq 100$	135	19.0
Storm 2 (S_2)	$100 < R \leq 150$	20	2.8
Storm 3 (S_3)	$R > 150$	18	2.5

5.5.1 Spike Service Time Distributions

In Figure 5.5 we present service time distributions with Figure 5.5(a) showing are distributions for the shower regime and Figure 5.5(b) showing distributions for storms. It is evident that both service times for measured data can be approximated by the Erlang-*k* distribution with $k = 2$ and $k = 3$ for shower and storm regimes respectively. The Erlang-*k* distribution is given by [*Alonge and Afullo, 2015a; Adan and Resing, 2015*]:

$$f(x) = \mu \frac{(\mu x)^{k-1}}{(k-1)!} e^{-\mu x} \tag{5.3}$$

where μ is the scale parameter and k is the shape parameter. The number of rain spikes for which service time is exceeded is shown in Figure 5.6, where it is observed that the number of shower spikes outnumber those of the storm spikes for the same service time. Further analysis shows that it takes shorter time for high-magnitude storms to traverse a given region compared to those with lower magnitudes. For instance, it is shown in Table 5.2, that it takes, on average, 21.13 minutes

Table 5.2 Spike Queuing Parameters

Parameter	**Rainfall regime**	**Average time [min]**	**Best fit Distribution**	**RMSE**	**CHI**
Service time, t_{st},	$c_{x,Sh} = 0.7201$	21.13	Erlang-*k*, $k = 2$	0.0059	0.0931
	$c_{x,St} = 0.6712$	13.00	Erlang-*k*, $k = 3$	0.0092	0.2390
Inter-arrival Time, t_{arr}	$c_{x,Sh} = 0.4807$	16.28	Erlang-*k*, $k = 2$	0.0057	0. 2306
	$c_{x,St} = 1.0996$	8.47	Exponential	0.0092	0.1445
Overlap Time, t_{ov}	$c_{x,Sh} = 0.8702$	3.16	Erlang-*k*, $k = 2$	0.0128	0.4070
	$c_{x,St} = 0.6067$	2.79	Erlang-*k*, $k = 3$	0.0471	0.1563
Spike Max. Rain Rate, R_m	$c_{x,Sh} = 0.7335$	-	Erlang-*k*, $k = 2$	0.0068	0.0352
	$c_{x,St} = 0.8964$	-	Exponential	0.0024	0.0609

$c_{x,Sh}$ and $c_{x,st}$ are coefficients of variation for shower and storms regimes respectively

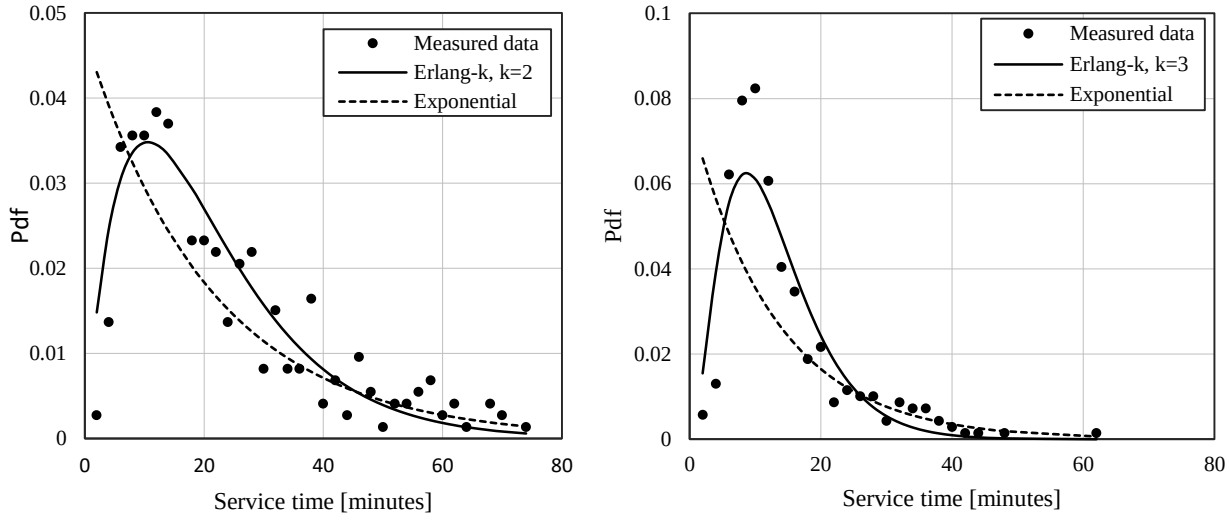

(a) (b)

Figure 5.5 Service time distributions for (a) shower and (b) storm rainfall regimes

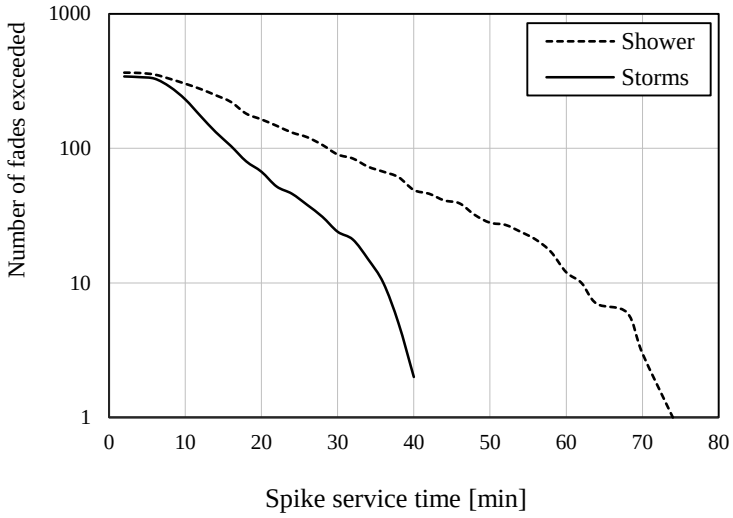

Figure 5.6 Number of rain spikes exceeded

for shower clouds to traverse a region as compared to 13.00 minutes for storm clouds. The traversal time of 13.00 minutes is comparable to 13.32 minutes obtained by *Diba et al.* (*2016*) for rain storm spikes over Jimma, a tropical climate. This comparison is shown in Table 5.3. Further analysis shows that service times for shower spikes are longer over Durban compared to Jimma, contrary to service times for storms where spikes have relatively higher service times in Jimma compared

Table 5.3 Service time comparisons for Durban and Jimma

Model	Regime	Service time distribution	Average Spike Service Time (minutes)
Diba et al., 2016 (Jimma)	Shower	E_k, $k = 4$	16.8390
	Storms	E_k, $k = 4$	13.3237
Durban	Shower	E_k, $k = 2$	21.1336
	Storms	E_k, $k = 3$	13.0028

to Durban region. It is also noted that for both regions, measured data can be approximated by Erlang-*k* distributions with *k* taking values in the range $2 \leq k \leq 4$.

5.5.2 Spike Inter-Arrival Time Distributions

The time interval for arrival of two consecutive rain clouds as observed from a stationary point is referred to as the inter-arrival time. These times are presented in Table 5.2 for both shower and storm rain events and results show that these times are 16.28 minutes and 8.47 minutes for shower and storm regimes, respectively. From Figure 5.7, it is observed that the spike inter-arrival time for shower regimes follow the Erlang-*k* distribution with $k = 2$, whereas those for storms follow the exponential distribution, similar to results that were obtained by *Alonge and Afullo*, (2015a).

5.5.3 Spike Over-Lap Time Distributions

It is evident from Figure 5.1 shows that there exists an overlap time, t_{ov}, over which two rain spikes overlap in time. The overlap time distributions are shown in Figure 5.8, where spikes in both types of regimes follow the Erlang-*k* distribution with $k = 2$ and $k = 3$ for shower and storm regimes, respectively. Overlap time distributions are expected to follow the Erlang-*k* distribution because overlap times are subsets of service times. Results presented in Table 5.2 show that rain spikes in shower and storm regimes overlap for a mean duration of 3.16 minutes and 2.79 minutes, respectively. For storms, results from *Alonge and Afullo* (2015a) showed a corresponding mean overlap time of 5.75 minutes for storms, over Durban region. One explanation for the difference in the two overlap times in the same location can be described by analysis carried out in the next chapter on rain fade statistics, where it is revealed that for the same rain rate, rain spikes that occurred during storm periods last for a shorter period than their pre-storm counterparts.

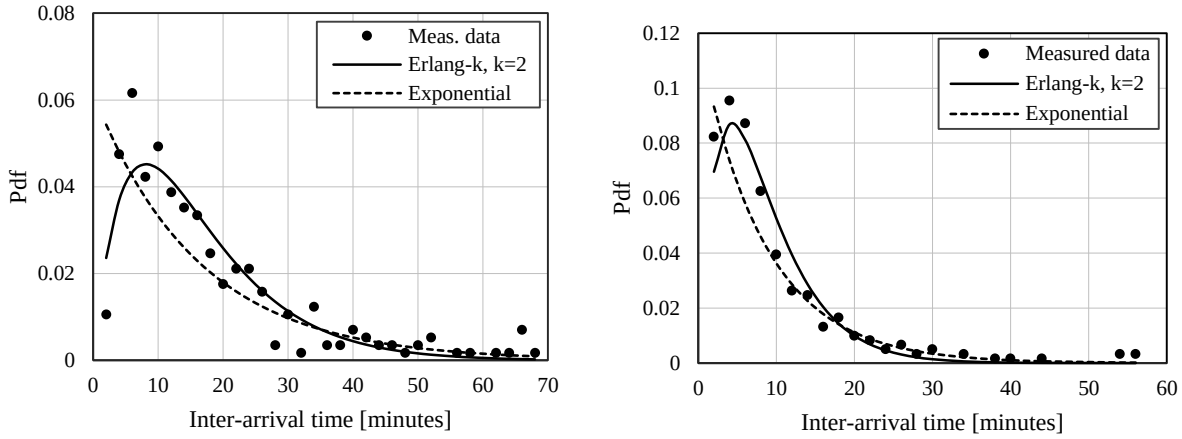

(a) (b)

Figure 5.7 Inter-arrival time distributions for (a) shower and (b) rain storm regimes

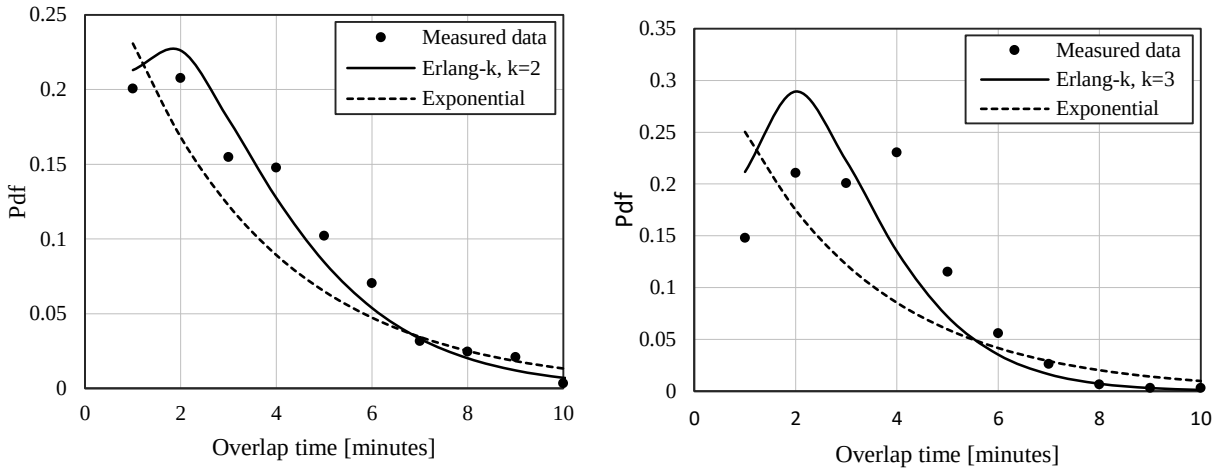

(a) (b)

Figure 5.8 Overlap time distributions for (a) shower and (b) storm rainfall regimes

5.5.4 Correlation Between Spike Maximum Rain Rate with Spike Diameter

For every rain spike, there exists a rain rate, R_{max} mm/h, with the highest value. This rain rate is referred to in this section as the maximum rain rate. In Figure 5.9, we present R_{max} distributions for shower and storm regimes. Results show that, for this parameter, shower regimes and storm regimes follow Erlang-*k* and the exponential distributions, respectively. Further, examination of the relationship between spike diameters and R_{max} was carried out and results are presented in Figure 5.10.

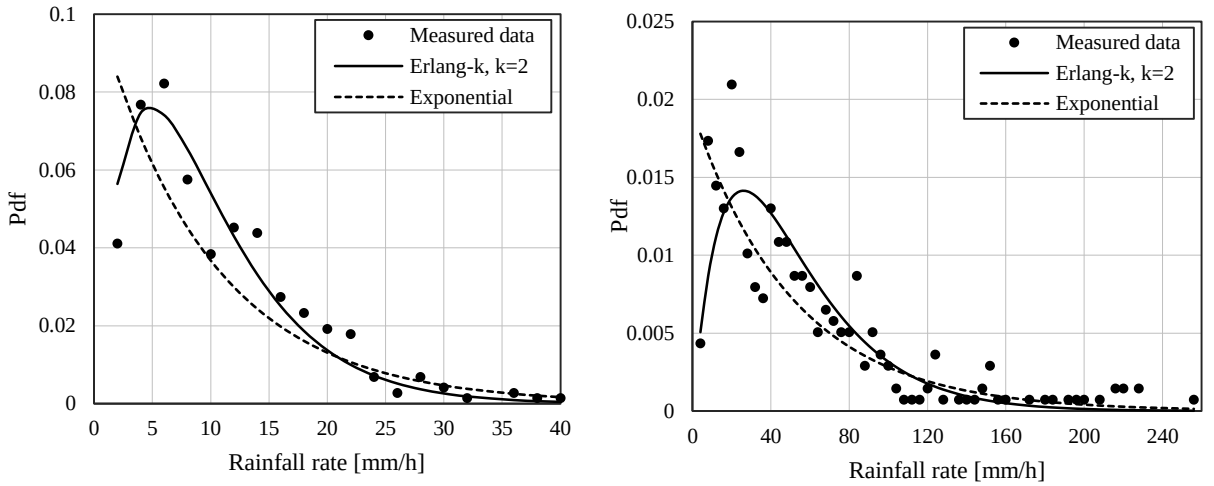

(a) (b)

Figure 5.9 Spike R_{max} distributions for (a) shower and (b) storm rainfall regimes

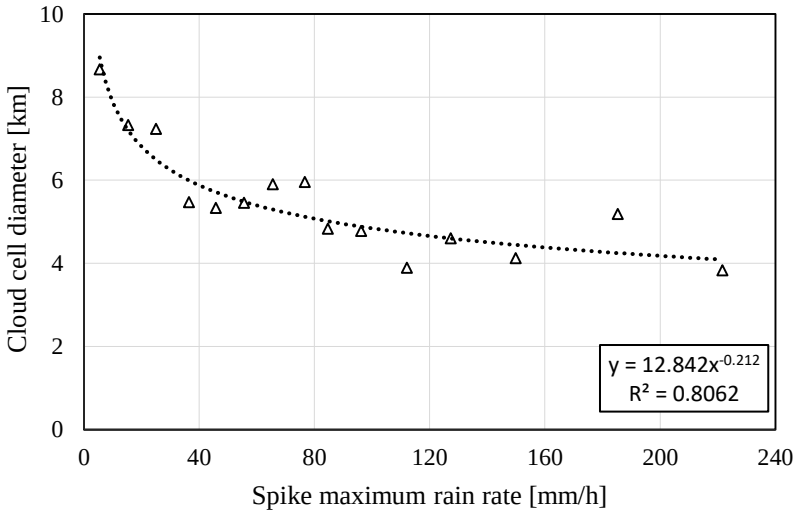

Figure 5.10 Cloud cell diameter versus R_{max}

Results of this examination show that the diameter of a rain spike is a function of the maximum R_{max} with low magnitude spikes having larger diameters compared to higher magnitude spikes. For instance, it is observed that spikes with R_{max} below 10 mm/h have, on average, diameters of about 8.5 km. On the other hand, spikes with maximum rain rates $90 \leq R_{max} \leq 100$ mm/h take on values of about 4.8 km. These diameters are calculated using advection velocities of 6 m/s and 10

m/s for shower and storm rain cells, respectively [*Pawlina, 2002; Akuon and Afullo, 2011*b]. Analysis of the relationship that exists between R_{max} and the spike diameter yields a power-law function that can be used to estimate the diameter, D_{sp}, of a rain spike and is given as:

$$D_{sp} = c_1 {R_{max}}^{c_2} \qquad [km] \tag{5.4}$$

where coefficients c_1 and c_2 are found to be 12.842 and -0.212 respectively. From analysis of thequeuing parameters shown in Table 5.2, a rain event cell diameter, D_{ev}, can be estimated as:

$$D_{ev} \approx wD_{sp} - (w-1)D_{ov} \qquad [km] \tag{5.5}$$

where *w* is the mean number of spikes within a rain event, D_{sp} and D_{ov} are rain spike diameter and the overlap distance, respectively, both in km. Hence, from (5.4) and (5.5) in conjunction with the knowledge of the overlap time described in *Section 5.6.3*, the stretch of any rain event can be determined. For clarity, a rain event is regarded as the continuous time in which R > 0 with one or more spikes present.

Knowledge on the coverage distance of a rain event is important for site diversity as a rain fade mitigation scheme. Link designers are keen on maximizing site diversity gain by considering the minimum distance required between two earth stations. This ensures that the two or more earth

Table 5.4 Comparison of rain cell sizing

Model	**Region of study**	**Approach**	**Rain cell diameter**
Khamis et al., (2004)	Subang, Selangor, Malaysia	$R_{0.01}$ rain rate	1.2 km ≤ D ≤ 1.5 km for $R_{0.01}$ = 120 mm/h
Begun and Otung (2009)	Sparsholt, United Kingdom	Synthetic Storm Technique and rain rate time series	D < 10 km for intense rain cells
Akuon and Afullo (2011)	Various climatic zones, South Africa	Synthetic Storm Technique and 1-minute rainfall distributions	D = 7.75 km for R_{max} = 60 mm/h
Proposed model	Durban, South Africa	Queueing Theory Technique	D = 5.39 km for R_{max} = 60 mm/h

stations are not located under the same rain intense rain clouds. Using the synthetic storm technique and rain rate time series, *Begun and Otung* (2009] determined the partial structure of rain cells over Sparsholt, UK. Results of their investigation showed that intense rain cells cover less than 10 km. Similarly, investigations carried out by *Akuon and Afullo* (2011b] show that rain cells with rain rate threshold of 60 mm/h cover distances up to 7.75 km. Their investigations were carried out over different climatic regions in South Africa using the synthetic storm technique and 1-minute rainfall distributions. Over Durban, a cell with R_{max} = 60 mm/h yields a cell diameter of 5.39 km, which is comparable to the results of *Akuon and Afullo,* (2011b]. A comparison of three rain cell sizing model is shown in Table 5.4.

5.5.5 Rain Spike Magnitude Prediction Using Markov Chain Approach

Prediction of the amount of rain attenuation can be achieved with the knowledge of the magnitude, R_m, of the rain spike that is to arrive next. This prediction becomes more accurate if there is a known probability of occurrence of different rain magnitudes. The prior knowledge of the amount of attenuation prepares the system to engage necessary fade mitigation measures that will ensure link availability during a rain storm. In this chapter, the *N*-state Markov Chain approach is used to investigate the natural arrival of rain spikes of different magnitudes within the regions of study [*Bolch et al., 1998*].

This investigation considers six states, where 'state' represents a type of a rain regime. The six states of investigation are drizzle (*D*), widespread (*W*), shower (*Sh*), storm 1 (S_1), storm 2 (S_2) and storm 3 (S_3) whose rain rate bounds are given in Table 5.1. This analysis uses data sourced from convective rain events due to their significant contribution to signal attenuation. A 3×3 state transition matrix for the shower regime is presented as:

$$P_{ij,(Sh)} = \begin{bmatrix} DD & DW & DSh \\ WD & WW & WSh \\ ShD & ShW & ShSh \end{bmatrix} \tag{5.6}$$

where *WD* represents a state transition from widespread spike to drizzle spike, with other states defined in the same way. Our investigation from measured data yielded a rain spike transition graph presented in Figure 5.11 and the state transition matrix as:

$$P_{ij,(Sh)} = \begin{bmatrix} 0.4609 & 0.2783 & 0.2609 \\ 0.2800 & 0.2000 & 0.5200 \\ 0.2483 & 0.3221 & 0.4295 \end{bmatrix} \tag{5.7}$$

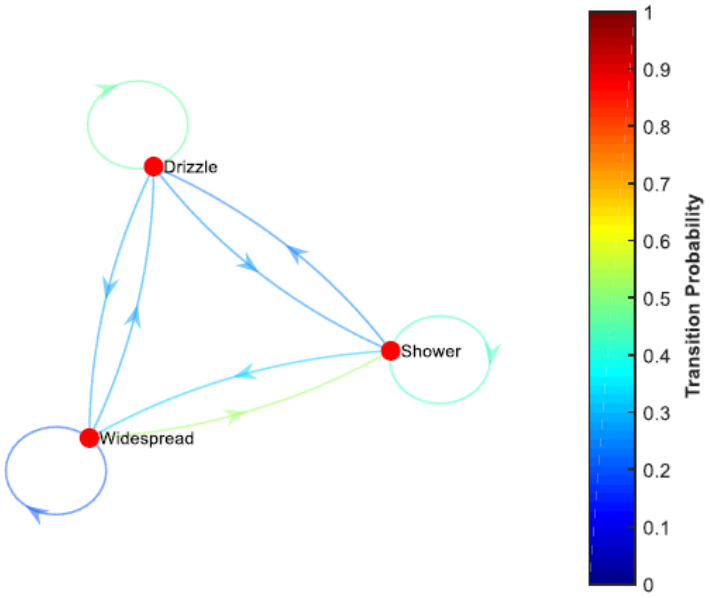

Figure 5.11 Spike transition graph for shower regime

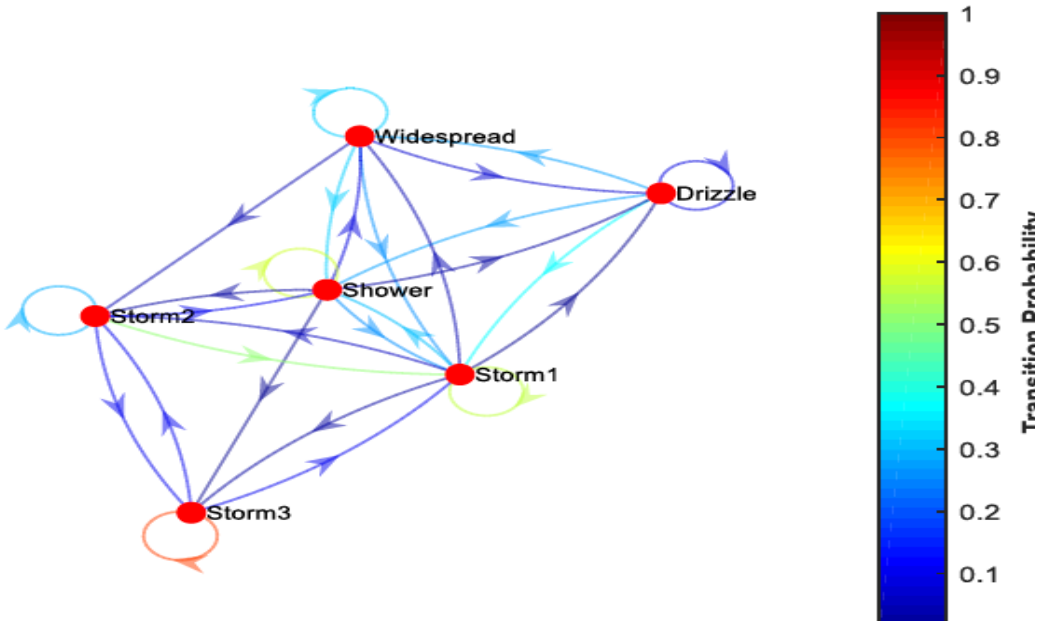

From (5.7), the initial probability matrix shows that state transitions from widespread spikes to shower spikes occur more frequently with a probability of 52% whereas the least transition occur between two widespread spikes with a state transition probability of 20%. In the same way, the 6×6 transition probability matrix for rain storm events are presented below:

$$P_{ij,(S)} = \begin{bmatrix} DD & DW & DSh & DS_1 & DS_2 & DS_3 \\ WD & WW & WSh & WS_1 & WS_2 & WS_3 \\ ShD & ShW & ShSh & ShS_1 & ShS_2 & ShS_3 \\ S_1D & S_1W & S_1Sh & S_1S_1 & S_1S_2 & S_1S_3 \\ S_2D & S_2W & S_2Sh & S_2S_1 & S_2S_2 & S_2S_3 \\ S_3D & S_3W & S_3Sh & S_3S_1 & S_3S_2 & S_3S_3 \end{bmatrix} \tag{5.8}$$

The probability transition graph for storm spikes arising from (5.8) is presented in Figure 5.12 whereas the spike transition matrix is given in (5.9). Equation (5.9) indicates that the highest transition probability occurs between S_3 spikes with a probability of 80%.

$$P_{ij,(S)} = \begin{bmatrix} 0.0909 & 0.2727 & 0.2727 & 0.3636 & 0 & 0 \\ 0.0714 & 0.3214 & 0.3214 & 0.2500 & 0.0357 & 0 \\ 0.0301 & 0.0902 & 0.5714 & 0.2632 & 0.0301 & 0.0150 \\ 0.0148 & 0.0370 & 0.3111 & 0.5556 & 0.0519 & 0.0296 \\ 0 & 0 & 0.1071 & 0.5000 & 0.2857 & 0.1071 \\ 0 & 0 & 0 & 0.1000 & 0.1000 & 0.8000 \end{bmatrix} \tag{5.9}$$

Chapman-Kolmogorov forward equations are used in this section to determine the state probability *k* steps into a chain and are given by *Kleinrock* (1975) as:

$$P^{(k+1)} = \left[P^{(k)}\right] \times [P] \quad ; \quad P_{ij}{}^{(k+1)} = \sum_{k=0}^{n} P_{ij}{}^{k} P_{kj} \tag{5.10}$$

$$\Pi_j = \sum_{i=1}^{N} \Pi_i P_{ij} \quad ; \quad \sum_{j=1}^{N} \Pi_j = 1 \tag{5.11}$$

From (5.7) and (5.10), the final state matrices for shower regimes are given as:

$$\Pi_{Sh} = [P_D \quad P_W \quad P_{Sh}] \tag{5.12a}$$

$$\Pi_{Sh} = [0.3264 \quad 0.2743 \quad 0.3993] \tag{5.12b}$$

where P_D, P_W and P_{Sh}, represent the state probabilities for drizzle, widespread and shower rains.

Similarly, from (5.9) and (5.10), the final state probabilities for storms regime are as given as:

$$\Pi_S = [P_D \quad P_W \quad P_{Sh} \quad P_{S_1} \quad P_{S_2} \quad P_{S_3}] \tag{5.13a}$$

$$\Pi_S = [0.0238 \quad 0.0769 \quad 0.3554 \quad 0.3682 \quad 0.0616 \quad 0.1142] \tag{5.13b}$$

Observations from (5.12b) shows that shower spikes have the highest probability of occurrence at 39.93% within a given shower rain event, trailed by drizzle spikes with 32.64% and at the lower

Table 5.5 Markov Chain steady state values

Model	Regime	Markovian Steady State values			
		P_D	P_W	P_{sh}	P_{S1}
Diba et al., 2016 (Jimma)	Shower	0.1733	0.3140	0.5126	-
	Storms	0.0515	0.1651	0.3344	0.4990
Durban	Shower	0.3264	0.2743	0.3993	-
	Storms	0.0238	0.0769	0.3554	0.3682

end, are widespread spikes with probability of occurrence of 27.43%. Similarly, it is observed in equation (5.13b) that S_1 spikes have the highest occurrence probability of 36.82% followed by shower spikes with 35.54% and so on. Within storm rain events, drizzle spikes have the least probability of occurrence of 2.38%.

The Markov Chain values over Durban are compared with those obtained for Jimma and the results are given in Table 5.3 and Table 5.4. This comparison reveals that, at both sites, shower spikes dominate with probabilities of 39.93% and 51.26%, respectively. For rain storms, comparison

the results show that rain storm spikes have the highest probability of occurrence compared to low magnitude spikes over both regions with values of 36.82% and 49.90% for Durban and Jimma, respectively. Future studies in this area will provide more comprehensive results due to on-going precipitation measurements in Durban, South Africa, Jimma, Ethiopia and Butare, Rwanda.

5.6 Chapter Summary

Distributions for service times, inter-arrival times and overlap times of rain spikes have been presented in this chapter. From service times and R_{max}, maximum variable models are developed for estimating the spike cell and rain event diameters. Also, from measured rainfall data, state probability matrices for shower and storm rainfall regimes are developed using the Markov Chain approach. The next chapter will explore the second order statistics, and in particular, fade durations experienced over wireless links at different attenuation thresholds.

CHAPTER 6

Second Order Rain Fade Statistics and Application for Site Diversity

6.1 Introduction

The drive to meet quality and reliability criteria and optimize system capacity has been on the rise in many regions of the world. Dynamic fading characteristics of fading require dynamic fade mitigation techniques for efficient systems and resource sharing [*ITU-R P.1623, 2005; Argota et al. 2017*]. Therefore, rain fade duration (RFD) statistics (as inputs to dynamic fade mitigation schemes) are important for design of earth-space links operating at frequencies above 10 GHz [*Matricciani and Riva, 2005*; *Cheffena and Amaya, 2008; ITU-R P.618, 2017*]. In the previous chapter, probabilities of occurrence for rain storms of various magnitudes were analyzed. In this chapter, rain fade durations at different attenuation thresholds are examined and explored for site diversity and adaptive coding and modulation fade mitigation techniques.

6.2 Background Information

The knowledge of the occurrence probability of a rain fade duration at a given attenuation threshold is an important factor that determines the performance availability and quality of service (QoS) [*Dao et al., 2013*]. Fade duration is the continuous time over which rain attenuation is above a given threshold whereas an inter-fade duration is the continuous time interval that separates two consecutive fade events, in which attenuation is below a given threshold. The third

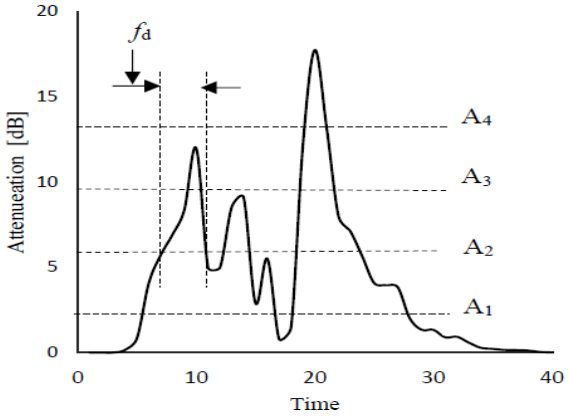

Figure 6.1 A fade duration illustration

parameter of interest in second order statistics is the fade slope. This is defined as the rate of change of attenuation with time. The duration of a rain fade determines the period in which a communication link becomes degraded or unavailable and is an important input for planning and applying dynamic fade mitigation. Figure 6.1 shows an example of a rain fade, f_d, measured at an attenuation threshold of A_2 dB. This figure was derived from a rain event of 20th February, 2014 from 19:58:30 hours.

6.3 Methodology

Precipitation data used in this chapter was obtained as described in Section 3.2.1 and spans for a period of 5 years, similar to data used in *Chapter 5*. Once again, this data was categorized into two periods of PSP (2013-2015) and SP (2016-2017) for comparison of results. In both year periods, convective rainfall events with $R_{max} \geq 10$ mm/h, are considered for analysis. Rain events considered in this chapter are categorized into six categories of shower 1 (Sh_{1yz}), shower 2 (Sh_{2yz}), storm 1(S_{1yz}) and storm 2 (S_{202}), and storm 3 (S_{302}) as shown in Table 6.1 and 6.2. Cases where the mid subscript is zero means that the rainfall regime was never subdivided into parts. Measured rain data was converted into the corresponding rain attenuation time series using the model developed by *Matricciani* (1996) and the input parameters to this model were determined using a link with an elevation angle of 36.5° operating at a frequency of 12 GHz. Finally, fade duration statistics were extracted from rain attenuation time series data using MATLAB® codes that was developed for this purpose.

Table 6.1 Convective rain events categories (PSP)

R_{max} bounds [mm/h]	Regime Label
$10 \leq R < 20$	Sh_{101}
$20 \leq R < 40$	Sh_{201}
$40 \leq R < 60$	S_{101}
$R > 60$	S_{201}

Table 6.2 Convective rain events categories (SP)

Rain Rate Bounds [mm/h]	Regime Label
$10 \leq R < 20$	Sh_{102}
$20 \leq R < 40$	Sh_{202}
$40 \leq R < 60$	S_{112}
$60 \leq R < 100$	S_{122}
$100 \leq R < 150$	S_{202}
$R > 150$	S_{302}

Attenuation thresholds of 1.28 dB, 2.78 dB, 6.02 dB, 13.05 dB, 20.51 dB, 36.25 dB and 56.98 dB are used in this study, corresponding to attenuation caused by rain rates of 5 mm/h, 10 mm/h, 20 mm/h, 40 mm/h, 60 mm/h, 100 mm/h and 150 mm/h respectively. Other than the 5 mm/h, the rest are lower rain rate bounds for Sh_{1yz}, Sh_{2yz}, S_{1yz}, S_{202}, and S_{302}, as shown in Table 6.2.

6.4 Results and Discussion

In this section, we discuss the results of this study in two parts: (1) long-term attenuation statistics and (2) second order rain fade statistics.

6.4.1 Long-Term Attenuation Statistics

Long-term attenuation prediction provides information on attenuation exceeded for a given percentage, *p*, of time in an average year. Figure 6.2(a) and Figure 6.2(b) show complementary cumulative distribution functions (CCDFs) for pre-storm and storm year periods, respectively. The three CCDFs are compared and the results are shown in Table 6.3 and Table 6.4 for PSP and SP periods respectively. Comparisons show a general agreement in attenuation values derived

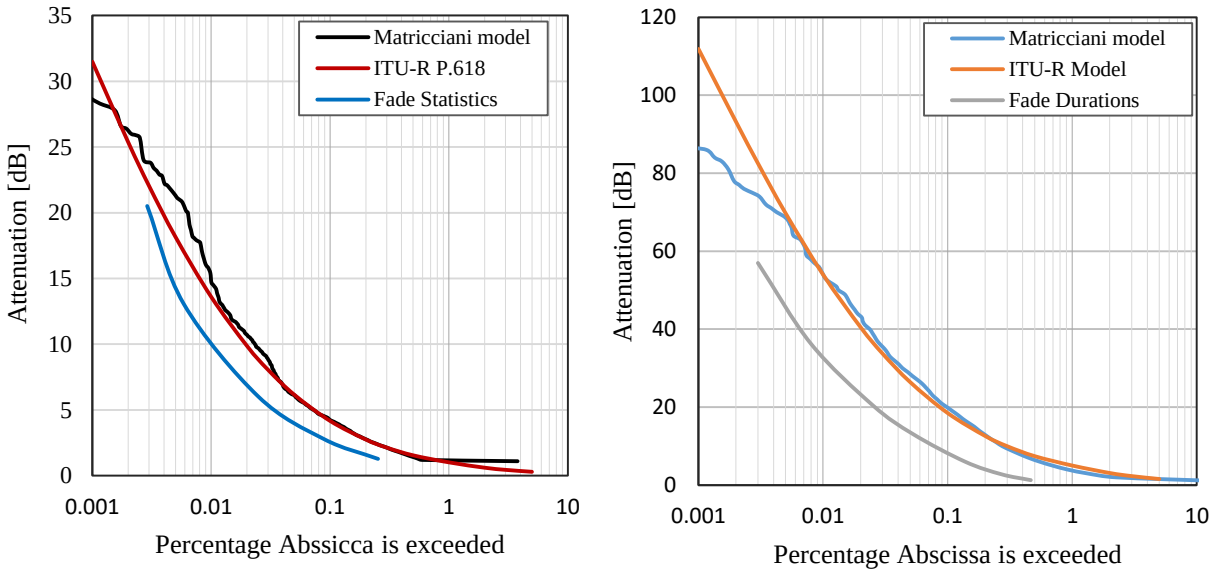

(a) (b)

Figure 6.2 Complementary CDF of attenuation exceeded during (a) PSP period (b) SP period

Table 6.3 Attenuation exceeded (PSP)

%	SST Model [Matricc.]	ITU-R Model [ITU-R P.618-13]	Proposed model (Fade durations approach)
1	1.0	1.0	-
0.5	1.4	1.6	-
0.3	2.1	2.1	-
0.1	4.2	4.2	2.5
0.05	6.1	6.2	4.0
0.03	8.8	8.1	5.7
0.01	14.7	13.6	10.2
0.005	21.3	18.2	15.5
0.003	23.8	22.0	20.51

Table 6.4 Attenuation exceeded (SP)

%	SST Model [Matricc.]	ITU-R Model [ITU-R P.618-13]	Fade durations approach
1	3.8	5.0	-
0.5	5.5	7.4	-
0.3	9.3	10.0	2.5
0.1	19.0	18.5	9.5
0.05	28.5	26.4	14.0
0.03	35.5	33.8	19.1
0.01	54.0	54.0	34.3
0.005	68.5	69.8	49.2
0.003	74.0	82.5	56.98

from ITU-R P.618 model and *Matricciani* (1996) model for percentages down to around 0.01% as shown in Figure 6.2(a) during PSP period. Similarly, in Figure 6.2(b) it is observed that, for the two models, the agreement of results stretch down to 0.005% of an average year, during SP period. Further analysis shows that long-term attenuation values derived from RFDs are lower values compared to the other two models. One possible explanation for these lower values is that fade duration statistics do not consider the depth of a fade, but rather, its duration at a given threshold. For instance, it is noted that the margin between exceeded fades during SP period shown in Figure 6.2(b) is higher than that obtained during PSP period at 0.01% of an average year. Results show

that, for the PSP period, attenuation exceeded for 0.01% of an average year are 14.7 dB, 13.6 dB and 10.2 dB for *Matricciani* model, ITU-R P.618 model and fade statics approach, respectively. Similarly, for the SP period corresponding values are 54.0 dB, 54.0 dB and 34.3 dB for *Matricciani* model, ITU-R P.618 model and fade statics approach, respectively. Further, it is observed that there is a margin of approximately 20 dB between RFD approach and the other two models at 0.01% probability during SP period. Similarly, a margin of 4.5 dB is observed between the RFD approach and the other two models during the PSP period at the same probability of exceedance. More conclusive results on the margin may obtained using data collected over a relatively longer period such as 10 years and above. Table 6.2(a) and Table 6.2(b) show more statistics on other percentages of exceedances.

6.4.2 Rain Fade Duration Statistics

This subsection presents rain fade statistics that are computed for the pre-storm and storm periods at the thresholds given in *Section 6.3*. These results are shown in Table 6.5 and Table 6.6 for PSP and SP periods, respectively. Analysis of mean fade durations was performed and results show that these values decrease with increase in fade thresholds. For instance, on average, a spike in PSP is observed to last for about 2.13 minutes at a threshold of 2.78 dB while it lasts for about 1.5 minutes at a threshold of 20.51 dB. Corresponding values for storm periods are 2.35 minutes and 1.52 minutes at the same fade thresholds. Generally, comparison results show that mean fade durations are higher for convective rains during storm periods compared to pre-storm periods, despite the smaller mean rain event duration indicated in Table 6.4. One possible explanation for this is that high intensity rain spikes have steeper slopes, hence larger widths at higher fade thresholds, especially for mid-range thresholds. This is evident from Table 6.5 and Table 6.6 where the lowest and highest thresholds have lower mean fade durations than in PSP period.

Further analysis shows that median fade durations over Durban are in the range of 1 minute and 1.5 minutes for PSP whereas they range from 0.5 minute to 1 minute for SP. Results for median fade durations over Durban are compared to those obtained by *Cox and Arnold* (1982] and are found to be lower. In their study, *Cox and Arnold,* (1982) used a link operating at a frequency of 19 GHz with an elevation angle of 18.5°. Their results revealed median fade durations ranging from 2.8 minutes to 7.5 minutes with fade thresholds from 5 dB to 40 dB. A possible explanation for lower values of median fade duration over Durban is the lower frequency of operation and a

higher elevation angle. Previous studies have proven that the fade duration is a function of both elevation angle and the frequency of operation [*Mitchel et al., 1997; Acosta, 1997*].

In Figure 6.3, we show distributions of number of fade events that last for a time duration longer than *D* sec at different fade thresholds. A comparison is made between two year periods and plots

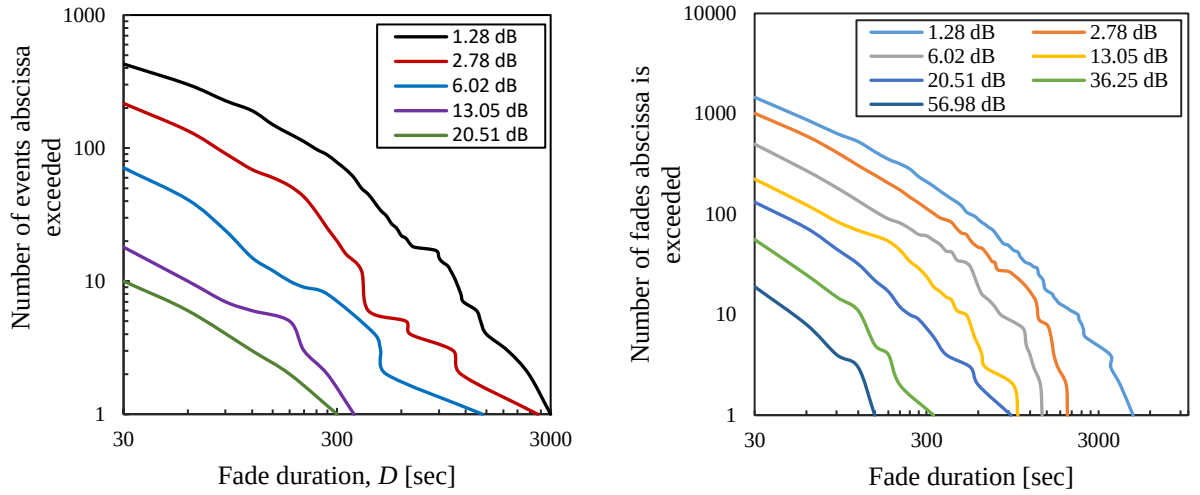

(a) (b)

Figure 6.3 Number of events with fade durations greater than a given fade duration for (a) PSP (b) SP

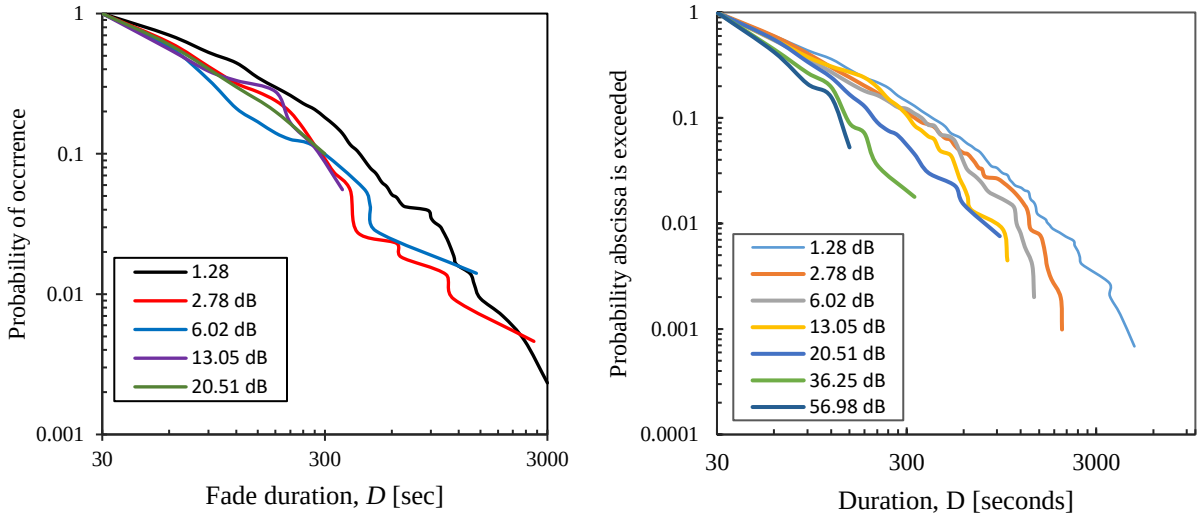

(a) (b)

Figure 6.4 Probability of occurrence fade events with $F_D \geq D$ sec for (a) PSP (b) SP

Table 6.5 Fade Duration Statistics (PSP)

Fade threshold [dB]	**Mean fade duration [min]**	**% of time $a \geq A$ in a rain event**	**Total number of samples**
1.28	184	13.6	430
2.78	128	5.7	218
6.02	109	3.2	71
13.05	102	3.0	18
20.51	90	1.3	10

Table 6.6 Fade Duration Statistics for SP

Attenuation threshold [dB]	**Mean fade duration [sec]**	**% of time $a \geq A$ dB in a rain event**	**Total number of samples**
1.28	174	24.23	1430
2.78	141	13.66	989
6.02	128	9.37	494
13.05	119	8.24	222
20.51	91	5.49	132
36.25	65	4.06	57
56.98	55	1.82	22

Table 6.7 Number of Fades exceeded at *D* sec

Fade thresh. [dB]	**Number of fades**						
	PSP				SP		
	1 min	3mins	5 mins		1 min	3mins	5 mins
1.28	301	128	78		877	282	49
2.78	135	52	20		603	148	27
6.02	41	10	7		272	72	9
13.05	10	5	2		124	34	-
20.51	6	2	1		73	10	-
36.25	-	-	-		25	-	-
56.98	-	-	-		8	-	-

show similar trends, with lower thresholds plots showing higher values than lower thresholds. For example, at a boundary of 3 minutes, the number of fades that last for this duration or longer are found to be 10 and 5 at thresholds of 6.02 dB and 13.05 dB, respectively, during the PSP period. In the same way, the values are 90 and 54 at the same thresholds during SP period. These statistics are given in Table 6.7.

Figure 6.4 shows the probability of occurrence of fade spikes with duration $d \geq D$ sec during both year periods. Observations show that trends in both year periods are similar. For instance, the

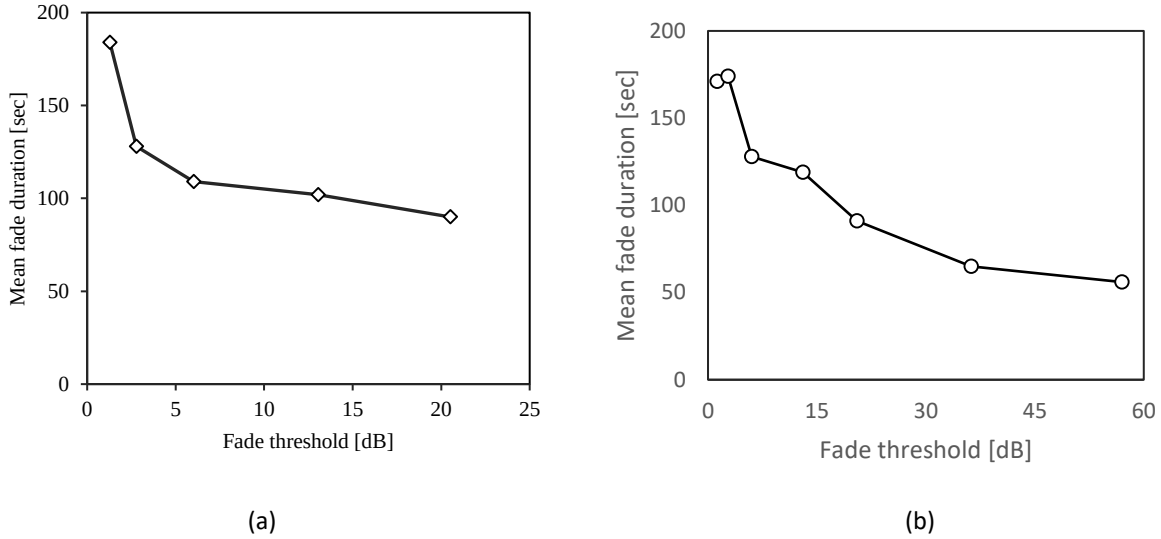

Figure 6.5: Mean fade durations at different fade thresholds during (a) PSP (b) SP

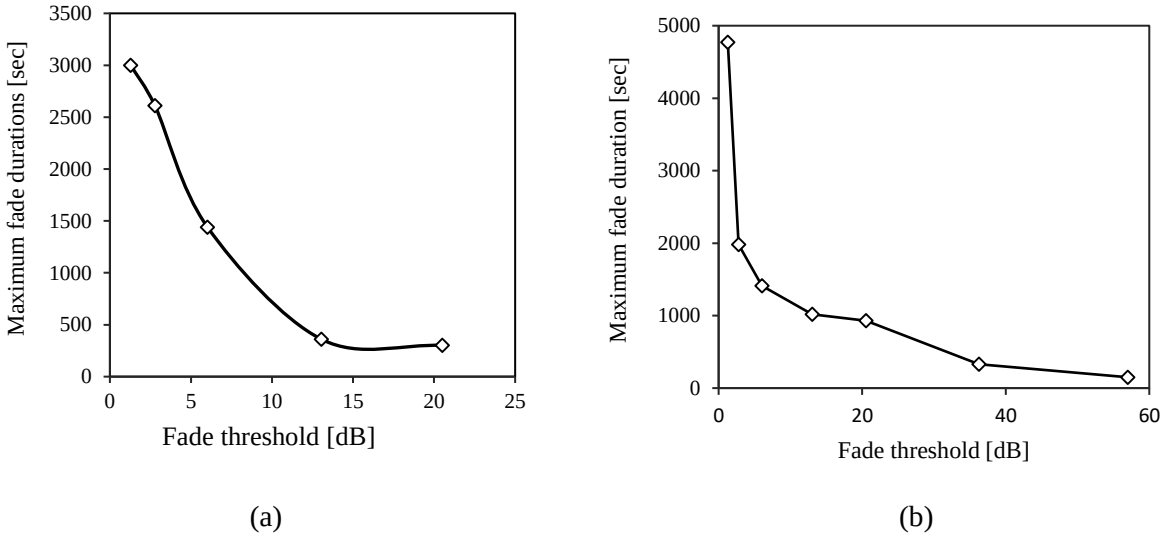

Figure 6.6 Maximum fade durations at different fade thresholds during (a) PSP (b) SP

probability of occurrence of fades lasting for 6 minutes or more is 5.6% at a fade threshold of 13.05 dB during the pre-storm period whereas it is 7.6% during SP period.

The mean and maximum fade durations were plotted against fade thresholds and results are shown in Figure 6.5 and Figure 6.6, respectively. Similar trends are observed for the two year periods indicating that the two parameters, $F_{\mathrm{D,mn}}$ and $F_{\mathrm{D.mx}}$ decrease as fade thresholds increase, though the gradient is smaller at higher thresholds.

From results of Table 6.5 and Figure 6.5, two power-law relationships are obtained for estimation of the mean fade duration, $F_{\mathrm{D,mn}}$ and the maximum fade duration, $F_{\mathrm{D,mx}}$ during the pre-storm period. These functions are given as:

$$F_{\mathrm{D,mn}} = 178.34A^{-0.235} \qquad [sec] \tag{6.1}$$

$$F_{\mathrm{D,mx}} = 5160A^{-0.925} \qquad [sec] \tag{6.2}$$

Similarly, using Table 6.6 and Figure 6.6 results, the two parameters for the SP period are estimated as:

$$F_{\mathrm{D,mn}} = 218.04A^{-0.31} \qquad [sec] \tag{6.3}$$

$$F_{\mathrm{D,mx}} = 5908A^{-0.792} \qquad [sec] \tag{6.4}$$

Equations (6.1) and (6.3) may become useful in determining the distance of separation between two or more earth stations when applying site diversity as a fade mitigation scheme. On the other hand, (6.2) and (6.4) provide information on the worst case scenario where a fade is longest at a given fade threshold.

6.5 Application of RFD statistics for Site Diversity

In this section, rain fade duration statistics are applied in two types of dynamic fade mitigation, namely: site diversity and adaptive coding and modulation.

6.5.1 Application of RFDs for Site Diversity

The spatial variability of rain makes it possible for implementation of site diversity. Convective rains occur with high rain rates though they cover shorter distances of up to 5 km [*Panagopoulos et a., 2004; Ahuna et al., 2018a*]. Also, it is a general agreement that fading at two sites separated by a distance greater than the average size of the rain cell will be uncorrelated [*Acosta, 1997*]. In this scenario, the two stations that are separated by a distance greater than the average cell diameter

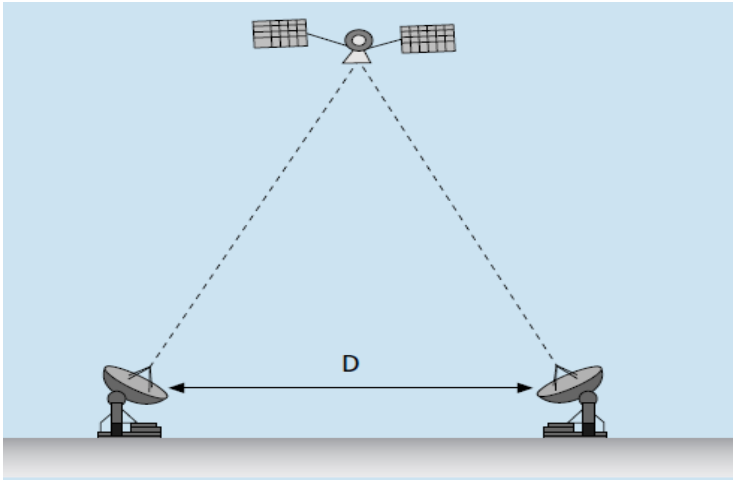

Figure 6.7 Double-site diversity [*Panagopoulos et al., 2004*]

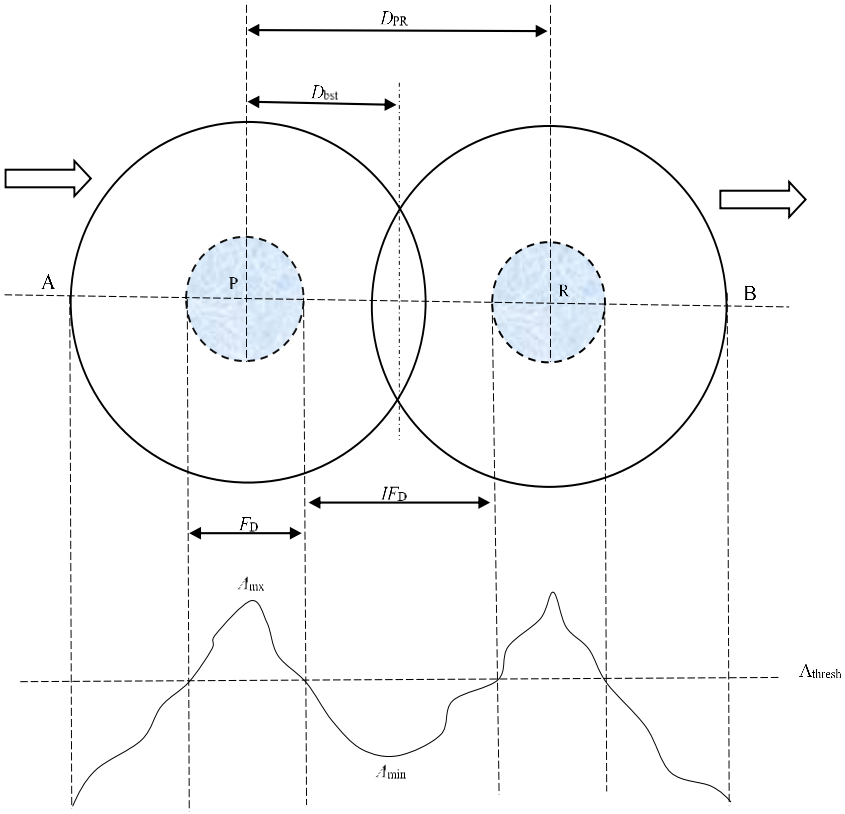

Figure 6.8 Illustration of double-site diversity

are safeguarded from being covered by the same rain cloud. On the other hand, rain cells usually appear in queues and hence we need to consider the probability of the two stations being covered

by two adjacent rain cells at the same time. In this section, we have considered this second scenario.

Figure 6.7 shows double-site diversity technique that utilizes two earth stations receiving the same signal from one satellite. This is beneficial because the site with less or no fading can re-route stronger data traffic to those sites that are affected by rain fading through alternative paths.

Figure 6.8 shows an example of two consecutive fade cells moving in the direction AB with maximum fades at their centers, points P and Q. The area of inner circles represents fades above, A_2 dB threshold. Separating these two stations with a distance less than D_{PQ} gives good results, though a separation distance equal to D_{bst} yields the best results, with an assumption that these rain cells are circular and only one layer of clouds exists. Two instances can be considered here: (1) that one station is under maximum fading while the other is under minimum fading conditions or (2) both stations are under fading conditions with attenuation below the A_2 dB threshold, and eventually, improving the link reliability and performance. With analysis of Figure 6.8 and an advection velocity of 10 m/s, the best separation distance D_{bst}, is given by:

$$D_{\text{bst}} = 5\left[F_{D,mn} + IF_{D,mn}\right] \qquad [m] \tag{6.5}$$

where $F_{D,mn}$ is as defined in (6.1) and $IF_{D,mn}$ is the mean inter-fade duration at an attenuation threshold, A_2 dB shown in Figure 6.8.

6.5.2 Rain fade mitigation using ACM

Due to dynamics of rain attenuation, dynamic fade mitigation schemes such as adaptive coding and modulation schemes can be employed for link efficiency. In dynamic schemes, system resources such as more power, are not expended during good sky (clear air) conditions. This means that the fade mitigation scheme will only be utilized depending on the current prevailing link conditions. Adaptive coding and modulation schemes are widely used techniques for improving link reliability under fading conditions. This technology enables service and network providers to achieve high-capacity data transmission. Additionally, the highest link spectral efficiency possible can be maintained throughout during data transmission under any given link condition.

In *Chapter 4*, the BPNN was utilized in the prediction of rain attenuation at time (t + 1). This shows that, for a deteriorating link, the link state can be predicted beforehand and resources allocated to guarantee link availability. The concept developed in *Chapter 4* can be used for

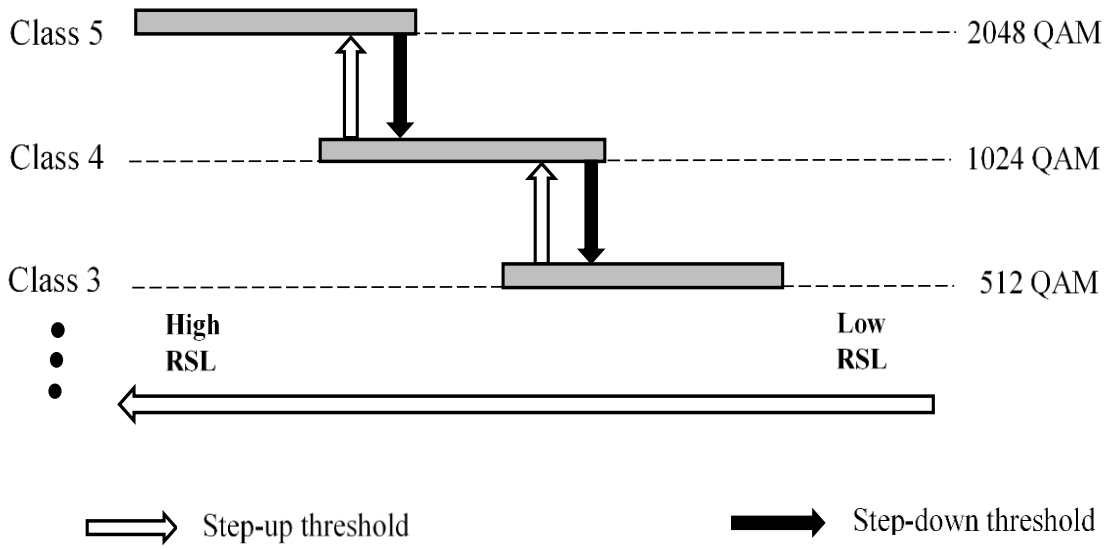

Figure 6.9 Illustration of ACM switching algorithm

deployment of ACM as illustrated in Figure 6.9. In this illustration, we assume that the received signal level (RSL) is the main factor in deciding on the level of a modulation scheme to employ under prevailing link conditions. As an example, Figure 6.9 relates to Table 4.2 with three attenuation classes (5, 4, and 3) with attenuation thresholds as shown in Table 4.2. It should be noted that relating attenuation thresholds and modulation schemes in this figure are only for illustrating the ACM concept.

The ACM switching algorithm shown in Figure 6.9, indicates that during the period when the link condition is good (high RSL), the highest modulation scheme (2048 QAM) is employed. As the link's condition deteriorates and the RSL reaches a given threshold, there occurs a modulation scheme down-shift at the step-down threshold (attention threshold). Conversely, the modulation scheme is stepped up when the RSL reaches the step-up attenuation threshold as the link conditions improves. This process is beneficial because it improves the overall link availability.

6.6 Chapter Summary

This chapter has investigated fade duration statistics and their application with site diversity as a rain mitigation technique over earth-satellite links. The chapter further illustrates an application ACM using results of *Chapter 4*. The next chapter will give a summary and the conclusions drawn from the work of this study as well as providing recommendations for future work.

CHAPTER 7

Conclusions and Recommendations for Future Work

7.1 Chapter Introduction

In this chapter we present the conclusion of the research work that has been carried out and documented in this thesis and make further recommendations on the future work.

7.2 Thesis Conclusion

In *Chapter 3*, the long-term $R_{0.01}$ parameter was examined from data spanning a period of 17 years and results show that this parameter has been rising. This information is critical for accurate estimation of rainfall attenuation over the region of study, for rain fade mitigation. Attenuation estimated from the ITU-R proposed value of between 40 – 60 mm/h will not be accurate because the current value of this parameter stands at around 132 mm/h. This is revealed using data collected in the period 2013-2017, with a lower sampling time of 30 sec.

Additionally, modelling of rain drop size distribution using the lognormal DSD is investigated in this chapter and results show that, due to intense rain storms, larger rain drops with mean diameters of over 4 mm are not well represented by the typical 3-parameter lognormal DSD. Consequently, rain attenuation estimated from measured DSDs reveal that at the same rain rate, the microwave link is exposed to higher attenuation resulting due to larger rain drops present in intense rain storms. This finding implies that specific attenuation values obtained from measured rain DSDs provide more accurate results compared to those obtained through the well-known and widely used power-law model.

In *Chapter 4*, results show that the backpropagation neural network can predict rain rate time series well, and hence, attenuation, over a communication link. This prediction is useful for dynamic rain fade mitigation over a link. Rain fade mitigation techniques such as adaptive coding and modulation techniques are applied according to the link condition, hence the need to predict the future link condition for adjustment of the modulation scheme. Moreover, results in this chapter revealed that the trained BPNN model is suitable for use in tropical regions with equatorial climate.

The Queueing theory technique was used to determine distributions of the three basic rainfall queueing parameters in *Chapter 5*. Analysis of these results show that the service time and the overlap time are best represented by the Erlang-*k* distribution, whereas the inter-arrival time for shower and storm regimes are best fitted with Erlang-*k* and the exponential distributions respectively. These parameters were subsequently used to develop a model for estimating rain cell sizes using R_{max} as the model input. This information is required for application in site diversity as a rain fade mitigation scheme. For Effectiveness, two stations are to be separated by a distance greater than the average cell diameter. This ensures that the two stations are not subjected to the fading effect of the same rain cell. Further, the Markov chains model was utilized to develop state probability matrices and it is revealed that, for storms, rain storms with maximum rain rates in the range $40 \leq R_{max} < 100$ mm/h are dominant with a state probability of 36.82%.

In *Chapter 6*, rain fade duration statistics are examined at six different attenuation thresholds ranging from 1.28 dB to 56.98 dB. Results show that the mean fade duration decreases with an increase in the attenuation threshold for both pre-storm period (PSP) and storm period (SP), with storms having relatively higher values within threshold range of $2 \leq A < 20$ dB. Further, the number of fades exceeded at a given threshold is found to be higher for the storm period compared to the pre-storm period. This indicates that fade spikes are more frequent during the SP period, hence the mitigation scheme to be employed should result in link efficiency. Using rain fade duration statistics, a model is developed for estimation of the best distance, D_{bst}, of earth stations separation that could improve the signal quality of transmission using the site diversity scheme. Lastly, the ACM technique is used as an illustration in the application for rain fade mitigation.

7.3 Recommendations for future work

- Develop or modify any existing rain DSD model that can suitably represent intense rain storms over the region of study.
- Investigate rain fade statistics using data collected at other sampling times and make comparisons with the results of the current study.
- Investigate optimal frequencies that can successfully be transmitted under different rain storm magnitudes

- In the application of the backpropagation neural network for rainfall prediction, we recommend training the BPNN using rainfall data collected at a much lower integration time of less than 30 sec and make comparisons with the current results.
- Future work should consider the effect of temperature and pressure on the maximum rain drop size within a rain storm and their relationships with D_{max}.
- Due to constant variations of fading over communication links, future work should explore the use of self-optimizing networks and how they can be designed to autonomously compensate for fading and interference and allocate radio resources for quality of service based on demand and environmental parameters.

REFERENCES

Abhishek, K., A. Kumar, R. Ranjan, and S. Kumar, "A rainfall prediction model using artificial neural network," *IEEE Control and System Graduate Research Colloquium*, pp. 82-87, 2012.

Acosta, R. J., "Rain fade compensation for Ka-band communication satellites," *NASA Lewis Research Center*, Ohio 44135, September 1997.

Adan, I. and J. Resing. *Queueing Systems*. Eindhoven University of Technology, Netherlands, March 2015. https://www.win.tue.nl/~iadan/queueing.pdf.

Adetan, O. and T. J. Afullo, "Comparison of Two Methods to Evaluate the Lognormal Raindrop Size Distribution Model in Durban," *SATNAC Proceedings*, Western Cape, South Africa, Sept. 2-5, 2012.

Adetan, O., and T. J. O. Afullo, "The critical diameters for rainfall attenuation in southern Africa," *Progress In Electromagnetic Research B,* Vol. 46, pp. 275-297, 2013.

Afullo, T. J. O., "Raindrop size distribution modelling for radio link design along the eastern coast of South Africa," *Progress In Electromagnetics Research B,* Vol. 34, pp. 345-366, 2011.

Ahuna, M. N., "Determination of Rainfall Parameters for Specific Attenuation Due to Rain for Different Integration Times for Terrestrial Line-of-Sight Links in South Africa," MSc. Dissertation, Univ. of KwaZulu-Natal, Durban, South Africa. March, 2016*b*.

Ahuna, M. N., and T. J. Afullo: "Effects of storm attenuation over satellite links in sub-tropical Africa," *2018 Progress In Electromagnetics Research Symposium (PIERS),* Toyama, Japan, 1-4 August, 2018*a*, pp. 115-120.

Ahuna, M. N., T. J. Afullo and A. A. Alonge, "Rainfall Rate Prediction based on Artificial Neural Networks for Rain Fade Mitigation over Earth-Satellite link", *IEEE Africon 2017 Proceedings*, 2017, pp. 579-584, Sept. 2017.

Ahuna, M. N., T. J. Afullo, and A. A. Alonge: "30-second and one-minute rainfall rate modelling and conversion for millimetric wave propagation in South Africa", *SAIEE Africa Research Journal*, Vol. 107, No. 1, pp. 17-29, March 2016a.

Ajayi, G. O., and E.B.C. Ofoche, "Some tropical rain rate characteristics at Ile-Ife for microwave and millimeter wave applications*," Journal of Climate and Applied Meteorology*, Vol. 23, pp. 562-567, 1984.

Ajayi, G. O., and R. L. Olsen, "Modelling of a tropical raindrop size distribution for microwave and millimeter wave applications," *Radio Science*, Vol. 20, No. 2, pp. 193-202, Apr. 1985.

Akuon, P. O, and T. J. O. Afullo, "Rain cell sizing for the design of high capacity radio link systems in South Africa" *Progress In Electromagnetics Research B,* Vol. 35, pp. 263-285, 2011.

Akuon, P. O. and T. J. O. Afullo, "Rain cell size statistics from rain gauge data for site diversity planning and attenuation prediction," *SATNAC Proceedings*, East London, South Africa, Sept. 4-7 2011.

Alonge, A. A. and T. J. Afullo, "Approximate Queue Scheduling for Rainfall Synthesis over Radio links in Subtropical Regions," *IEEE Africon Proceedings*, Addis Ababa, Ethiopia, Sept. 14-17, 2015*b*.

Alonge, A. A. and T. J. Afullo, “Characteristics of Rainfall Queues over Radio Links at Subtropical and Equatorial Africa,” *Radio Science*, Vol. 49(8), pp. 583-596, August 2014.

Alonge, A. A. and T. J. Afullo, “Estimation of Parameters for Lognormal Rainfall DSD Model for Various Rainfall Types in Durban,” *SATNAC Proceedings*, East London, Africa, Sept. 4-7 2011.

Alonge, A. A. and T. J. Afullo, “Fractal Analysis of Rainfall Event Duration for Microwave and Millimetric Networks: Rain Queueing Theory,” *IET Microwaves, Antennas Propag.*, Vol. 9(4), pp. 291-300, 2015*a*.

Alonge, A. A. and T. J. Afullo, “Seasonal analysis and prediction of rainfall effects in Eastern South Africa at microwave frequencies,” *Progress In Electromagnetics Research B,* Vol. 40, 279-303, 2012.

Argota, J. A. R., A. Fernandez, I. Anitzine, and J. Mezquita, “Analysis of rain attenuation time series from synthesizer and experimental satellite measurements,” *Proceedings of 2017 Asia Pacific Microwave Conference*, pp. 49-52, 2017.

Atlas, D. and C.W. Ulbrich, “The physical basis for attenuation-rainfall relationships and the measurement of rainfall parameters by combined attenuation and radar methods,” *J. Rech. Atmos.*, 8, pp. 275–298, 1974.

Begum, S., and I. E. Otung, “Rain cell size distribution inferred from rain gauge and radar data in the UK”, *Radio Sci*., 44, RS2015, doi:10.1029/2008RS003984, 2009.

Bezde, A. Adaptive coding and modulation (ACM) in microwave communications. January 26, 2018. Retrieved November 13, 2018: https://blog.saftehnika.com/en/whitepapers/adaptive-coding-and-modulation-in-microwave-communications/.

Bolch, G., Greiner, S., de Meer, H., Trivedi, K.S. *Queueing networks and Markov chains*. John Wiley and Sons, New York, 1998.

Brownlee, Jason. *Gentle introduction to models for sequence prediction with recurrent neural networks*. July 17, 2017. Retrieved November, 27 2018: https://machinelearningmastery.com/models-sequence-prediction-recurrent-neural-networks/.

Bryant, G. F., I. Adimula, C. Riva, and G. Brussaard, “Rain attenuation statistics from rain cell diameters and heights,” *International Journal of Satellite Communication*, Vol. 19, pp. 263-283, 2001.

A. C. Kruger and M. P. Nxumalo, “Historical trends in South Africa: 1921-2015,” Water SA, Vol. 43, No. 2, April, 2017.

Capsoni, C., F. Fedi, C. Magistroni, A. Paraboni, and A. Pawlina, "Data and Theory for a New Model of the Horizontal Structure of Rain Cells for Propagation Applications," *Radio Science*, Vol. 22, No. 3, pp. 395-404, May 1987.

Capsoni, C., L. Luini, A. Paraboni, C. Riva, and A. Martellucki, “A new prediction model of rain attenuation that separately accounts for stratiform and convective rain,” *IEEE Transactions on Antennas and Propagation*, Vol. 57, No. 1, pp.196-204, 2009.

Chebil, J. and T. A. Rahman, “Development of 1min rain rate contour maps for Microwave applications in Malaysia Peninsula,” Electronics Letts., Vol.35, 1712-1774, 1999.

Cheffena, M., and C. Amaya, "Prediction Model of Fade Duration Statistics for Satellite Links Between 10–50 GHz*", IEEE Antennas and Wireless Propagation Letters*, Vol. **7**, pp. 260 – 263, 2008.

Christodoulou, C. I., S. C., M. Gabella, and C.S. Pattichis, "Prediction of rainfall rate based on weather radar measurement," *IEEE Proceedings of Int. Joint Conference of Neural Networks*, Vol. 2, pp. 1393-1396, 2004.

Cioni, S. R. De Gaudenzi, and R. Rinaldo, "Adaptive coding and modulation for the reverse link of broadband satellite networks," in *IEEE Global Telecommunications Conference*, vol. 2, 1101– 1105, 2004.

Cooper, R. B. *Introduction to Queueing Theory*. Second Edition. Elsevier North Holland, New York. 1981.

Cox, D. C. and H. W. Arnold, "Results from the 19- and 28-GHz COMSTAR Satellite Propagation Experiments at Crawford Hill," *Proceedings of the IEEE*, Vol. 70, No. 5, pp. 458-488, May 1982.

Crane, R. K., "A two-component rain model for the prediction of attenuation statistics," Radio Science, Vol. 17, No. 6, pp. 1371-1387, 1982.

Dao, H., Md. R. Islam, K. Al-Khateeb, and A. Ishmail, "Analysis of rain fade duration over satellite-earth path at Ku-band in tropics," *International Conference on Computer and Communication Engineering*, 3-5 July 2012, Kuala Lampur, Malaysia 2012.

Diba, F. D., T. J. Afullo and A. A. Alonge, "Time series rainfall spike modelling from Markov Chains and queueing theory approach for rainfall attenuation over terrestrial and earth-space radio wave propagation in Jimma, Ethiopia*," 2016 Progress In Electromagnetic Research Symposium (PIERS)*, Shanghai, China, 8–11 August, 2016, pp. 4991 - 4995.

Dissanayake A., J. Allnutt and F Haidara, "A prediction Model that combines Rain Attenuation and other propagation impairments along earth-satellite paths," IEEE Transactions and Propagation, Vol. 45, No. 10, pp. 1546-1558, Oct. 1997.

Dissanayake, A, J. Allnutt and F. Haidara, "A prediction model that combines rain attenuation and other propagation impairments along earth-satellite paths," Online Journal of Space Communication, Issue No. 2, pp. 1-29, 2003.

Dutton, E. J., Dougherty, H. T. and Martin Jr., R. F., 1974: "Prediction of European rainfall and link performance coefficients at 8 to 30 GHz," Techn. Report No. ACC-ACO-16-74, Office of Telecommunications, U. S. Dept. of Commerce

E. Matricciani and Carlo Riva, "The Search for the Most Reliable Long-Term Rain Attenuation CDF of a Slant Path and the Impact on Prediction Models," *IEEE Transactions on Antennas and Propagation*, Vol. 53, No. 9, September 2005.

Emiliani, D. L., L. Luini, and C. Capsoni, "Analysis and parameterization of methodologies for the conversion of rain rate cumulative distributions from various integration times to one minute," *IEEE Antennas and Propagation Magazine*, Vol.51, No.3, pp. 70-84, Jan. 2009.

Flavin, R. K., "Rain attenuation considerations for satellite paths," Telecom Australia Research Laboratories Report No 7505, 1982.

Foty, D., B. Smith, S. Sinha, and M. Schröter, "The wireless bandwidth crisis and the need for power-efficient bandwidth". IEEE AFRICON Conf., Livingstone, Zambia, September 2011, pp. 1–6.

French, G. M. N., W. F. Krajewski, and R. R. Cuykendall, “Rainfall Forecasting in space and time using neural network,” *J. Hydrol*. Vol. 137, pp. 1-31, 1992.

Holm, H., *Adaptive Coded modulation: channel estimation*. Norwegian University of Science and Technology. (n.d.). Retrieved November 27, 2018: https://www.ceid.upatras.gr/webpages/faculty/alexiou/ahts/other_pdf/5_ACM.pdf.

Hung, N. Q., M. S. Babel, S. Weesakul, and N. K. Tripathi, “An artificial neural network model for rainfall forecasting in Bangkok, Thailand,” *Hydrol. Earth Syst. Sci*., 13, pp. 1413-1425, 2009.

Ippolito, L. J. Jr. *Satellite Communications Systems Engineering: Atmospheric Effects, Satellite Link Design and System Performance*, John Wiley and Sons Ltd, UK, 2008.

ITU-R Recommendation P. 530-17. *Propagation data and prediction methods required for the design of terrestrial line-of-sight systems*. *ITU*, Geneva, Switzerland, 2017.

ITU-R Recommendation P.1623. *Prediction method of fade dynamics on earth-space paths*. *ITU*, Geneva, Switzerland, 2005.

ITU-R Recommendation P.618-13. *Propagation and prediction methods required for design of earth-space telecommunication systems*. ITU-R, Geneva, Switzerland, 2017.

ITU-R Recommendation P.837-1. *Characteristics of precipitation for propagation modelling*. *ITU*, Geneva, Switzerland, 1994.

ITU-R Recommendation P.837-7. *Characteristics of Precipitation for Propagation Modelling*. *ITU*, Geneva, Switzerland, 2017.

ITU-R Recommendation P.838-3. *Specific attenuation model for use in prediction methods*. *ITU*, Geneva, Switzerland, 2005.

Jaffrain, J., and A. Berne, “Influence of the subgrid variability of the rain drop size distribution on radar rainfall estimates,” *Journal of Applied Meteorology and Climatology*, Vol. 51, pp. 780-785, April, 2018.

Jamie, M., *MTN and Huawei launch first outdoor 5G trial in South Africa*. May 8, 2018. Retrieved October 8, 2018: https://mybroadband.co.za/news/cellular/259253-mtn-and-huawei-launch-first-outdoor-5g-trial-in-south-africa.html.

Jian, Z., and W. X. Wu, “The application of feedforward neural network for X-ray image fusion,” International Nuclear Physics Conference, pp. 1-6, 2011.

Joss, J. K. Schram, J. C. Thoms, and A. Waldvogel, “On the quantitative determination of precipitation by radar,” Wissenschaftliche Mitteilung Nr. 63, Zurich, ETH, City-Druck AG, Zurich, Switzerland, 1970.

Kim, Y., Convolutional neural networks for sentence classification,” Proceedings of the 2014 Conference on Empirical Methods in natural language processing, pp. 1746-1751, Oct. 25-29, Doba, Qatar, 2014.

Kleinrock, L. *Queueing Systems.* Vol. I, Theory, John Wiley and Sons, New York, 1975

Kumar, K. *Satellite communication systems: Propagation-3*. Lecture notes. (n.d.). Retrieved November 27, 2018: http://textofvideo.nptel.ac.in/117105131/lec21.pdf

Lakshmi, S., Y. H. Lee, and J. T. Otung, “The role of particular rain drop size on rain attenuation at 11 GHz," *IEEE, ICICS*, 2007.

Lavergnat, J., and P. Gole "A Stochastic Raindrop Time Distribution Model," *AMS Journal of Applied Meteorology*, Vol. 37, No. 8, pp. 805-818, August 1998.

Le, J. *The 10 Neural network architectures machine learning researchers need to learn*. (n.d.). Retrieved November 25, 2018: https://medium.com/cracking-the-data-science-interview/a-gentle-introduction-to-neural-networks-for-machine-learning-d5f3f8987786.

LeCun, Y., L. Bottou, Y. Bengio, and P. Haffner, "Gradient-based learning applied to Document recognition," Proc. of the IEEE, Nov. 1998.

Lin, S. H., "Statistical behavior of rain attenuation," *The Bell System Technical Journal*, pp. 557-581, April 1973.

Luk, K. C., J. E. Ball, and A. Sharma, "An application of artificial neural networks for rainfall forecasting," *Mathematical and Computer modelling*, Vol. 33, pp. 683-693, 2001.

Maitra, A., "Rain attenuation modelling from measurements of rain drop size distribution in the Indian Region," *IEEE Antennas and Wireless Propagation Letters*, Vol. 3, pp. 180-181, 2004.

Marshall, J. S. and W. M. Palmer, "The distribution of raindrops with size," *J. Meteor.*, Vol. 5, 165-166, 1948.

Matricciani, E, and C. Riva, "The search the most reliable long-term rain attenuation CDF of a slant path and the impact on prediction models," *IEEE Transactions on Antennas and Propagation*, Vol. 53, No. 9, pp. 3075-3079, Sept. 2005.

Matricciani, E., "Physical-mathematical model of the dynamics of rain attenuation based on rain rate time series and a two-layer vertical structure of precipitation," *Radio Science*, Vol. 31, No. 2., pp. 281-295, Mar. 1996.

Matricciani, E., "Prediction of fade durations due to rain in Satellite Communication System," *Radio Science*, Vol. 32, No. 3, pp. 935-941, May-June, 1997.

Matricciani, E., "Rate of change of signal attenuation from Sirio at 11.6 GHz," *Electronic Letters*, Vol. 17, No. 3, pp. 139-141, Feb. 1981.

B. McKellar, N., M. New, and C. Jack, "Observed and modelled trends in south Africa: 1960-2010," *S Afr J Sci*., Art. No. 2013-0353, 2014.

Michaelides, S. C., C. C. Neocleous, and C. N. Schizas, "Artificial neural networks and multiple linear regressions in estimating missing rainfall data," in *Proceedings of the DSP95 International Conference on Digital Signal Processing, Limassol, Cyprus*, 1995, pp. 668–673.

Miller, R., *Adaptive coding and modulation (ACM) in the CDM-625 advanced satellite modem* [White paper], June 2009. Retrieved November 27, 2018, from COMTECH EF Data: http://www.comtechefdata.com/files/articles_papers/wp-cdm625_acm_white_paper.pdf

Mitchel, W. C., L. Nguyen, A. Dissanayake, B. Markey, and A. Le, "Rain fade compensation for Ka-band communication satellites," COMSAT Laboratories, Clarksburg, Maryland, NASA/CR-97-206597 Report, December 1997.

Moupfouma, F, and S. Martins, "Modeling of the rainfall rate cumulative distribution for design of satellite and terrestrial communication systems," *International Journal of Satellite Communication*, 13(2) 105-115, 1995.

Moupfouma, F., "Model of rainfall-rate distribution for radio system design," IEE *Proceedings*, Vol. 132, No. 1, pp. 39-43, Feb. 1985.

Moupfouma, F., 1987: "More about rainfall rates and their prediction for radio systems," *IEEE Proceedings*, Vol. 134 (6), Pt. H, 527-537.

Nakazawa S., M. Nagasaka, S. Tanaka and K. Shogen, "A method to control phased array for rain fade mitigation of 21-GHz band broadcasting satellite," *Proceedings of the Fourth European Conference on Antannas and Propagation* (EuCAP), pp. 1-5, 2010.

Nayak, D. R., A. Mahapatra, and P. Mishra, "A Survey on rainfall prediction using artificial neural network," *International Journal of Computer Applications*, Vol. 72, No. 16, pp. 32-40, Jun. 2013.

Odedina, M. O. and T. J. Afullo, "Determination of rain attenuation from electromagnetic scattering by spherical raindrops: Theory and experiment," *Radio Science*, Vol. 45, pp. 1-15, RS1003, doi:10.1029/2009RS004192, 2010.

Paraboni, A. and C. Riva, "A new method of the prediction of fade duration statistics in satellite links above 10 GHz," *Int. J. Sat. Com.*, Vol. 12, pp. 387-394, 1994.

Paraboni, A., and C. Riva, "A new method of the prediction of fade duration statistics in satellite links above 10 GHz," *Int. J. Sat. Com.*, Vol. 12, pp. 387-394, 1994.

Pawlina, A., "No rain intervals within rain events: some statistics based on Milano radar and rain-gauge data," *COST Action 280, 1st International Workshop*, July, 2002.

Purnomo, H. D., K. D. Hartomo, and S. Y. J. Prasetyo, "Artifcial neural network for monthly rainfall rate prediction," *1st Annual Applied Science and Engineering Conference*, 180, pp.109, 2017.

Rambaugh, J. I., Jacobson and G. Booch. *The Unified Modelling Language Reference manual.* 2nd Ed. Pearson, Boston, 2005.

Rice, P. L. and N. R. Holmberg, "Cumulative Time Statistics of Surface-Point Rainfall Rates," *IEEE Transactions on Communications*, Vol. COM-21, No. 10, pp. 1131-1136, 1973.

Rojas, R., "The Backpropagation Algorithm" in *Neural Networks: A systematic Introduction,* Berlin, Germany: Springer-Verlag, 1996, pp. 151-182.

Rumelhart, D. E., G. E. Hinton, and R. J. Williams, "Learning internal representations by error propagation," in *Parallel Distributed Processing*, Vol. 1, J. A. Feldman, P. J. Hayes, D. E. Rumelahart, Eds. London, England: MIT Prss, 1986, pp. 318-362.

S. H. Lin, "Statistical behavior of rain attenuation," *The Bell System Technical Journal*, pp. 557-581, April 1973.

Saad, N. W. M., A. F. Ismail, K. Badron, and N. H. M. Sobli, "Assessments of time diversity rain fade mitigation technique for V-band space-earth link operating in tropical climate," *International Journal of Electrical energy*, Vol. 1, No. 4, pp. 268-273, 2013.

Schonhuber, M., K. Plimon, and M. Thurai, "Statistical significance of specific rain attenuation in Southern Africa," *Progress In Electromagnetic Research B*, Vol. 46, 275-297, 2013.

Segal, B., "The Influence of the Raingauge Integration Time on measured Rainfall-Intensity Distribution Functions," *Journal of Atmospheric and Oceanic Technology*, Vol. 3, 662-671, 1986.

Tarchi, D., G. E. Corazza, and A. Vanelli-Coralli, "Adaptive coding and modulation techniques for mobile satellite communications: a state estimation approach," *6th Advanced Satellite multimedia systems (ASMS) and 12th Signal Processing for Space Communications Workshop (SPSC)*, pp. 36, 2012.

Ulbrich, C.W., "Natural variation in the analytical form of the raindrop size distribution," *J. of Climate and Applied Meteor.*, vol. 23, pp. 1764–1775, 1983.

Vikas Gupta. *Understanding feedforward neural networks*. October 9, 2017. Retrieved November 27, 2018: https://www.learnopencv.com/understanding-feedforward-neural-networks/

Yunus, M. M., J. Din, H. Y. Lam, and S. L. Jong, "Estimation of interfade duration for Ku- and Ka-band satellite communication system in equatorial Malaysia," *Asia-Pacific Radio Science Conference*, Seol Korea, August, 21st -25th, pp. 1967-1970, 2016.

APPENDICES

Appendix 1

Summary of rain rate conversion models [*Emilliani et al., 2009*]

Model Name and Nature	Formulation	Advantages	Disadvantages
Direct power law. Empirical	$R_1(P) = aR_T(P)^b$	Simplicity of use Availability of coefficients from various research works Currently recommended by the ITU	Increasing rms with increasing t Not of direct global applicability High sensitivity to changes in the parameters
Probability conversion factor. Empirical	$CF(P) = \frac{R_1(P)}{R_T(P)}$ $\begin{cases} CF(P) = aP^b \\ CF(P) = aP^b + ce^{dP} \end{cases}$	Easy to use Best performing in tropical zones Moderate sensitivity to changes in the parameters	Limited availability of coefficients, compared to the direct power law Applicability limited to 0.001% and 1% (as per the literature)
Lavergnat-Golé conversion factor. Physical-stochastic	$CF = \frac{t_2}{t_1}$ $P_2(R_2) = CF^a P_1(R_1)$ $R_2 = \frac{R_1}{CF^a}$	Simplicity of use, only one parameter needed for conversion between integration times Approach from random processes (physical basis) Robust to changes in the parameter (small variations on conversion rms) Physical-stochastic approach	Requires empirical determination of the parameter. Not tested globally by the scientific community.
Moupfouma analytical conversion	$P(R)_1 = \left(\frac{a_1}{a_T}\right) R^{(b_T - b_1)} e^{(u_T - u_1)R} P(R)_T$	Useful in tropical regions where the Moupfouma distribution has been proven to work. A Global model already in place for the one-min distribution.	Requires knowledge of local parameters for a Moupfouma distribution Not tested globally by the scientific community.

Appendix 2

Rec. ITU-R P.837-7

FIGURE 1

Rainfall rate exceeded for 0.01% of an average year

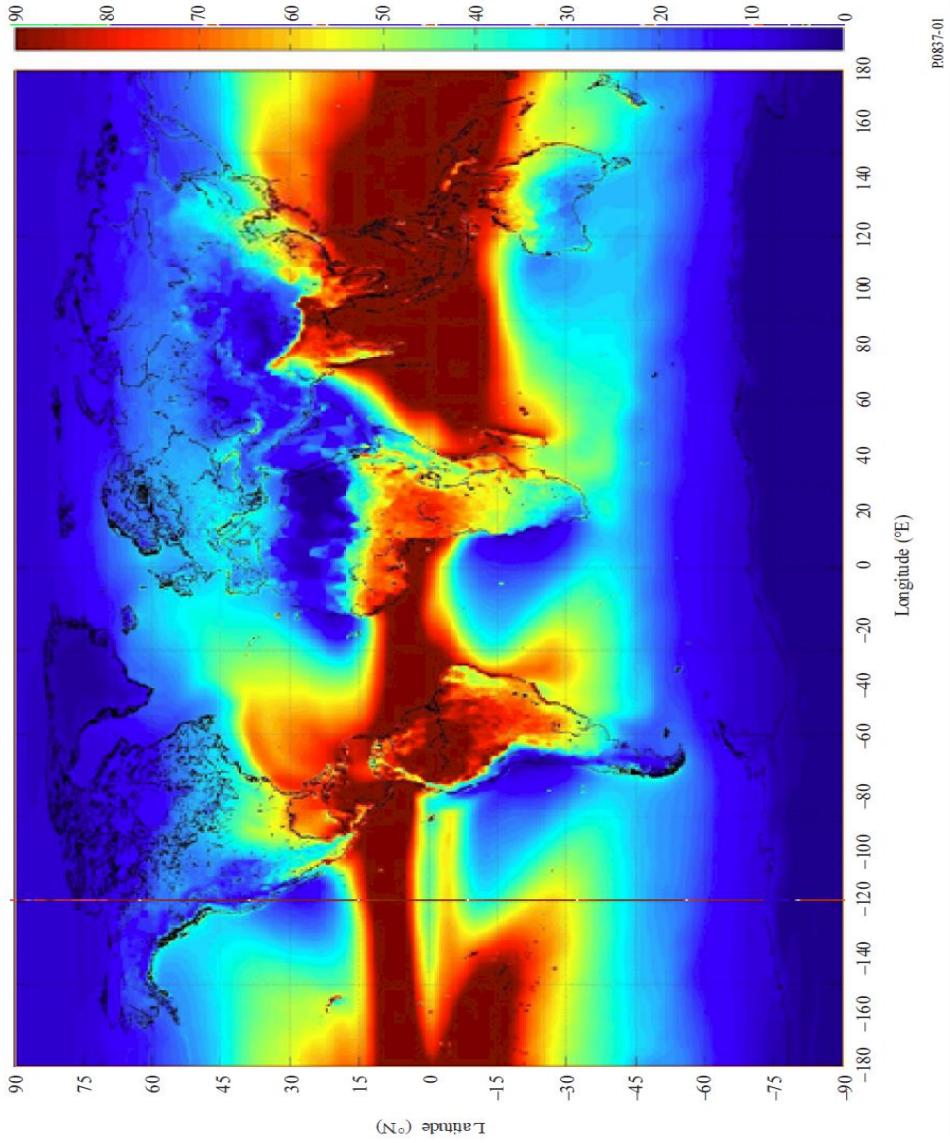

Appendix 3

Best fit parameters of (2.21) for Fucino as a function of probability

Probability (%)	C_1	C_2	δ_1	δ_2
0·01	−220·65	151·51	−0·0420	−0·0649
0·05	−261·61	218·05	−0·0389	−0·0478
0·1	−227·74	191·17	−0·0368	−0·0448
0·3	−198·17	171·73	−0·0334	−0·0390
0·5	−180·00	157·02	−0·0314	−0·0362
0·8	−161·15	143·04	−0·0289	−0·0327
1	−142·11	125·73	−0·0272	−0·0308

Appendix 4

Best fit parameters of (2.21) for Gera Lario as a function of probability

Probability (%)	C_1	C_2	δ_1	δ_2
0·01	−369·18	255·99	−0·0503	−0·0778
0·05	−274·99	206·80	−0·0423	−0·0587
0·1	−253·41	202·80	−0·0394	−0·0508
0·3	−198·99	164·53	−0·0348	−0·0430
0·5	−190·00	160·49	−0·0333	−0·0401
0·8	−172·33	147·27	−0·0316	−0·0375
1	−147·89	124·98	−0·0303	−0·0363